61510

P-133

INVESTIGATION OF THE INFLUENCE OF A STEP CHANGE IN SURFACE ROUGHNESS ON TURBULENT HEAT TRANSFER

Robert P. Taylor
Hugh W. Coleman
J. Keith Taylor
M. H. Hosni

Thermal & Fluid Dynamics Laboratory
Mechanical and Nuclear Engineering Department
Mississippi State University
Mississippi State, MS 39762

June 1991

Final Report for the Period January 1, 1990 - June 30, 1991

Grant Number NAG 3 1116

National Aeronautics and Space Administration
Lewis Research Center
Cleveland, OH 44135

INVESTIGATION OF THE INFLUENCE OF A STEP CHANGE IN SURFACE ROUGHNESS ON TURBULENT HEAT TRANSFER

by

Robert P. Taylor, Hugh W. Coleman, J. Keith Taylor, and M. H. Hosni

Thermal & Fluid Dynamics Laboratory
Mechanical and Nuclear Engineering Department
Mississippi State University
Mississippi State, MS 39762

ABSTRACT

The work reported here was motivated by concern over the use of smooth heat flux gages on the otherwise very rough SSME fuel pump turbine blades. To gain insights into behavior of such installations, fluid mechanics and heat transfer data were collected and are reported for a turbulent boundary layer over a surface with a step change from a rough surface to a smooth surface. The first 0.9 m length of the flat plate test surface was roughened with 1.27 mm hemispheres in a staggered, uniform array spaced 2 base diameters apart. The remaining 1.5 m length was smooth. The effect of the alignment of the smooth surface with respect to the rough surface was also investigated by conducting experiments with the smooth surface aligned with the bases or alternatively with the crests of the roughness elements. Stanton number distributions, skin friction distributions, and boundary layer profiles of temperature and velocity are reported and are compared to previous data for both all-rough and all-smooth wall cases. The experiments show that the step change from a rough surface to a smooth surface has a dramatic effect on the convective heat transfer. In most cases, the Stanton number and skin friction coefficient drop below the smooth-wall correlation immediately downstream of the change in roughness. The alignment of the surfaces has only a weak effect of the Stanton number and skin friction coefficient just downstream of the interface.

It is concluded that use of smooth heat flux gages on otherwise rough surfaces could cause large errors. It is recommended that heat transfer data collected in this manner be used with caution.

PREFACE

This work was conducted in the Thermal & Fluid Dynamics Laboratory of the Mechanical and Nuclear Engineering Department at Mississippi State University. This research was supported by the NASA Lewis Research Center, Grant #NAG 3 1116. Mr. Kestutis Civinskas of the Lewis Research Center was the program manager. The interest and encouragement of Mr. Civinskas and of Mr. Bob Boyle of the Lewis Research Center are gratefully acknowledged. The experimental apparatus was funded in part by the U.S. Air Force Office of Scientific Research Grant AFOSR-85-0075. The expert assistance of Mr. Mike Bolander and Mr. Walid Chakroun in the collection of the data is also gratefully acknowledged.

TABLE OF CONTENTS

Page

CHAPTER

APPENDIX

NOMENCLATURE

A	plate surface area
B	bias limit
C_D	Roughness element drag coefficient
C_f	skin friction coefficient ($2\tau_w/\rho U_\infty^2$)
C_p	specific heat
d_o	roughness element base diameter
d(y)	Local roughness element diameter
H	Enthalpy
h	convective heat transfer coefficient
K	Thermal conductivity
k	roughness element height
L	roughness element spacing
l_m	Mixing length
Nu_d	Roughness element Nusselt number
P	Pressure
Pr	Prandtl number
Pr_t	Turbulent Prandtl number
q_c	conductive heat loss rate
q_r	radiative heat loss rate
R	recovery factor

Re_d	Reynolds number based on local roughness element diameter
Re_x	x-Reynolds number
St	Stanton number ($h/\rho C_p U_\infty$)
T	local fluid static temperature
T_∞	freestream static temperature
T^+	nondimensional temperature $[(T_w - T)u^*/U_\infty(T_w - T_0)St]$
T_o	freestream stagnation temperature
T_R	Roughness element temperature
T_r	freestream recovery temperature
T_w	wall (plate) temperature
T_{wb}	freestream wet-bulb temperature
u	mean longitudinal velocity
u^*	friction velocity ($U_\infty(C_f/2)^{1/2}$)
u'	longitudinal velocity fluctuation
u^+	nondimensional u (u/u^*)
$\overline{u'^2}$	Turbulence intensity factor
$\overline{u'v'}$	Reynolds shear stress factor
U	95% coverage uncertainty
U_∞	freestream velocity
$(UA)_{pp}$	plate-to-plate overall conductance for q_c calculation
$(UA)_{pr}$	plate-to-rail overall conductance for q_c calculation
v	Mean normal velocity
$\overline{v'h'}$	Turbulent heat flux factor

W	test plate heater power
x	axial distance from nozzle exit
x_0	Lag model parameter
x_c	Turbulence transition model parameter
y	coordinate normal to the wall surface
y^+	nondimensional y (yu^*/ν)

Greek

β_x	Blockage factor
β_y	Blockage factor
δ	boundary layer thickness
δ_0	Lag model parameter
δ_1	displacement thickness
δ_2	momentum thickness
δ_i	internal layer thickness
Δ	thermal boundary layer thickness
Δ_2	enthalpy thickness
ε	plate surface emissivity
η	Lag model parameter
λ	Lag model parameter
μ	Dynamic viscosity
μ_t	Turbulent eddy viscosity
μ_{t0}	Lag model parameter
μ_{te}	Lag model parameter

ν	kinematic viscosity
ρ	density
σ	Stefan-Boltzmann constant
τ	viscous shear stress

<u>Subscripts</u>

baro	barometric
w	wall
∞	freestream

LIST OF FIGURES

LIST OF TABLES

Chapter I

INTRODUCTION

In the design and analysis of many engineering systems, knowledge of the skin friction and heat transfer characteristics for turbulent flow are essential. These characteristics are usually affected by the shape and condition of solid surfaces. Surface roughness plays an important role in many engineering applications such as turbine blades, high performance aircraft, heat exchangers, and piping systems. In most instances, these surfaces are rough in the aerodynamic sense.

The objectives of this report are to describe a set of experiments which investigates the effects of a step change from a rough to a smooth surface on heat transfer in the turbulent boundary layer and to present some results from these experiments. The motivation for this work was concern over the results obtained when using smooth heat flux gauges on otherwise rough turbine blades. These gauges are usually quite smooth. The quality of the data received from this method can frequently depend upon the roughness of the surface being tested. If the surface is also smooth, the heat flux measured by the gauge will likely be close to the heat flux of the surface itself. However, if the surface is rough then the heat flux measured with the smooth gauges could be quite different from the actual heat flux on the rough surface. The primary application for this research effort involves the similar problem of using smooth heat flux gauges for external heat transfer measurements on otherwise rough turbine blades from the Space Shuttle Main Engine (SSME) fuel-pump turbine.

Taylor (1990) measured and classified the surface roughness on turbine blades from TF-39 and F-100 aeroengines. Taylor (1989) also made roughness measurements on the SSME fuel-pump turbine blades. The blades were determined to be very rough. The TF-39 and F-100 turbine blades had an average roughness ranging from about 1.5 μm to about 10 μm. This was determined to be very rough since the boundary layer thickness is on the order of 1 mm. The SSME fuel-pump turbine blades had average roughness heights on the order of 15 μm with the boundary layer thickness on the order of 0.5 mm. The heat flux gauges used to measure the heat transfer are much smoother than surrounding turbine blade surface. How the heat transfer is affected by the step change in surface roughness was the primary motivation for this research work.

Flows with step changes in surface roughness are also important in planetary boundary layer flows over a land-sea interface and mountain ranges. There is a large group of theoretical and experimental work which pertains to step changes in surface roughness for these atmospheric flows.

Background

Jacobs (1939) performed some of the early experimental work on this subject for fully developed channel flows. Antonia and Luxton (1971a, 1972) presented one of the most detailed data sets for zero pressure gradient boundary layer flows. They performed extensive velocity, turbulence, and skin friction measurements for both smooth-to-rough and rough-to-smooth schemes. Their measurements were made using rib-roughened surfaces with the rib crests on the rough surface aligned with the smooth surface. Antonia and Luxton (1971b) also studied the effects of a smooth-to-rough transition with the bases of the ribs aligned with the smooth section. This gave a transition to a rough surface with the roughness elements upstanding. Schofield (1975) performed and presented a series of flow measurements for a step change in surface roughness with adverse pressure gradients. He also used a ribbed rough surface with the crests of the ribs aligned with the smooth surface. Andreopoulous and Wood (1982) performed and presented measurements of velocity profiles, turbulence quantities, and skin friction distribution for a flow over a smooth plate which was roughened in one narrow strip at mid plate using sandpaper. They referred to their alignment as "slightly upstanding".

There have also been theoretical contributions made by Townsend (1965) who developed a theory for velocity and temperature profiles development in the internal layer which develops after a change in surface condition. Antonia and Wood (1975) and Andreopoulous and Wood (1982) each presented prediction methods based on numerical solutions of the boundary layer equations.

As indicated from the previous listed sources, there is a fair amount of experimental and theoretical work that has been reported for developments in the turbulent boundary layer after a step change in surface roughness. However, there exists no heat transfer data for turbulent boundary layer flow with a step change in surface roughness. This is not surprising since there is very little good convective heat transfer data for rough surfaces in general.

Current Research Effort

The objective of the current research effort was to obtain comprehensive convective heat transfer and fluid mechanics data for a step change in surface roughness. As stated, this work was performed to gain insight into the use of smooth heat flux gauges on the otherwise rough SSME fuel-pump turbine blades.

In the full scale turbine blade tests, there are two distinct reasonable limits to the location of the smooth surface. The first has the smooth surface aligned with the base of the roughness elements, or base-aligned, as shown in Figure 1a. The second is the case of the smooth surface aligned with the crests of the roughness elements, or crest-aligned, as shown in Figure 1b. For this work, both alignments were investigated for carefully matched flow conditions. The effects of the alignment of the smooth surface with respect to the rough surface at the rough-to-smooth interface were investigated to determine if the alignment has a strong effect on the heat transfer and fluid dynamics, and if one alignment would be preferred over the other.

The work consisted of heat transfer and temperature profile measurements as well as measurements of velocity profiles, axial turbulence intensity, and skin friction coefficient distributions. All measurements were made for both alignments under carefully matched flow conditions. Also, the rough-to-smooth data were compared to all-rough and all-smooth wall tests made in the same facility.

Overview

This report presents the significant heat transfer and fluid dynamics results for a step change in surface roughness. Direct comparisons are made between the two alignments. The experimental facility and the operation procedures are discussed in

Chapter II. A summary of the THTTF operating systems and information concerning the Stanton number and skin friction distributions are included. Chapter III presents the experimental heat transfer results for the rough-to-smooth surface and compares the heat transfer results between the two alignment cases. Likewise, Chapter IV presents the experimental fluid mechanics data for the rough-to-smooth surface and compares the similarities and difference between the two alignments. Chapter V presents the discrete element model and compares the results of the computations with the data. A summary and conclusions are presented in Chapter VI. Appendix A details the method used to experimentally determine the Stanton number and its corresponding uncertainty analysis. Tabular data for the Stanton number and skin friction distributions are presented in Appendix B.

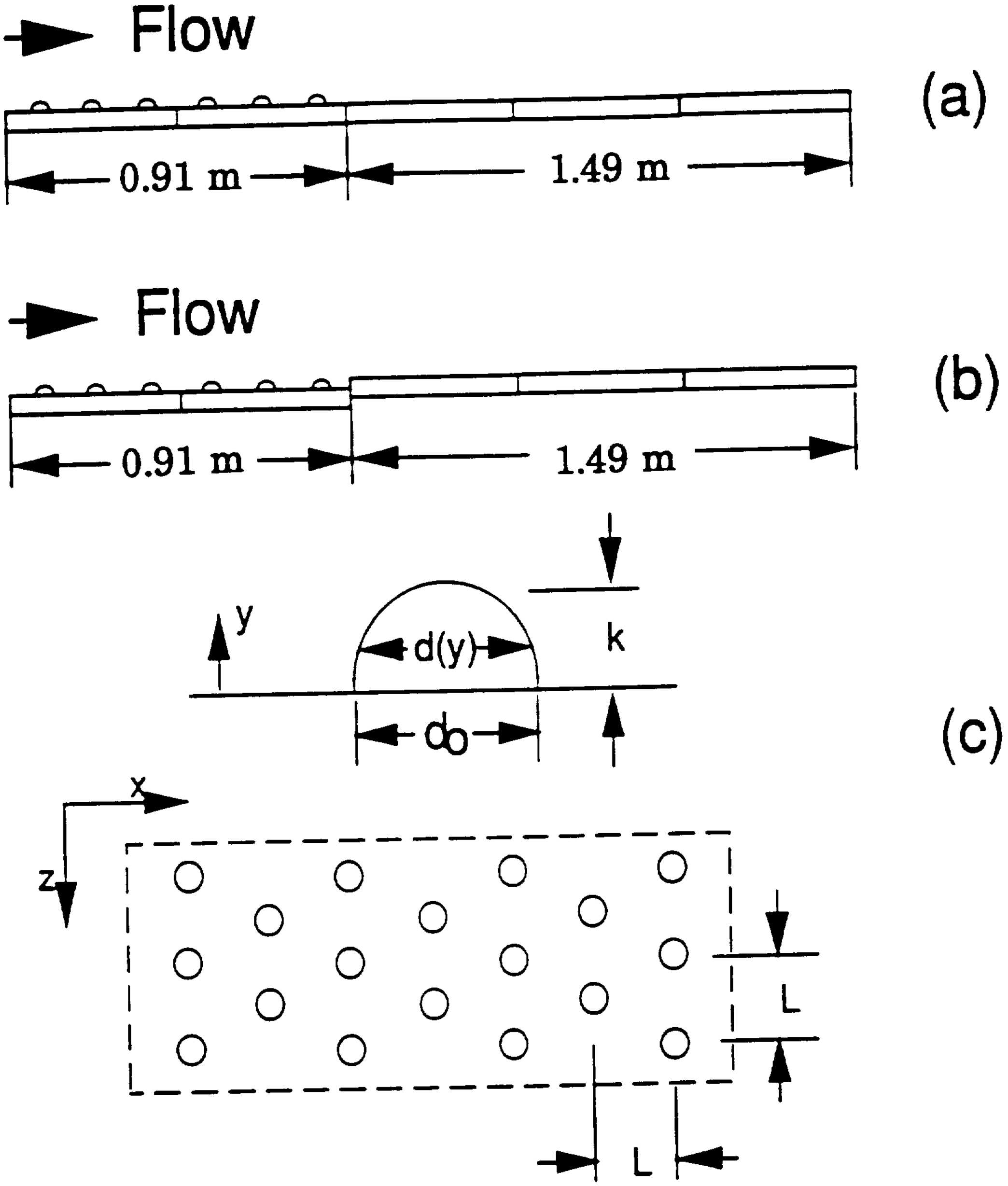

$d_o = 1.27$ mm

$k = 0.635$ mm

$L = 2.54$ mm

Figure 1. Descriptions of the rough-to-smooth test surface alignment schemes and the roughness shape for the hemisphere roughened surface.

CHAPTER II

EXPERIMENTAL FACILITY AND MEASUREMENT TECHNIQUES

The Turbulent Heat Transfer Test Facility (THTTF) was designed and built to study the characteristics of heat transfer and fluid dynamics in turbulent flat plate boundary layer flow. The THTTF was originally designed by Norton (1983). It is geometrically similar to a test apparatus used at Stanford University to investigate turbulent boundary layer flow and heat transfer in flow over a single, porous rough surface [Healzer (1974), Pimenta (1975), Coleman (1976), Ligrani (1979)].

General Description

Schematically shown in Figure 2, the THTTF is a closed loop subsonic wind tunnel which can deliver a uniform air flow over a set of individually heated flat test plates which abut together to form a continuous 2.4 m long test surface. Each plate is fitted with its own heater pad and can be maintained for either a uniform temperature or uniform heat flux case. The local Stanton number is obtained by applying an energy balance to each plate. Boundary layer velocity and turbulence profiles are determined with hot-wire anemometry techniques. Skin friction coefficients are determined by using hot-wire anemometry or the Preston tube method. Thermal boundary layer temperature profiles are measured using a thermocouple probe.

Descriptions of the apparatus, measurement procedures, and system debugging and qualification are discussed in great detail by Coleman et al. (1988) and Hosni et al. (1989). The determination of the Stanton number from the measured variables and the uncertainty associated with the experimentally determined Stanton number particular to this work are presented in Appendix A.

The THTTF is composed of four primary systems: (1) the air flow system, (2) the test plate system, (3) the cooling water system, and (4) the automated data acquisition and control system. A discussion of each system follows.

The Air Flow System

The air flow system is a closed loop design that delivers a uniform velocity, low freestream turbulence intensity, controlled temperature air flow at the 10 by 51 cm inlet to the 2.4 m long test section. The air velocities can range from 6 m/s to 67 m/s which correspond to x-Reynolds numbers from about one million up to ten million at the end of the test section. The blower is a Buffalo Forge 45AW industrial blower and is driven by a belt and pulley with an Eaton eddy current clutch using a Dynamatic 18.6 kilowatt electric motor. The air exits the blower and travels through the 1.2 by 0.6 m overhead duct before entering the header. After turning through the header, the air is filtered through a linen particulate filter before passing through a Trane air to water 4 row cooling coil. After exiting the cooling coil, the flow is directed through a 3.8 cm thick aluminum honeycomb flow straightener and then through a series of 4 woven screens. The air then enters a three dimensional nozzle which is designed to smoothly accelerate the flow without separation [Healzer (1974)]. The flow is delivered to the test section at the 10 by 51 cm nozzle outlet with a uniform velocity field and is passed over a 1 mm by 12 mm boundary layer trip immediately upstream of the test plates.

The rectangular cross sectioned test section is fabricated of 1.3 cm thick clear plexiglass top and side walls. The bottom wall is the test surface which is comprised of the 24 test plates abutted together to form a continuous flat surface. One of the sidewalls is equipped with 24 static pressure taps spaced 10.2 cm apart and positioned 2.5 cm above the center of each test plate. Circular access holes for test probe entry are centered over each plate along the center-line of the top wall. These access holes are plugged with precision machined stoppers when not in use. The top wall elevation is adjustable to maintain the prescribed zero pressure gradient and constant freestream velocity in the axial direction. An inclined manometer with a resolution of 0.06 mm of water is connected to the sidewall static pressure taps to measure the pressure gradient in the flow direction. For the rough to smooth tests the static pressure variations along the test section were less than 4.2 mm for a freestream velocity of 66 m/s and 0.19 mm for velocity of 12 m/s, with corresponding maximum pressure coefficients of 2.0×10^{-5} and 2.6×10^{-5} respectively.

After exiting the test section, the air passes through an adjustable plexiglass diffuser and a series of screen inserts and enters a wooden vaned diffuser before entering the blower plenum. Filtered make-up air is added in the blower plenum to replace air lost through leakage in the air conduits.

The blower and motor are affixed to a massive concrete pad with vibration damping feet to minimize vibrations. The test section is isolated from key vibration sources through the use of flexible couplings at key locations. The noise in the overhead duct, plenum, and header is damped through the use of batt insulation covered by rigid fiberglass insulation board in these components. Also, the blower and motor are housed inside vented, insulation lined boxes for noise abatement.

The Plate System

The bottom surface of the THTTF test section is composed of individually machined plates that fit together to form a continuous flat surface. As shown in Figure 1, the first 0.91 m of the test section was composed of 9, 10.2 cm wide plates roughened with 1.27 mm diameter hemispheres, and the remaining 1.49 m length was made up of smooth plates. The roughness elements were spaced 2 base diameters apart in a staggered array as shown in the figure. Each rough plate was machined from a solid aluminum blank, so the contact between the roughness element and the smooth portion is perfect. The portion of the test surface immediately downstream of the rough-to-smooth interface was composed of 4 smooth plates with 2.54 cm width. These were installed to give better resolution of the Stanton number behavior after the step. The remaining smooth-wall plates were 10.2 cm wide. Dowel pins, as shown in Figure 3, are used to secure the plates together. The allowable mismatch at the joint between two plates is 0.013 mm. The plates rest on support rails that are heated to the plate temperature to minimize conduction losses. The test section support structure is fully encased in a removable wooden shroud which is amply insulated to prevent heat transfer with the laboratory environment. Figure 4 shows a cross section of the THTTF test section.

The hemispherically roughened plates with $L/d_0 = 2$ were chosen because on the 2.4 m test section plate, the roughness scales reasonably well with the roughness on the SSME fuel pump turbine blades. Taylor (1989) made comparisons of the

THTTF test section to the SSME blades. Assuming the heat flux gauges to be 1.25 mm in diameter, the following table compares the conditions in THTTF test section to estimated conditions in ground tests on the actual SSME blades at Calspan in Buffalo, NY.

	L/δ	k/δ	St/St_s	Re_x
SSME	4	0.003-0.03	≈ 2	$\approx 10^6$
THTTF	1-2	0.025	≈ 2	$\approx 10^6$

L is the length of the smooth heat flux gauge on the SSME turbine blade (1.25 mm) or the length of the four combined 2.54 cm wide THTTF plates (10.2 cm), k is the roughness height, δ is the boundary layer thickness, and St_s is the smooth surface Stanton number. The SSME Reynolds number is based on estimated test conditions at the mid chord. There is good agreement between the scaling of the THTTF test section and the actual SSME blades.

Each plate in the THTTF contains two thermistors for temperature measurement and is fitted with a flexible, rubber-encased, electric heating pad. The plate temperature is measured to within ±0.1 C using the two thermistors which are mounted in wells drilled into the lower surface of the plate. The power to each plate is regulated by a motorized transformer, which is controlled by the Automated Data Acquisition and Control System. Experience in performing heat transfer tests in the THTTF has shown that plate temperatures can be held to within ±0.1 C of a desired constant wall temperature for the entire 2.4 m length of the test surface. Design computations have shown that under these heating conditions the plate and the associated roughness elements can be considered to be at a uniform temperature.

The Cooling Water System

The cooling water system is needed by the THTTF to remove excess heat from the air and maintain the air at some constant temperature. This system is composed of a 570 liter water storage tank, a Trane 4 row air-to-water cooling coil, a motorized ball valve, a centrifugal pump, and PVC piping to circulate the cooling water. The cooling water is pumped from the storage tank to the cooling coil. Heat is transferred to the cooling water from the warm test air. A proportional amount of the warmer water may be dumped into a floor drain through the motorized ball valve. The ball valve is manually adjusted so that the water temperature in the loop and, thus, the air temperature in the test section is held at some constant value. The water level in the storage tank is held at a desired level with make-up cooling water from the building supply by depth sensing valves located in the storage tank.

The Data Acquisition and Control System

The THTTF is monitored and controlled by a Hewlett-Packard Series 9000 Model-220 personal computer and a Hewlett-Packard 3045A Automatic Data Acquisition and Control System (ADACS). This includes an HP-3437A high speed system voltmeter, an HP-3456A high resolution digital voltmeter, and HP-3497A data acquisition/control unit and a number of special function plug-in assemblies. Suryanarayana (1986) gives a detailed discussion of the ADACS and its use in the THTTF.

Information is relayed to the personal computer via transducers that are wired into ADACS and are used to monitor the THTTF. Using the operating condition information, the personal computer decides on the proper response based on programming, and sends the properly controlled commands to the ADACS. The ADACS can control the rail heaters, the plate heaters, the cooling water dump valve, and the blower motor. When the proper equilibrium conditions are met, the personal computer instructs the ADACS to collect the necessary data.

Measurement Techniques

The techniques used to determine the Stanton number, the mean velocity and turbulence quantities, the skin friction coefficient distributions, and the thermal boundary layer temperature profiles are discussed below.

Stanton Number Determination

By applying an energy balance to each test plate in the test section, the data reduction equation for the experimentally determined Stanton number is found to be

$$St = \frac{W - q_r - q_c}{\rho\, U_\infty A\, C_p\, (T_w - T_o)} \tag{1}$$

The plate heater power, W, is measured using a precision wattmeter. Using a gray-body enclosure model, the radiation heat loss, q_r, is determined with the emissivity of the nickel plated plates estimated to be 0.11. The conductive heat loss rate, q_c, is calculated using an experimentally determined value of overall conductance from plate to rail, $(UA)_{pr}$, and an experimentally determined value of overall conductance from plate to plate, $(UA)_{pp}$. The conduction losses are minimized by insulating underneath the test plates and actively heating the support rails. The density and specific heat of the air are determined from moist air property data using measurements of barometric pressure and wet and dry bulb temperatures in the THTTF test section.

The freestream velocity is determined with a Pitot tube and specially calibrated pressure transducers. Specially calibrated thermistors are used to measure the air and plate temperatures. The freestream total temperature is calculated using a recovery factor of R = 0.86 (Eckert and Goldstein, 1976) for the freestream thermistor probe. The derivation of the Stanton number data reduction equation from an energy balance on a test plate and the details of determination of each of the variables used are presented in Appendix A.

The uncertainty analysis of the Stanton number is based on the ANSI/ASME Standard on Measurement Uncertainty (1986), following the procedures of Coleman and Steele (1989). The bias limits for the sixteen variables involved in the determination of the Stanton number were estimated by Hosni (1989) and are presented in Appendix A. Some of the elemental contributions to the bias limits were correlated since the thermistors were calibrated against the same standard. These correlated biases, which reduce the overall uncertainty in the experimentally determined Stanton number, were accounted for in the uncertainty analysis.

During the design and construction phase of the THTTF, a detailed uncertainty analysis of the determination of Stanton number was made. This analysis showed that relative to bias limits corresponding to the measured variables, the precision limits were negligible. Therefore, replications of the Stanton number at a given set point should show negligible scatter. In previous work in the THTTF, it has been shown that for low freestream velocities ($U_\infty \leq 12$ m/s for the smooth plates and $U_\infty \leq 6$ m/s for the rough plates) the time constant of the THTTF is large enough such that variations in line voltage and cooling water temperature reduce the ability to maintain a strict steady state. As discussed by Hosni et al. (1989), a 95 percent confidence estimate of the precision limit in the 6 m/s rough plate and 12 m/s smooth plate Stanton numbers was estimated as 3 percent. The 3 percent precision limit contribution was combined with the bias limit by a root-sum-square to obtain the overall uncertainty in Stanton numbers.

Mean Velocity and Turbulence Intensity

Local mean velocities are measured with the horizontal hot-wire. The horizontal hot-wire probe is mounted on a micrometer arrangement which allows proper positioning along the x, y, and z axes. Using a fourth order least squares calibration equation, velocities are calculated from 1000 instantaneous anemometer output voltages measured 0.01 seconds apart. For each velocity profile, the probe was positioned in the freestream and the reference velocity, U_∞, was measured. The probe was then lowered to a height above the smooth wall as determined by a fixed keel. The keel height was set to prevent contact between the hot-wire probe and the plate surface. Measurements were taken at intervals such that the normalized velocity (u/U_∞) increased 1-2 percent from point to point in the near-wall region and 2-4 percent in the outer region. The overall uncertainty in the values of u were estimated by Coleman et al. (1988) to be ± 2 percent.

The measurements of the fluctuating longitudinal velocity component $\overline{u'^2}$ were made with the horizontal hot-wire in conjunction with the mean velocity measurements described above. The longitudinal velocity fluctuation $\overline{u'^2}$ was taken as the variance of the 1000 computed velocities. The overall uncertainty associated with the measurements of $\overline{u'^2}$ is ± 5 percent.

Skin Friction Coefficient Determination

The skin friction coefficients over the smooth-wall surface were determined using the method of Preston (1954). Preston's method uses a simple Preston tube resting on the wall surface and depends upon the assumption of a universal inner law (law of the wall) common to smooth wall turbulent boundary layer flows. The difference between the total pressure at the Preston tube of 1.6 mm inside diameter and the undisturbed static pressure measured at a pressure tap in the sidewall at the same x-location as the Preston tube was measured with the same calibrated pressure transducers used to determine the freestream velocity. This difference in pressure was used with Patel's (1965) calibration equation to solve for the skin friction coefficient.

The Preston tube method of determining the skin friction coefficient is valid only for smooth-wall turbulent boundary layer flows because calibrations have only been made for smooth walls. Unfortunately, the region just downstream of the step change in surface roughness does not have a well developed smooth-wall inner layer. Therefore, an additional uncertainty for the Preston tube measurements of skin friction coefficient made in this region exists. However, as shown later, the inner layer develops quickly, and all of the Preston tube measurements, with the exception of those made at the first smooth plate, are considered to be valid determinations with uncertainties of ±6 percent (Coleman et al.,1988).

Temperature Profile Measurements

A Type E (chromel-constantan) butt-welded, 0.25 mm diameter thermocouple probe was used to measure the time mean temperature distribution across the boundary layer. The probe was mounted on the same micrometer arrangement used for the velocity profile measurements, and the method of traversing the thermal boundary layer was the same as the procedure for the hot-wire probe discussed previously. The probe was positioned in the freestream and the reference freestream temperature was measured. The probe was then lowered to a position 1.19 mm above the wall for the initial measurement. Measurements were taken throughout the thermal boundary layer until the freestream was reached. The probe output, in millivolts, was converted to temperature using Hewlett-Packard software. The uncertainty associated with the temperature measurements was determined to be ± 0.09 °C (Coleman et al., 1988).

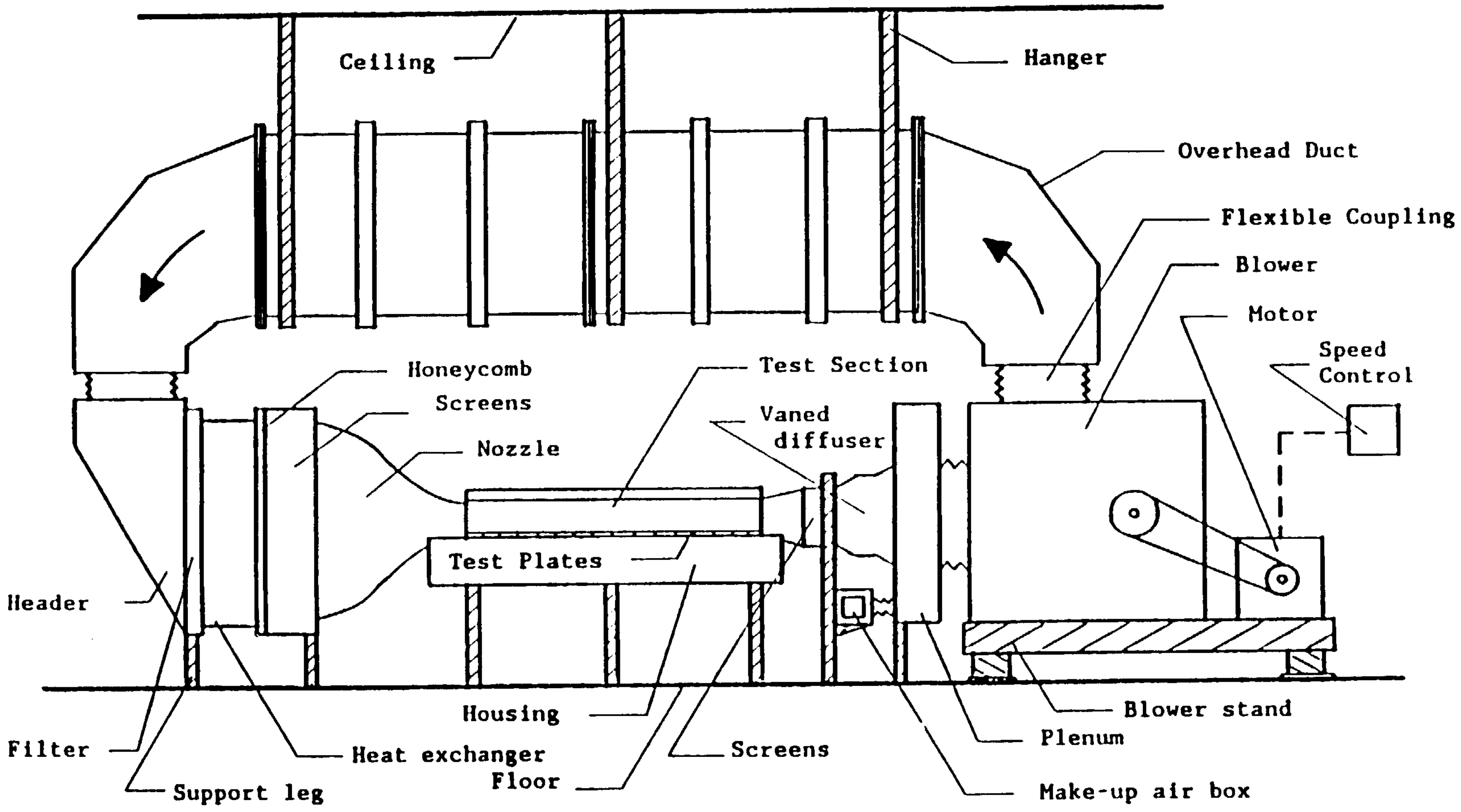

Figure 2. Schematic of the Turbulent Heat Transfer Test Facility (THTTF).

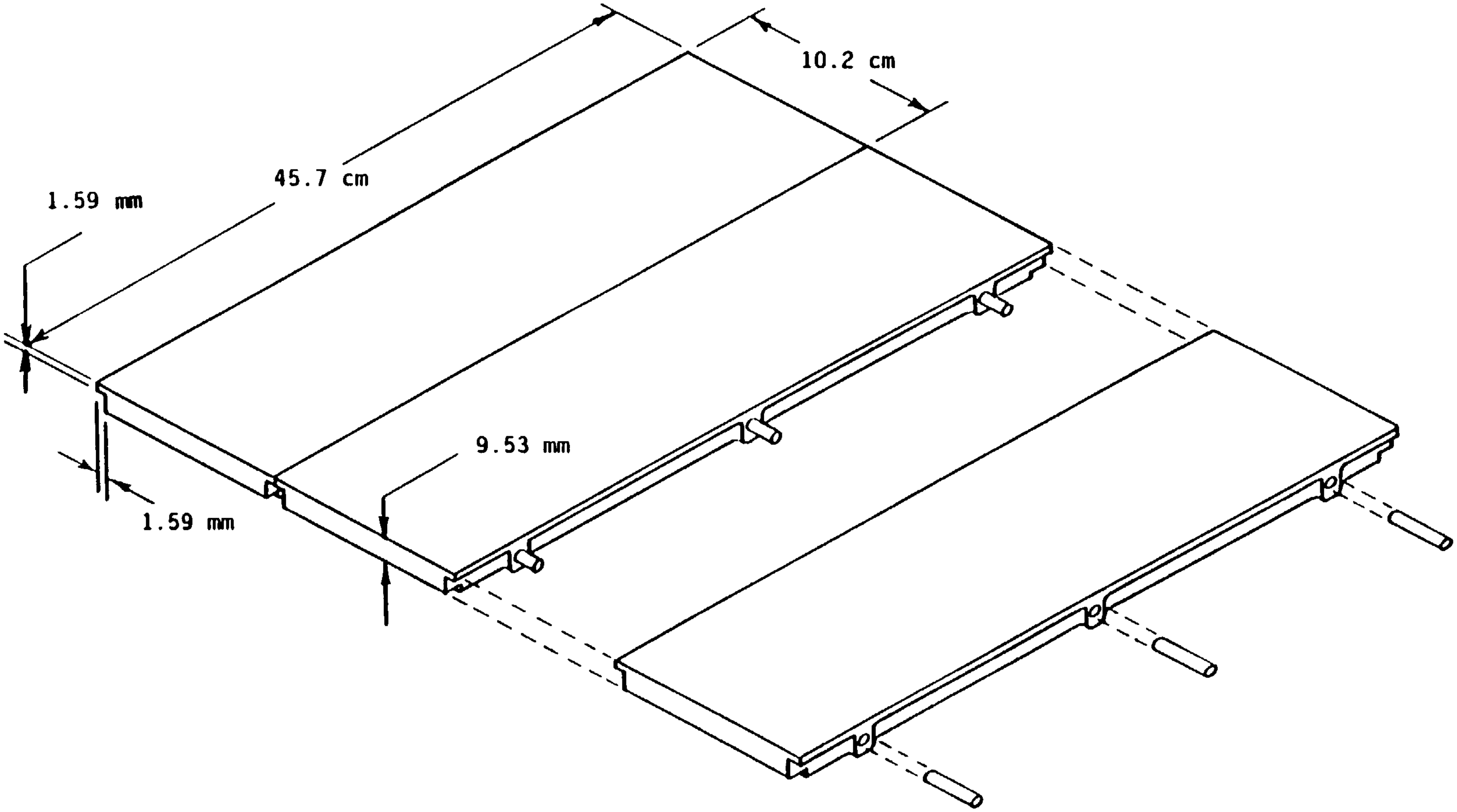

Figure 3. Exploded view of the THTTF test surface assembly.

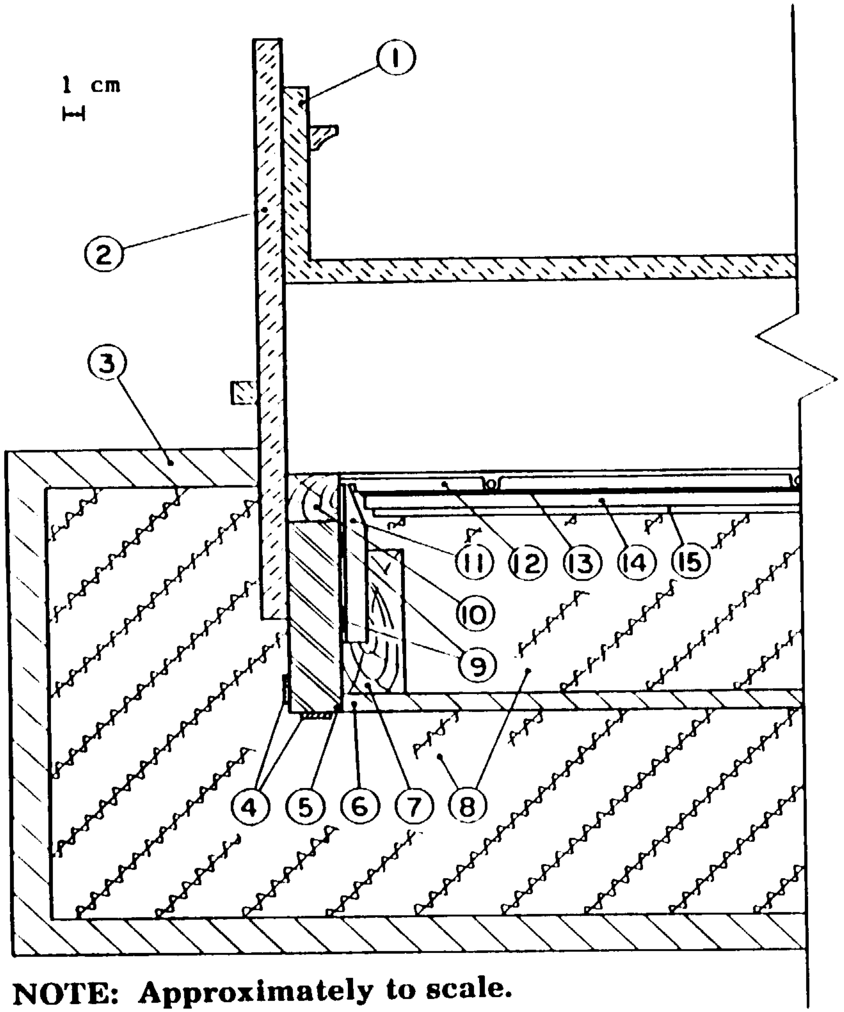

NOTE: Approximately to scale.

1. **Top Wall Assembly**
2. **Tunnel Side Wall**
3. **Wooden Housing**
4. **Side Rail Heaters**
5. **Steel Side Rail**
6. **Wooden Section Closure**
7. **Wooden Beam**
8. **Thermal Insulation**
9. **Birch Strips**
10. **Balsa Strip**
11. **Precision Straight Edge**
12. **Aluminum Test Plate**
13. **Heater Pad**
14. **Insulation Pad**
15. **Aluminum Backing Plate**

Figure 4. Cross section of the THTTF test section.

CHAPTER III

HEAT TRANSFER RESULTS

This chapter presents the experimental heat transfer results for zero pressure gradient, constant wall temperature, incompressible turbulent boundary layer flow with freestream velocities of 6, 12, 27, 43, 58, and 66 m/s and a nominal wall temperature of 44 C for both the base-aligned and crest-aligned cases. The main emphasis of the results is the Stanton number measurements in the Turbulent Heat Transfer Test Facility (THTTF) for the two alignments. Furthermore, the behavior of thermal boundary layer thickness and enthalpy thickness is also investigated.

The Stanton number data were determined from energy balances on each test plate, as outlined in Appendix A. Using the ANSI/ASME Standard on Measurement Uncertainty (1986) and following the procedures of Coleman and Steele (1989), the uncertainty in the experimentally determined Stanton number was estimated. As discussed in detail in Appendix A, the overall uncertainty for the Stanton number data ranged from about ±2 percent to ±5 percent for the 0.1 m plates, depending upon freestream velocity. The overall uncertainty in Stanton number associated with the narrower 0.025 m smooth plates at the rough-to-smooth interface ranged from ±4 percent to ±11 percent, depending upon freestream velocity. The plots of Stanton numbers presented in this chapter include uncertainty bars on various data points which show the typical overall uncertainty limits on Stanton numbers.

Temperature profiles of the thermal boundary layer were measured with the thermocouple probe, as described in Chapter II, for freestream velocities of 6, 12, 27, 43, 58, and 66 m/s. The profiles were taken at a location 0.94 m downstream of the test surface leading edge. This location is just downstream of the rough-to-smooth interface. For the base-aligned tests, additional temperature profiles for freestream velocities of 12 and 58 m/s were measured at locations 0.94 m, 1.05 m, 1.15 m, 1.35 m, and 1.55 m downstream from the leading edge. These temperature profiles were used to determine the thermal boundary layer thicknesses. The enthalpy thickness corresponding to each Stanton number was determined by numerically integrating the energy integral equation [Kays and Crawford (1980)].

$$\Delta_2 = \int_0^x St(x)\,dx \tag{2}$$

Base-Aligned Case

Figures 5 through 10 present the base-aligned Stanton number data plotted versus Re_x for nominal freestream velocities of 6, 12, 27, 43, 58, and 66 m/s, respectively. The corresponding x-Reynolds numbers range from 100,000 to 10 million. The x-Reynolds number immediately downstream of the step ranges from 300,000 to 3,000,000. Also shown on these plots is the corresponding THTTF heat transfer data for a smooth surface over the entire 2.4 m length of the test section (Coleman et al., 1988). For the 6 m/s case shown in Figure 5, a line representing the smooth wall case for turbulent boundary layers (Coleman et al.,1988)

$$St = 0.185\,[\,\log_{10}(Re_x)\,]^{-2.584}\,Pr^{-0.4} \tag{3}$$

was plotted for comparison since no smooth-wall data were taken for 6 m/s. These figures show that the step change from a rough surface to a smooth surface has an immediate and large effect on the heat transfer. For each of the freestream velocities the Stanton number rapidly approaches the smooth wall case. In most of the cases, the Stanton number immediately after the step change in roughness falls below the corresponding smooth-wall values and rises back to the smooth-wall values further downstream of the interface.

The $U_\infty = 6$ m/s case shown in Figure 5 behaves differently. In spite of the trip at the nozzle exit and the rough surface, the flow remains laminar for a considerable length. The flow becomes fully turbulent at a Reynolds number of about 200,000, and a transitionally rough boundary layer is established for a short distance before the rough-to-smooth interface. According to Hosni et al. (1989) this case is transitionally rough[1] in the aerodynamic sense while the higher velocities are fully rough boundary layers over the rough portion of the test surface. In the region between the rough-wall boundary layer and the developing smooth-wall boundary layer, the Stanton number decreases rapidly in a smooth, continuous fashion to the new smooth-wall condition. For a freestream velocity of 12 m/s shown in Figure 6, the Stanton number drops immediately to the smooth-wall condition. There appears to be a slight dip in the rough-to-smooth Stanton number below the all smooth-wall Stanton number data. Freestream velocities of 27 and 43 m/s shown in Figures 7 and 8, respectively, have

---

[1]. Turbulent flows which are influenced by surface roughness are usually divided into 3 regimes. Aerodynamically smooth flows are those where the roughness effects are so small that the flow behaves as if the wall were smooth. Fully rough flows are those where the roughness so dominates the momentum transport to the wall that viscous effects are negligible. In turbulent pipe flow fully rough flows are those where the friction factor is no longer a function of the Reynolds number. Transitionally rough flows are those at Reynolds numbers between, where viscous and roughness effects are both important.

an immediate drop in the Stanton number after the rough-to-smooth interface. Both cases show a definite dip in the Stanton number below the equivalent smooth-wall values after the step change in surface roughness. At the higher velocities of 58 and 66 m/s shown in Figures 9 and 10, the change in the Stanton number to the smooth-wall case is still immediate; however, the dip below the equivalent smooth-wall data is weaker than for the 27 and 43 m/s cases.

Overall, the transitionally rough flow has a smooth continuous change in the Stanton number from the rough surface region to the smooth surface region. Fully rough cases, however, have an immediate abrupt change in the Stanton number after the rough-to-smooth interface, with the Stanton numbers after the interface falling below the equivalent all smooth-wall values. As the freestream velocity increases, the change becomes slightly more abrupt.

Figures 11 and 12 show plots of the non-dimensional temperature profiles versus y/Δ for freestream velocities of 12 and 58 m/s for the base-aligned case. These plots show that the near wall region of the thermal boundary layer downstream of the rough-to-smooth interface rapidly takes on the smooth-wall profile characteristics. The outer regions of the profiles further downstream of the interface gradually approach the all smooth-wall case.

Figure 13 shows the temperature data for $U_\infty = 12$ m/s plotted in T^+ versus y^+ coordinates. Also shown on this figure is the law of the wall for the thermal boundary layer for a smooth wall as given by Kays and Crawford (1980)

$$T^+ = 2.195 \ln(y^+) + 13.2 Pr - 5.66 \tag{4}$$

The first smooth-wall T^+ profile immediately after the roughness interface is much like the last rough-wall profile. The profiles further downstream of the interface approach the smooth-wall T^+ levels. The uncertainties in the T^+ values are relatively large.

Figures 14 and 15 show plots of enthalpy thickness versus x for the base-aligned cases at 12 and 58 m/s. The corresponding all-rough data reported by Hosni (1989) are also shown. The enthalpy thickness after the step continues to grow; however, the growth rate is less than that a completely rough test surface.

Alignment Comparison

A direct comparison of the Stanton number data for the two alignments is shown in Figures 16 through 21. For the 6 and 12 m/s cases, results are indistinguishable from each other within the data uncertainty. The data at the rough-to-smooth interface exhibit the same behavior for both the base-aligned and crest-aligned cases. For the 27 m/s case, the Stanton number for the crest-aligned case on the first 0.025 m smooth test plate is slightly larger than its base-aligned counterpart; however, there is a large overlap of the uncertainty intervals. The same behavior is seen at the higher freestream velocities of 43, 58, and 66 m/s, with the first crest-aligned Stanton number after the interface slightly larger than its base-aligned equivalent with a small amount of overlap of the uncertainty bands. This effect is not seen for any test plate Stanton numbers further downstream of the first smooth-wall plate regardless of freestream velocity. For the conditions of these experiments, any effect of surface alignment is very small and observed only in the region immediately downstream of the step change in surface roughness.

As stated earlier, for the crest-aligned case mean temperature profiles were measured at an x-location 0.04 m downstream of the rough-to-smooth interface for all freestream velocities. Figure 22 shows a comparison of the mean temperature profile at this location for each of the two alignments at a freestream velocity of 12 m/s. There is no real discernable difference between the two profiles of either alignment. Figure 23 shows the same plot for a freestream velocity of 58 m/s.

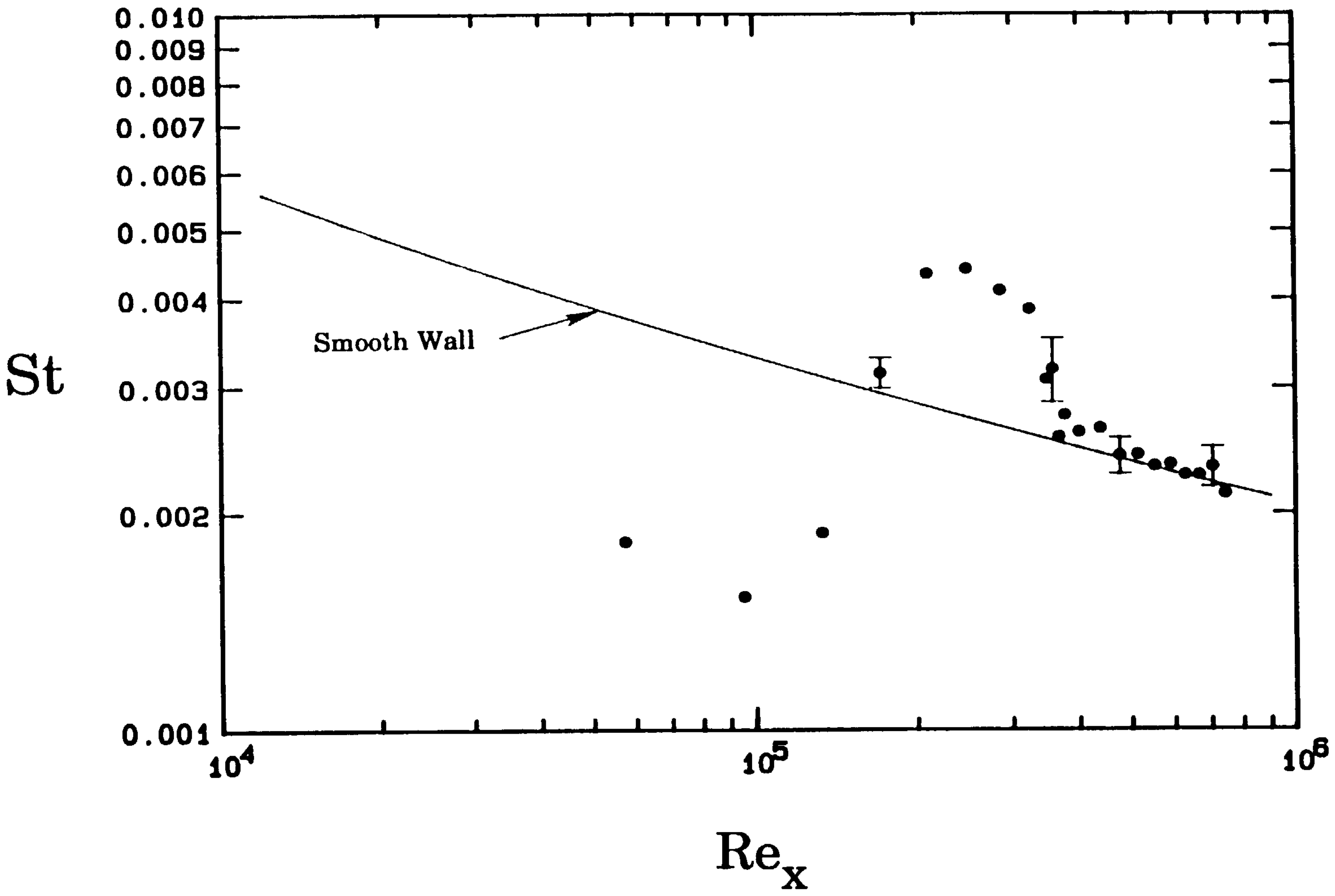

Figure 5. Stanton number data versus Re_x for the base-aligned case for $U_\infty = 6$ m/s.

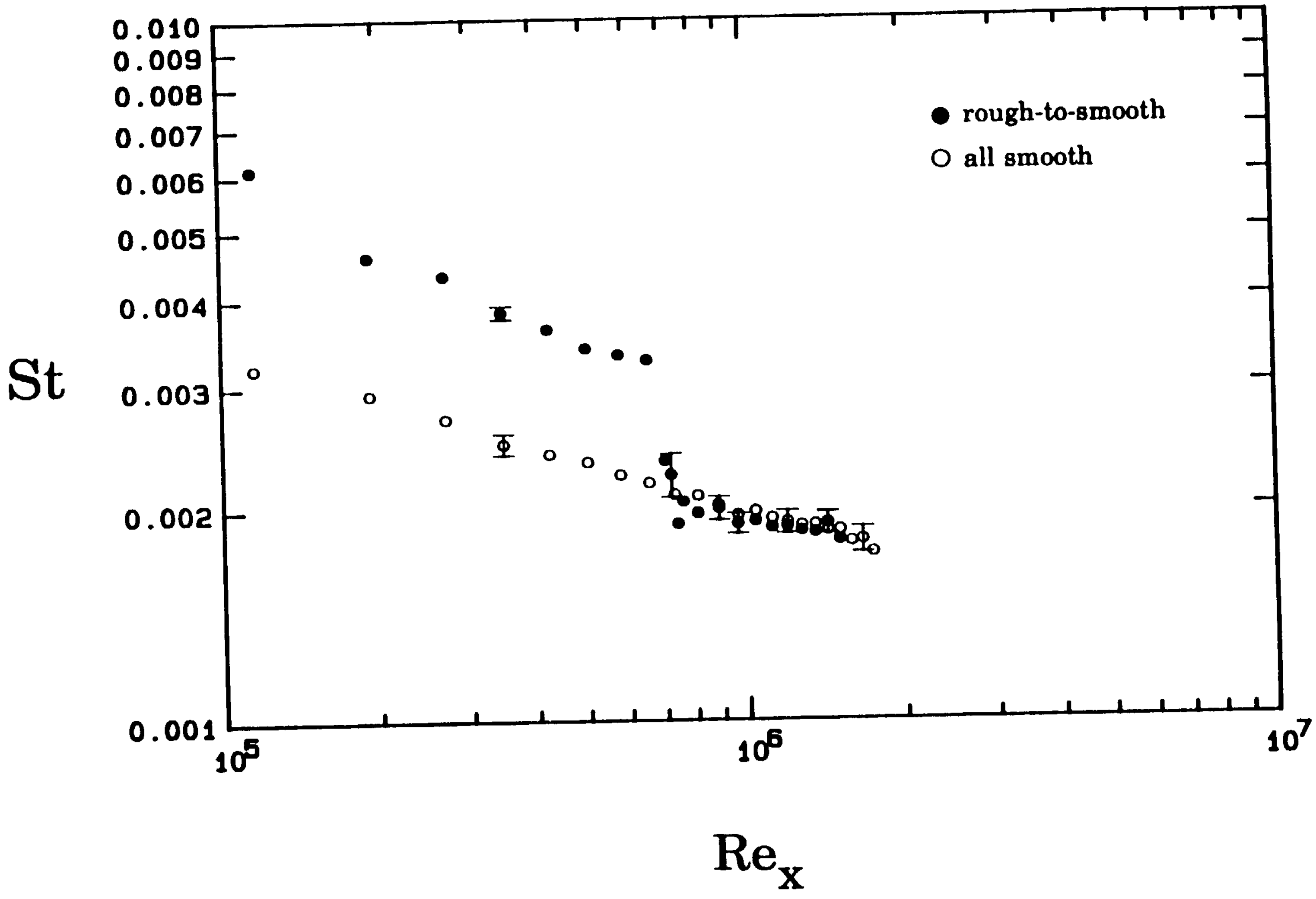

Figure 6. Stanton number data versus Re_x for the base-aligned case for U_∞ = 12 m/s.

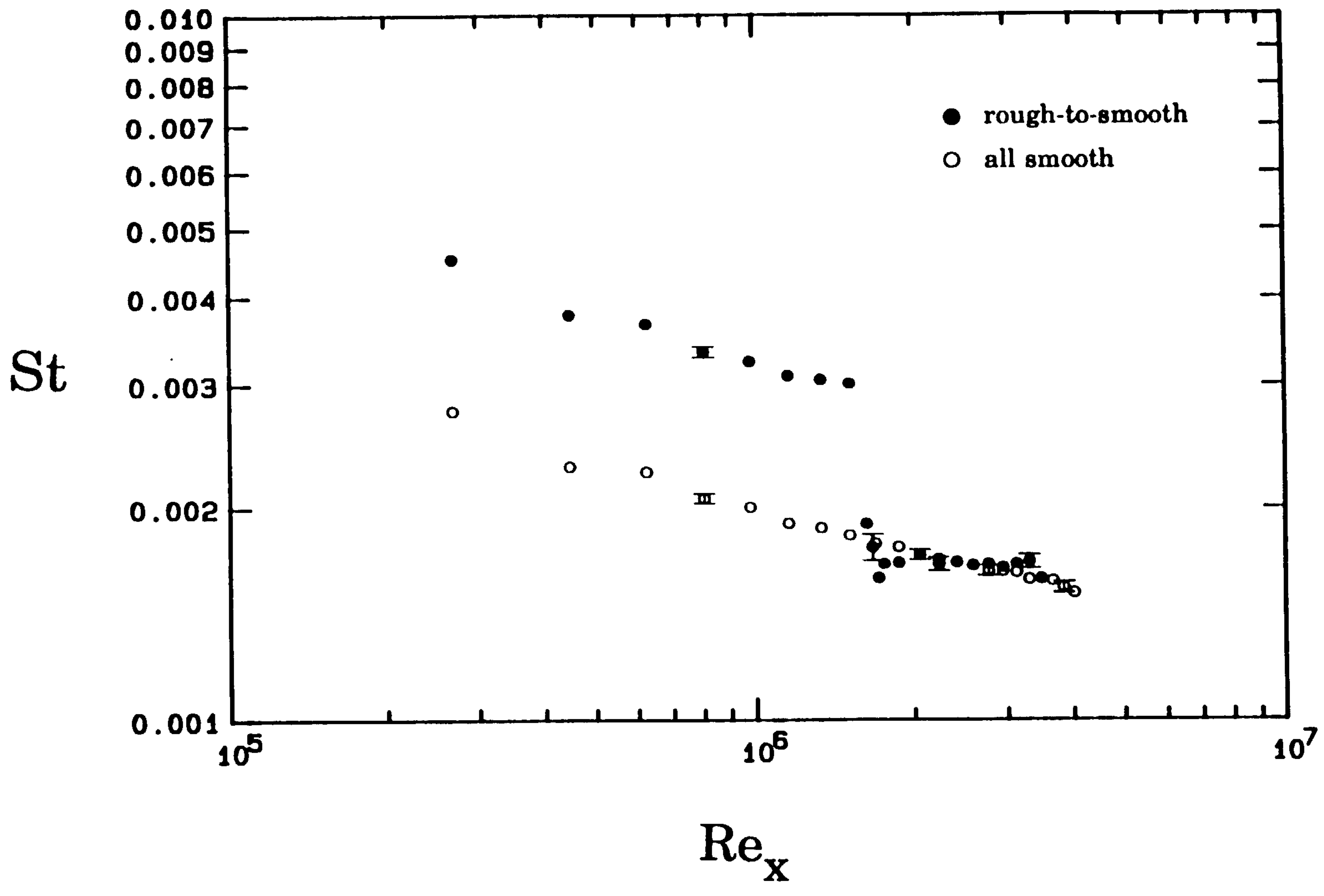

Figure 7. Stanton number data versus Re_x for the base-aligned case for U_∞ = 27 m/s.

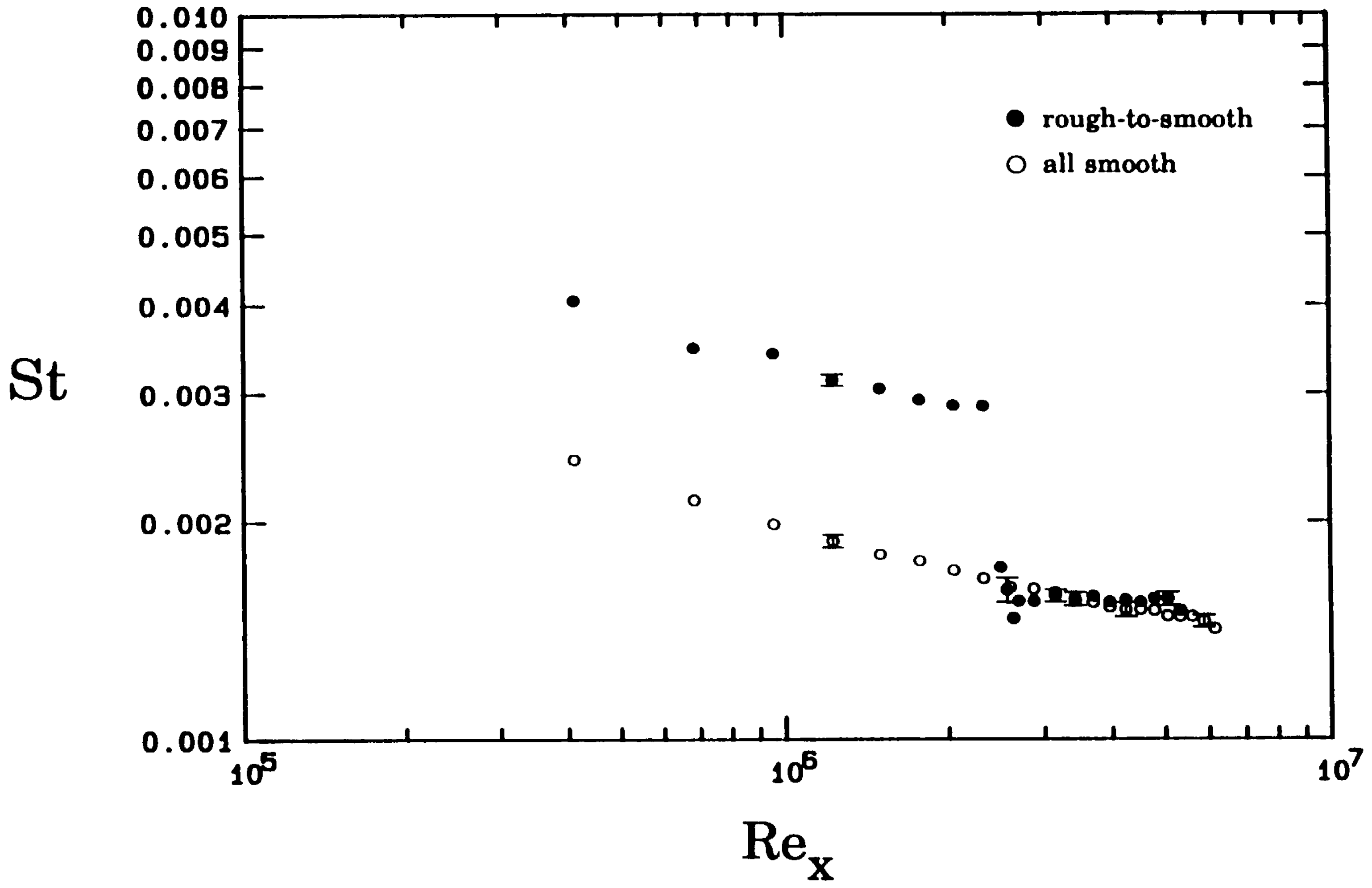

Figure 8. Stanton number data versus Re_x for the base-aligned case for $U_\infty = 43$ m/s.

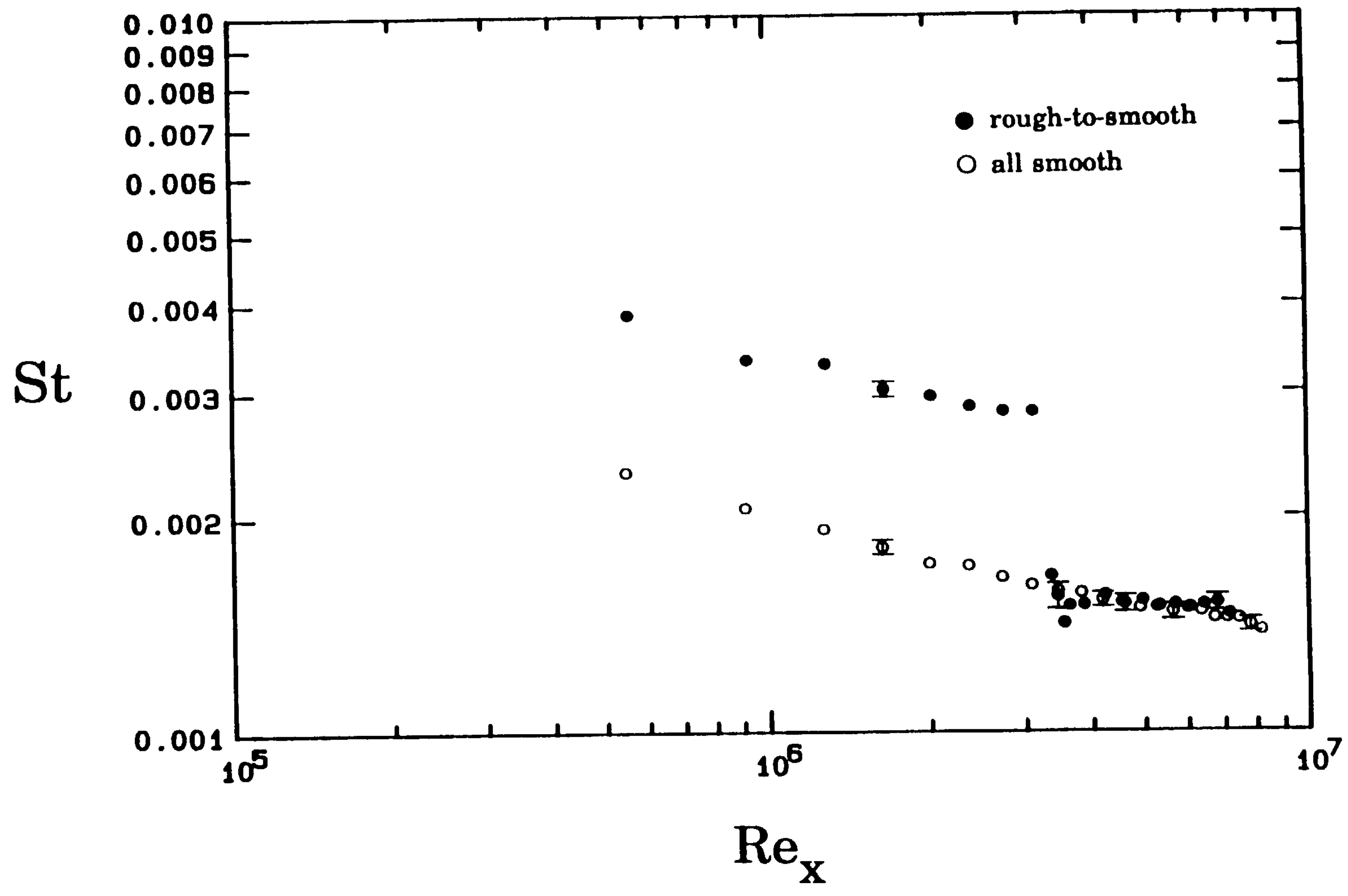

Figure 9. Stanton number data versus Re_x for the base-aligned case for U_∞ = 58 m/s.

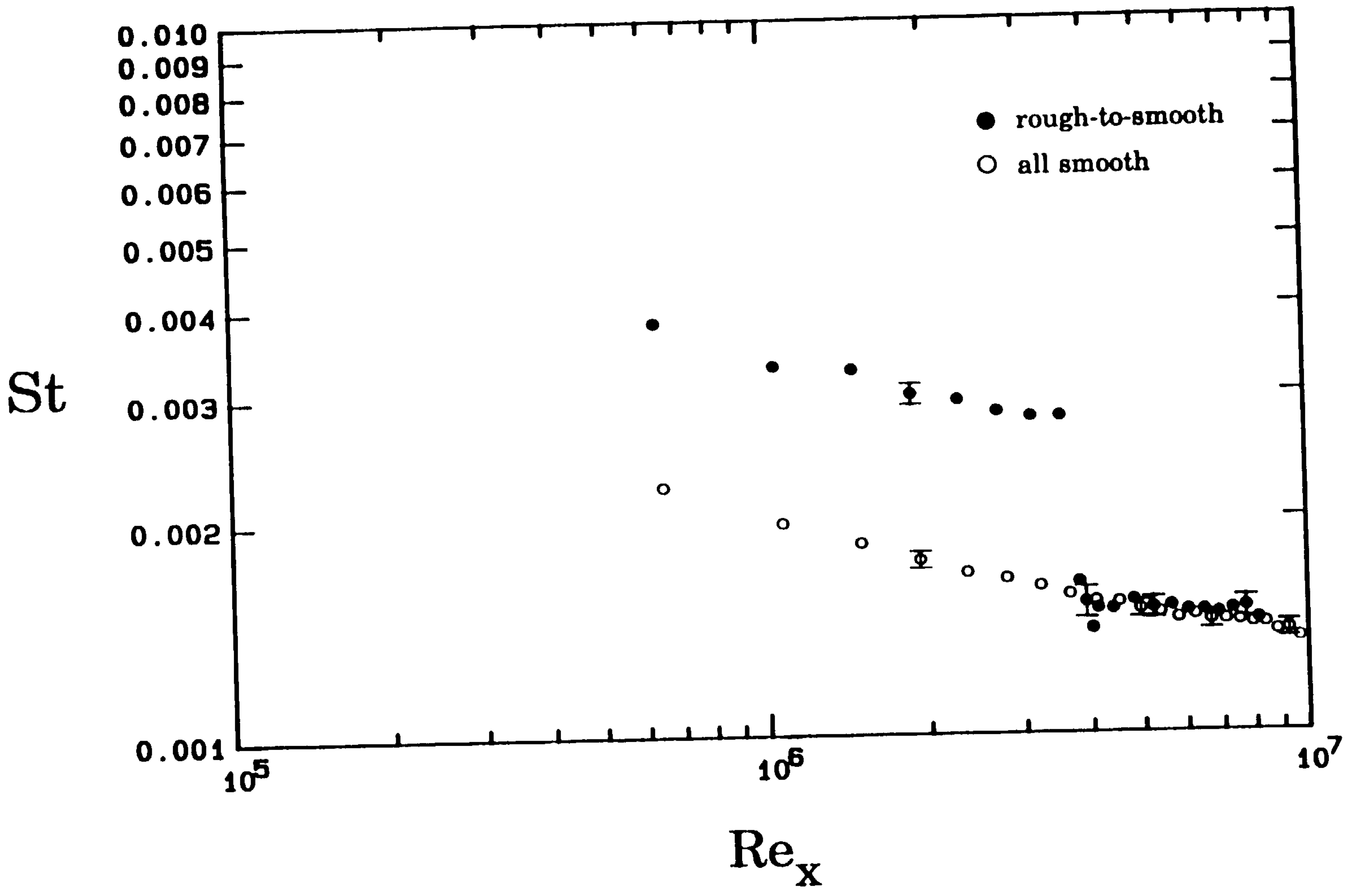

Figure 10. Stanton number data versus Re_x for the base-aligned case for U_∞ = 66 m/s.

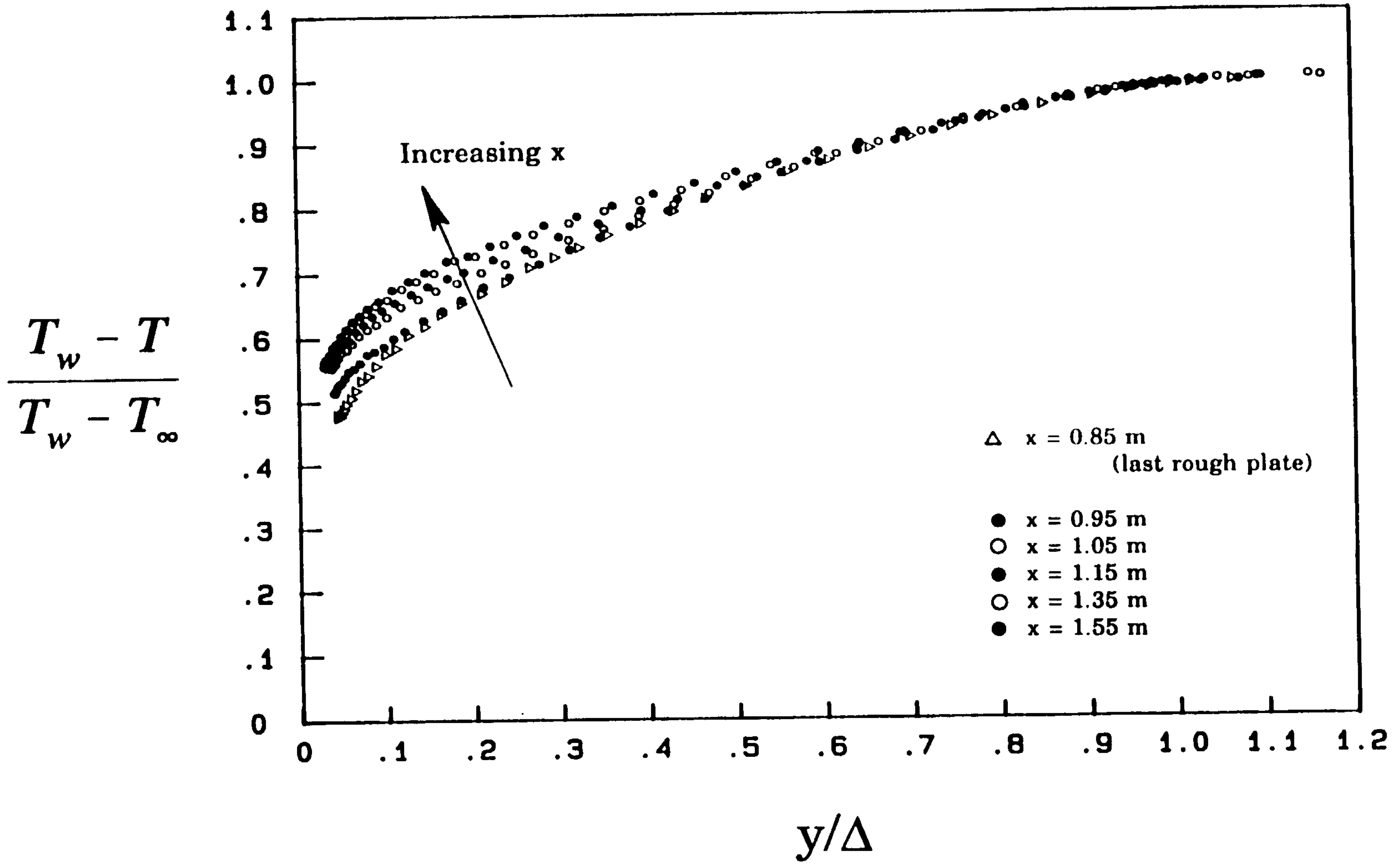

Figure 11. Nondimensional temperature profiles versus y/Δ for U_∞ = 12 m/s for the base-aligned case.

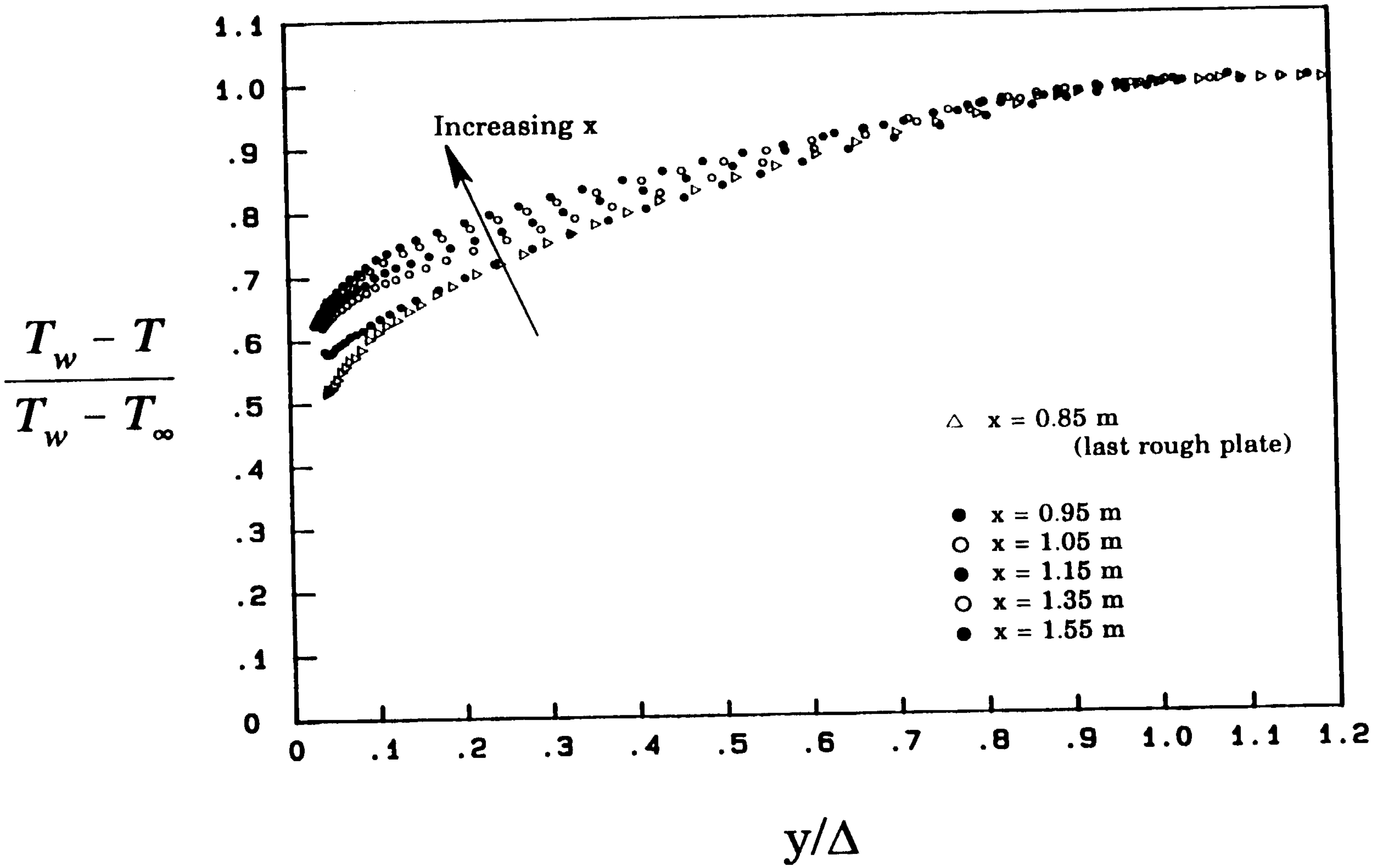

Figure 12. Nondimensional temperature profiles versus y/Δ for U_∞ = 58 m/s for the base-aligned case.

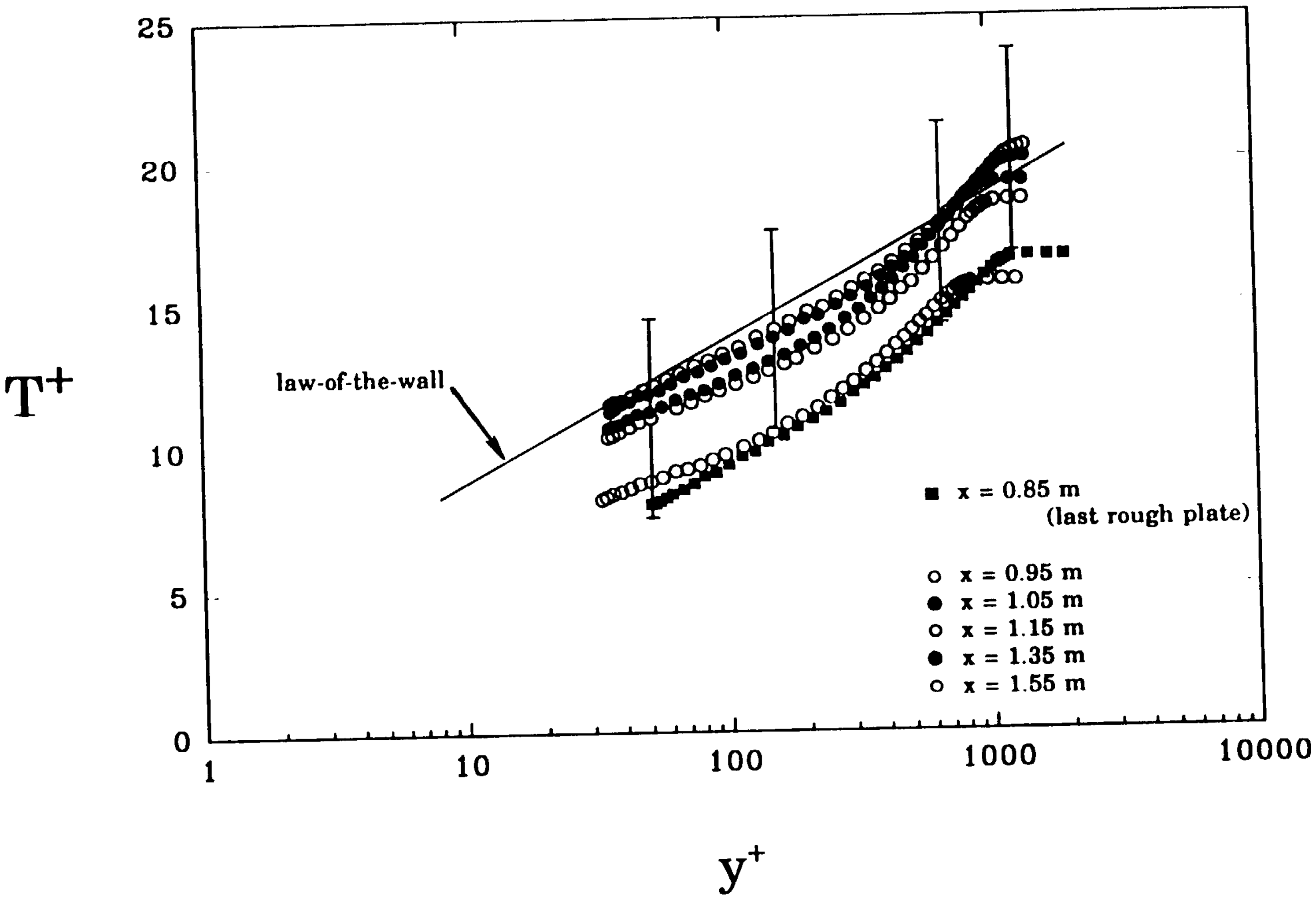

Figure 13. Temperature profiles at U_∞ = 12 m/s for the base-aligned case compared with the thermal law of the wall.

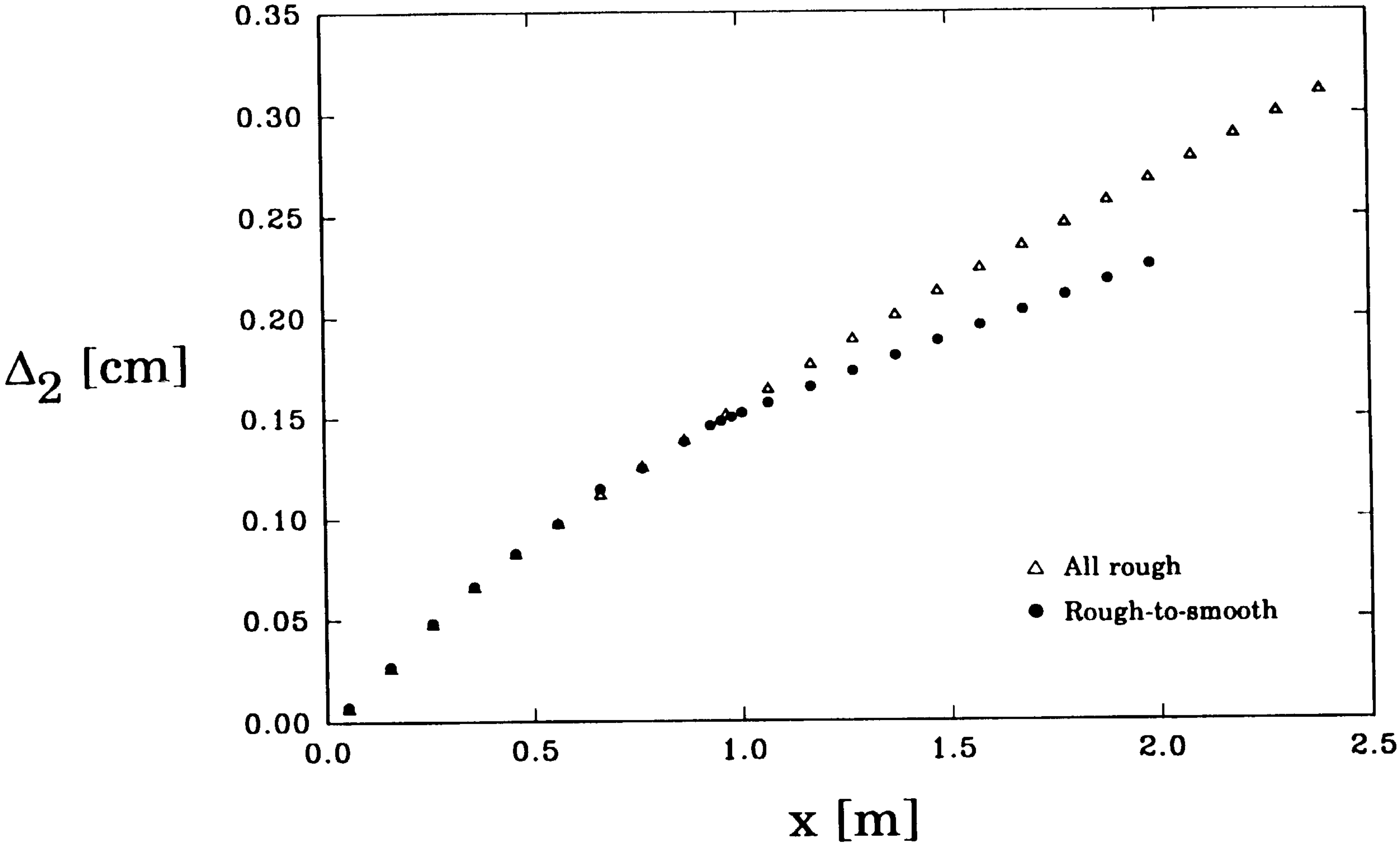

Figure 14. Enthalpy thickness versus x for the base-aligned case for $U_\infty = 12$ m/s compared with the all-rough case.

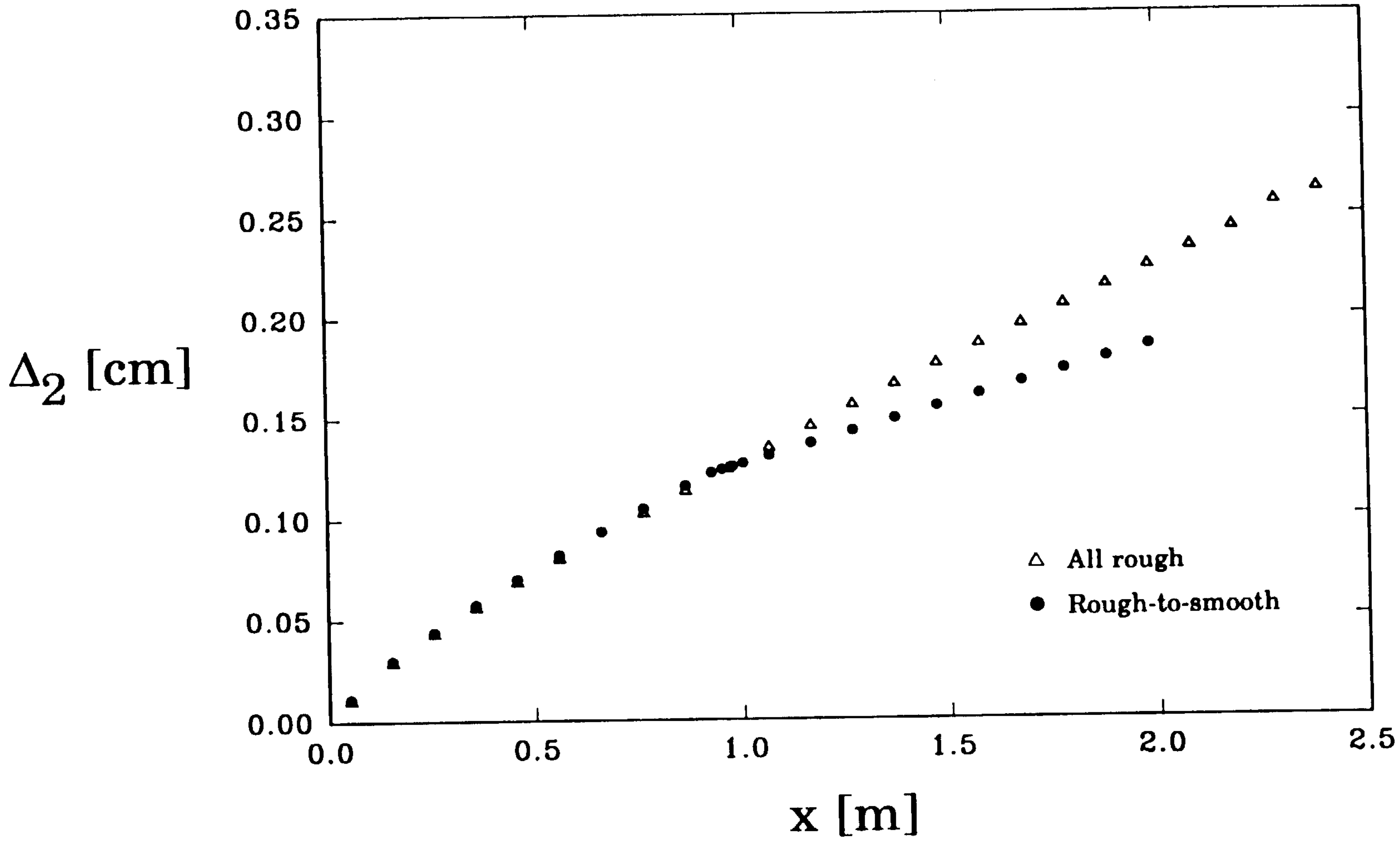

Figure 15. Enthalpy thickness versus x for the base-aligned case for $U_\infty = 58$ m/s compared with the all-rough case.

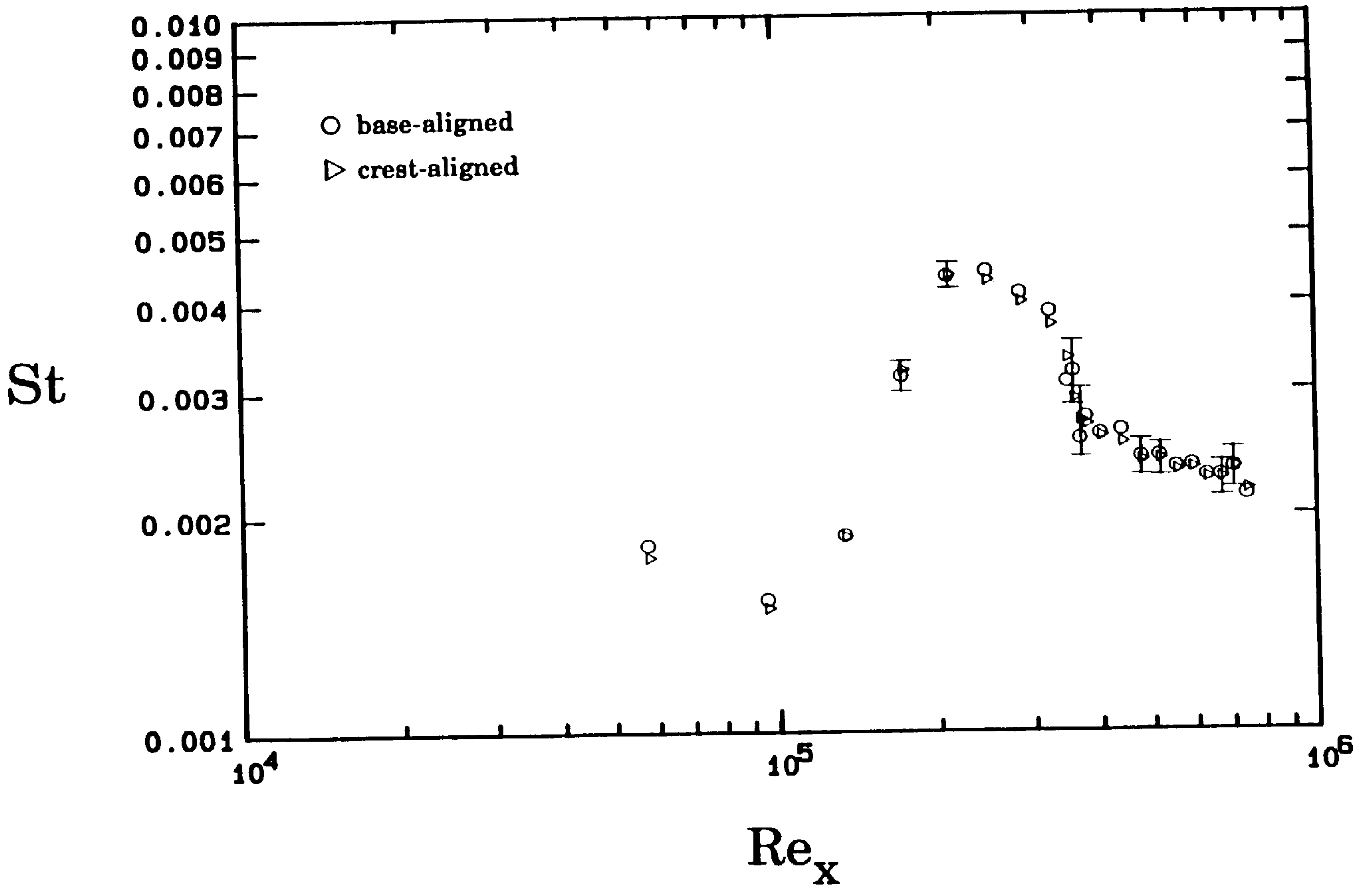

Figure 16. Comparison of Stanton number data versus Re_x for the base-aligned and crest-aligned cases for $U_\infty = 6$ m/s.

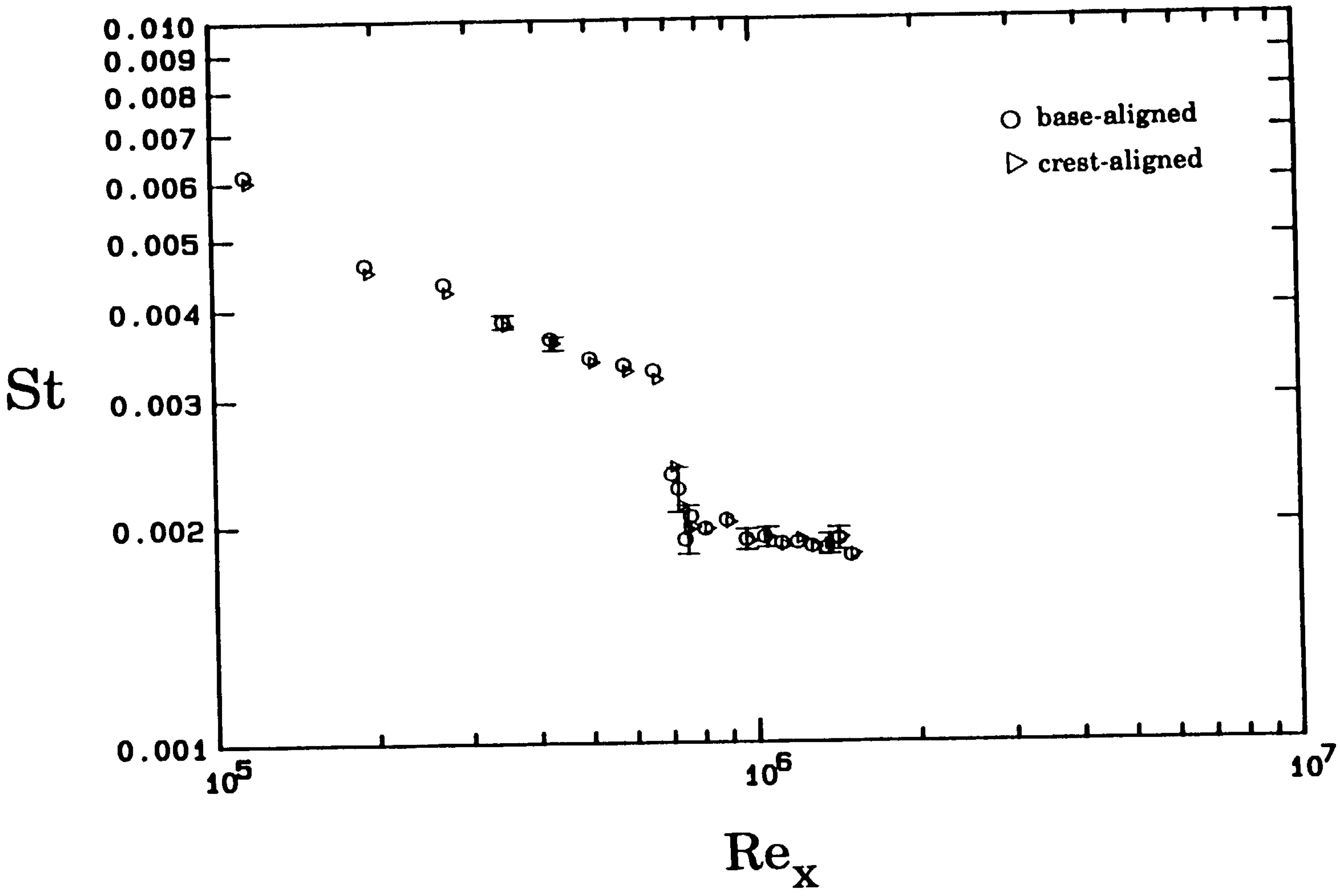

Figure 17. Comparison of Stanton number data versus Re_x for the base-aligned and crest-aligned cases for U_∞ = 12 m/s.

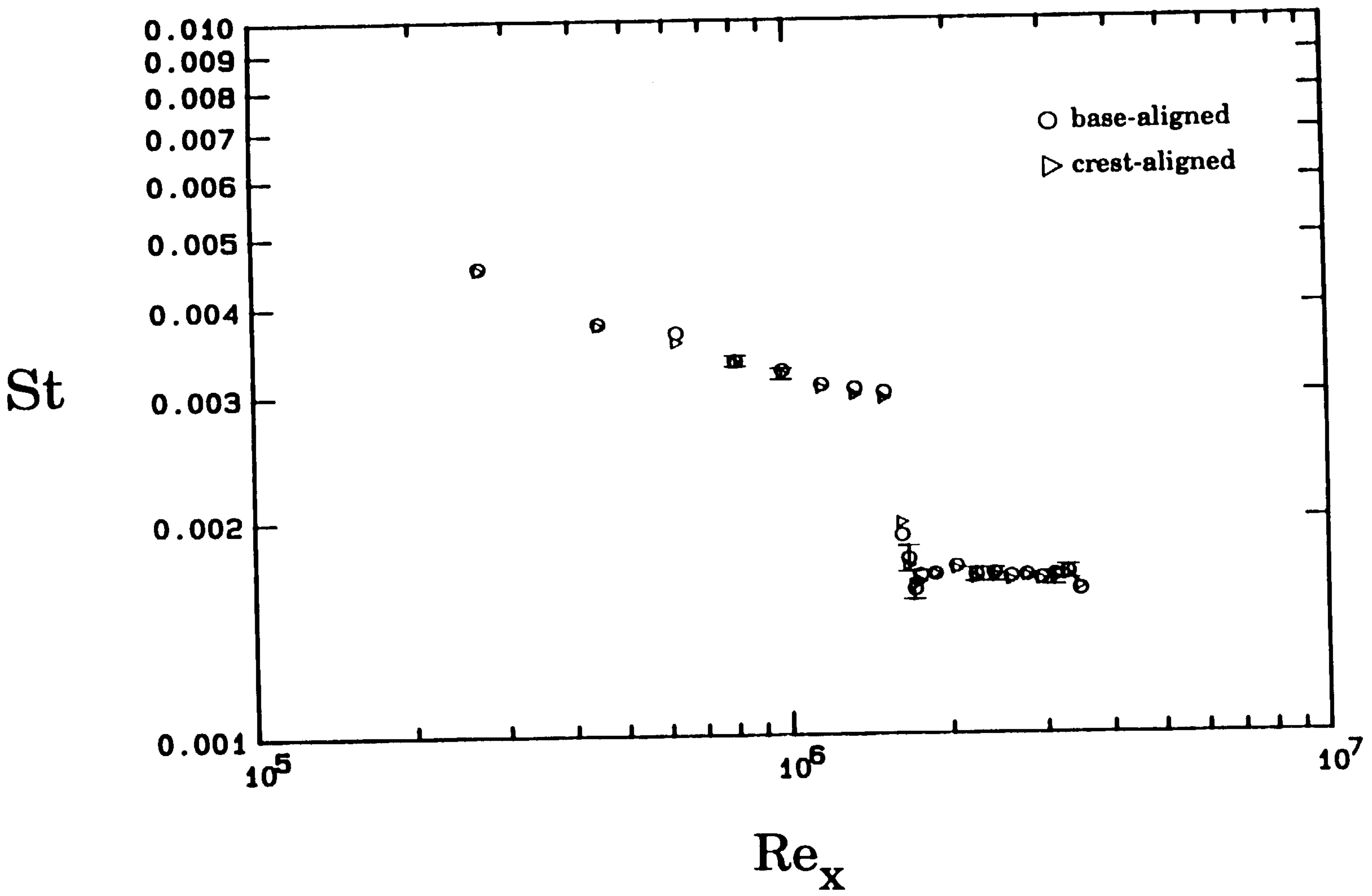

Figure 18. Comparison of Stanton number data versus Re_x for the base-aligned and crest-aligned cases for U_∞ = 27 m/s.

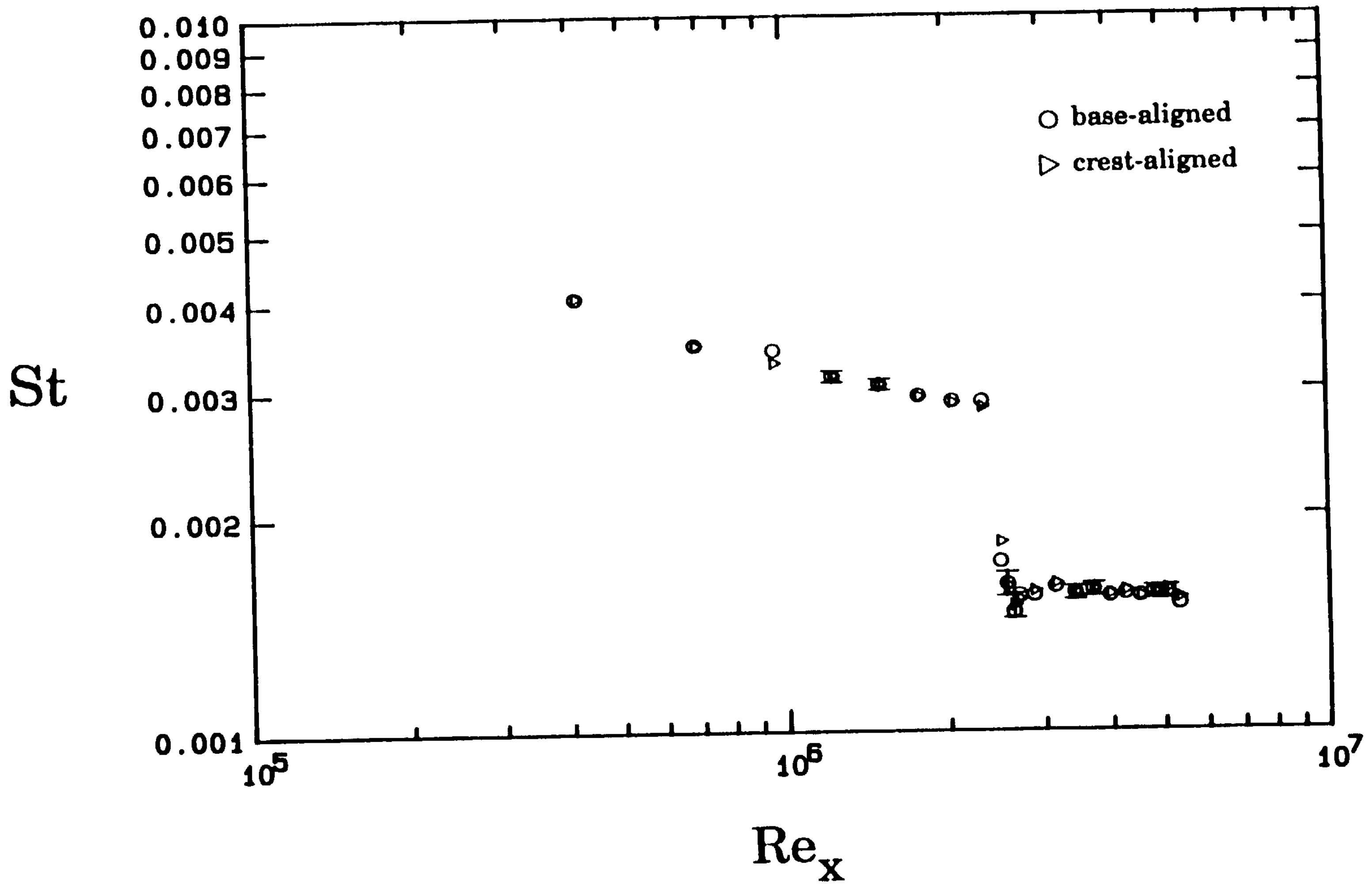

Figure 19. Comparison of Stanton number data versus Re_x for the base-aligned and crest-aligned cases for U_∞ = 43 m/s.

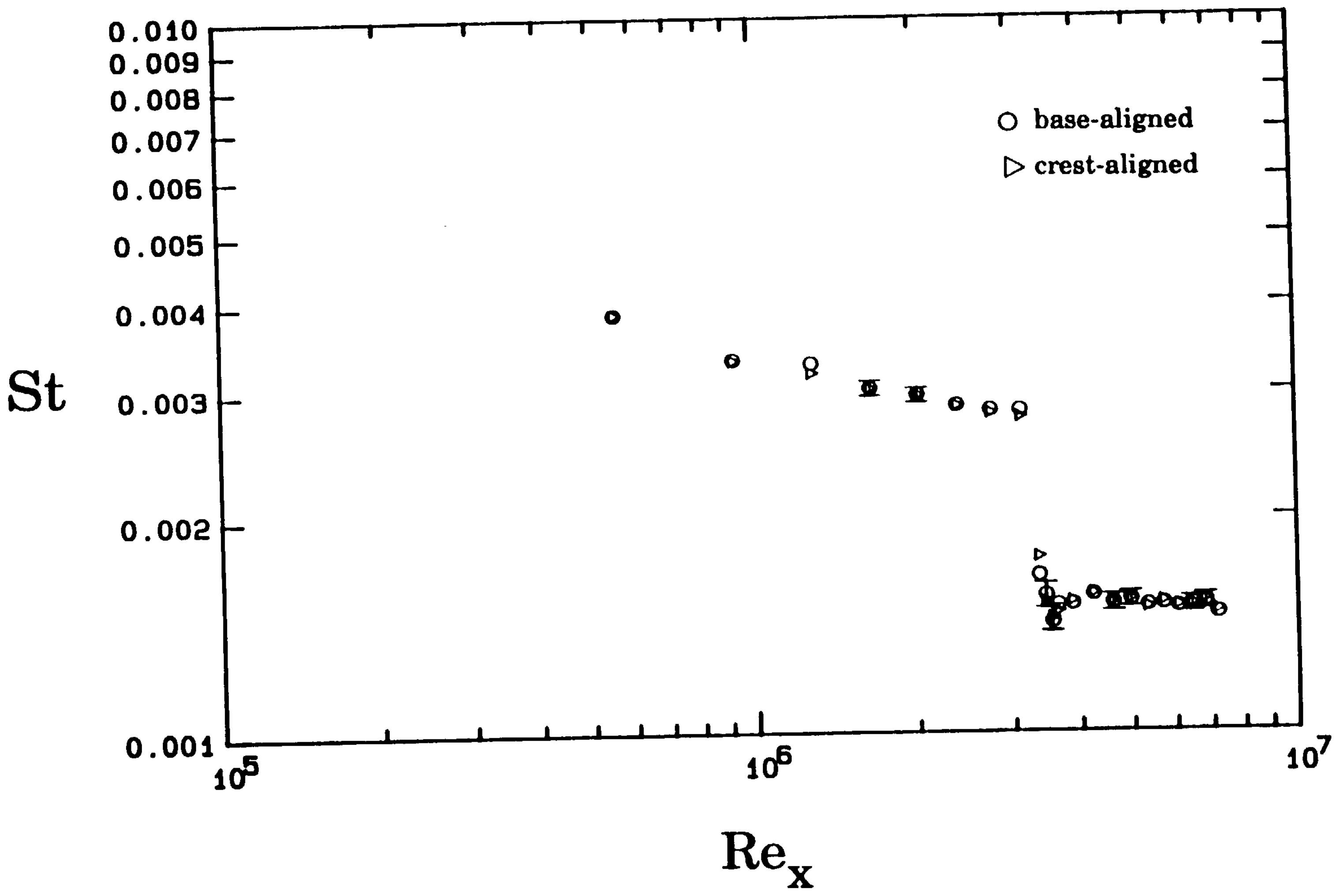

Figure 20. Comparison of Stanton number data versus Re_x for the base-aligned and crest-aligned cases for U_∞ = 58 m/s.

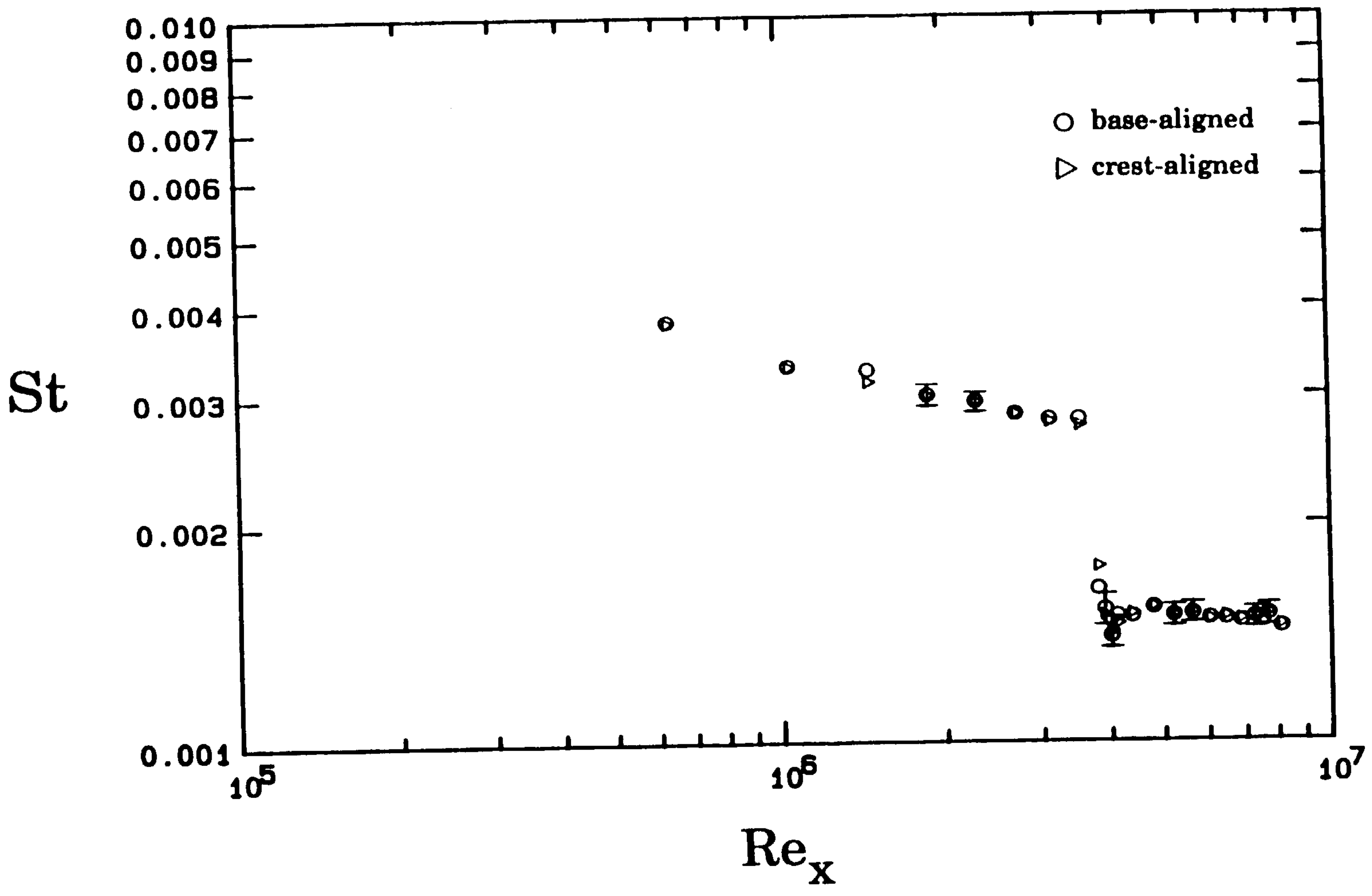

Figure 21. Comparison of Stanton number data versus Re_x for the base-aligned and crest-aligned cases for U_∞ = 66 m/s.

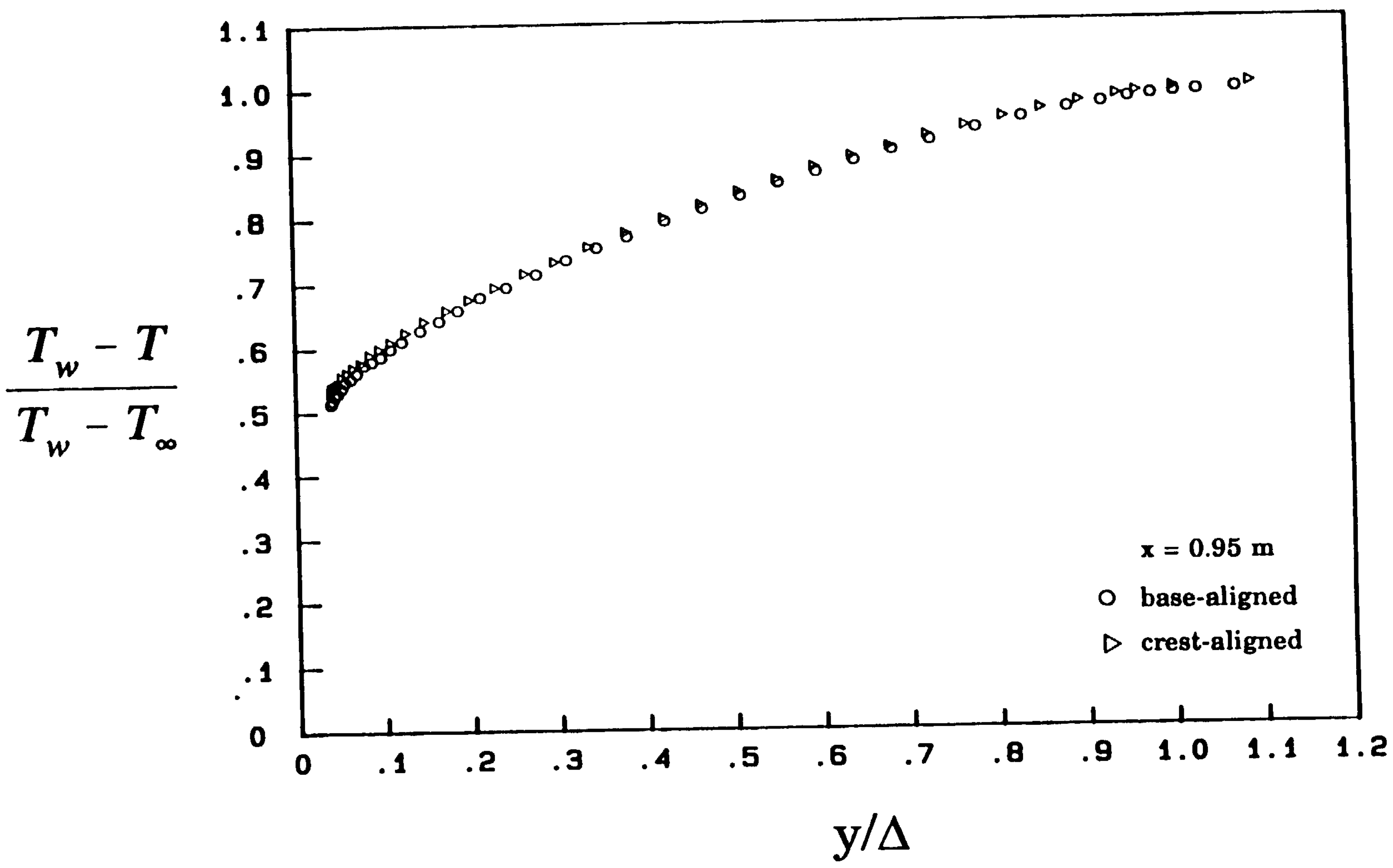

Figure 22. Comparison of the nondimensional temperature profiles versus y/Δ for the base-aligned and crest-aligned cases for U_∞ = 12 m/s.

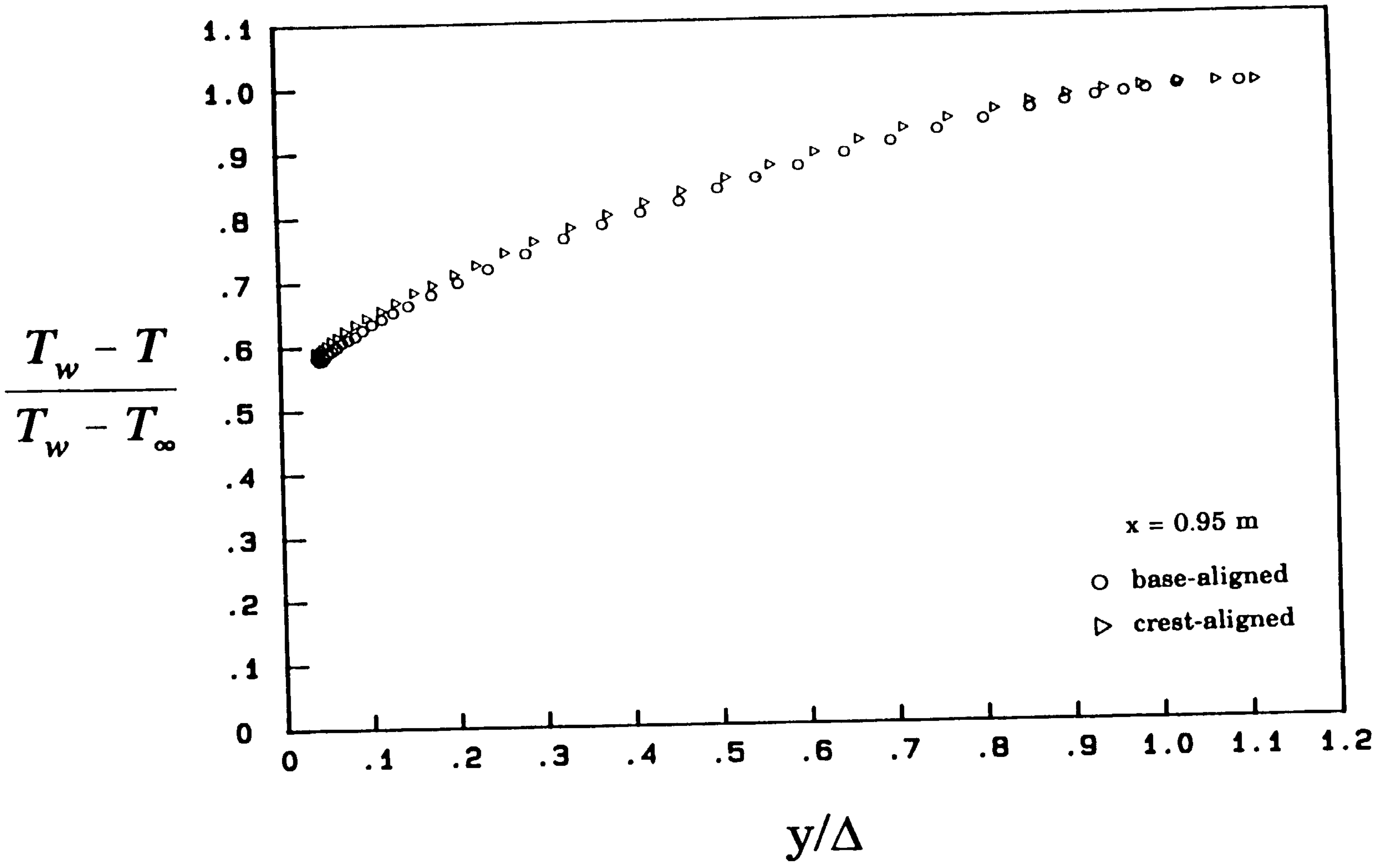

Figure 23. Comparison of the nondimensional temperature profiles versus y/Δ for the base-aligned and crest-aligned cases for U_∞ = 58 m/s.

CHAPTER IV

FLUID MECHANICS RESULTS

This chapter presents the fluid mechanics results obtained in the boundary layer over the rough to smooth surface for both the base-aligned and the crest-aligned cases. All of the fluid dynamics results are for zero pressure gradient, isothermal, incompressible boundary layer flows. Profiles of mean velocity and the turbulence intensity quantity $\overline{u'^2}$ were measured with a horizontal hot-wire using the techniques outlined in detail by Hosni et al. (1989). These profiles were used to obtain the boundary layer thickness, displacement thickness, and momentum thickness along the rough-to-smooth surface. The skin friction coefficient distribution was obtained using the Preston tube method. All of the data obtained are compared with previously reported THTTF data for all-rough and all-smooth surfaces.

Base-Aligned Case

Boundary layer velocity profiles and boundary layer integral parameters such as the boundary layer thickness (δ), the displacement thickness (δ_1), and the momentum thickness (δ_2) were obtained for the rough to smooth surface at nominal freestream velocities of 12 and 58 m/s. These profiles were measured at locations of 0.95 m, 1.05 m, 1.15 m, 1.35 m, 1.55 m, 1.75 m, and 1.95 m downstream of the test section leading edge, for the base aligned case, with the rough-to-smooth interface located at 0.90 m.

Figure 24 shows a plot of the rough-to-smooth velocity profiles in u/U_∞ versus y/δ coordinates taken with a hot-wire at a nominal freestream velocity of 12 m/s. Also included on the plot is the velocity profile for the last rough plate, x = 0.85 m. This plot shows the profile immediately downstream of the rough-to-smooth interface quickly assumes the smooth-wall characteristics in the near-wall region, but resembles the rough-wall profile in the wake region. Further downstream of the step, the profiles gradually assume a smooth-wall shape. Figure 25 shows a composite plot of the boundary layer mean velocity profiles taken with a hot-wire at a nominal freestream velocity of 12 m/s plotted in y versus u/U_∞ coordinates. The u/U_∞ abscissa is plotted with a multiple origin to show the progression of the velocity profiles downstream of the rough-to-smooth interface. The plot also shows the corresponding rough-wall velocity profiles under carefully matched flow conditions for the identical locations. This figure shows that after the interface, the velocity profile is quick to deviate from the rough-wall profile near the wall, however, there is quite a distance before the fully smooth wall profile is obtained.

Profiles of axial turbulence intensity were also determined with the horizontal hot-wire at the same locations downstream of the rough to smooth interface as the mean velocity profiles. Figure 26 shows the rough-to-smooth profiles of axial turbulence intensity normalized by U_∞ and plotted against the y-position normalized by the boundary layer thickness δ. For the 12 m/s profiles, the sharp near-wall peak typical for smooth-wall profiles is seen for all x locations except the x = 0.95 m location immediately after the step. Figure 27 shows the turbulence intensity profiles for a freestream velocity of 12 m/s plotted in coordinates y versus $\sqrt{\overline{u'^2}}\,/U_\infty$ on a multiple origin plot. Also shown on this plot are the rough-wall profiles for the same x-locations. The near-wall regions for the rough-to-smooth case quickly deviate from the all-rough scheme. However, the flow still has the rough-wall characteristics further out in the wake region for a considerable distance downstream.

Figure 28 shows a plot of δ versus x for a freestream velocity of 12 m/s. The boundary layer thickness, δ, is taken as the distance above the plate at which the boundary layer velocity was within 1 percent of the freestream velocity. This figure contrasts the boundary layer thicknesses for the all rough-wall and the rough-to-smooth cases. After the change in surface roughness, the boundary layer thickness grows at a slower rate than in the all-rough case.

The boundary layer displacement thickness was determined from numerical integration of the incompressible flow displacement thickness definition using the mean velocity profile data obtained with the horizontal hot-wire,

$$\delta_1 = \int_0^\infty \left[1 - \frac{u}{U_\infty}\right] dy \tag{5}$$

Likewise, the boundary layer momentum thickness was found by numerically integrating the incompressible flow momentum thickness definition using mean velocity profile data

$$\delta_2 = \int_0^\infty \frac{u}{U_\infty}\left[1 - \frac{u}{U_\infty}\right] dy \tag{6}$$

Figure 29 contrasts the boundary layer displacement thickness and momentum thickness for the all-rough and rough-to-smooth cases. While the all-rough displacement increased rapidly with x, the displacement thickness for the rough-to-smooth case remains more or less constant after the interface before slowly growing. After the rough-to-smooth interface, the momentum thickness closely follows the equivalent all-rough case for a substantial distance (0.4 m). After this distance, the rough-to-smooth case departs from the all-rough case with a slower growth rate. This effect is clearly seen in Figure 30. Figure 30 shows the nondimensional shape factor, $H = \delta_1/\delta_2$, versus x. There is a noticeable drop in the shape factor after the flow crosses the rough-to-smooth interface. The all-rough case has a more or less constant value for the shape factor equal to 1.6. The rough-to-smooth case, however, gradually falls toward the value of 1.3, the widely accepted value for the shape factor for a flat plate in turbulent flow. Antonia and Luxton (1972) reported the same behavior with shape factor in their experiments.

Antonia and Luxton (1971b) discussed, for a step change in surface roughness, the existence of two layers in the flow field downstream of the roughness interface. The boundary layer, δ, was defined previously to be the distance above the plate at which the boundary layer velocity was within 1 percent of the freestream velocity. An internal layer, δ_i, grows immediately downstream of the step due to the rapidly varying shear stress distribution. Shown in Figure 31, the flow outside the internal layer remains mostly unaffected by the change in surface roughness, while the flow inside the internal layer assumes a smooth-wall characteristic. Antonia and Luxton plotted their mean velocity profiles in u/U_∞ versus $y^{1/2}$ coordinates and showed that a "kink" or "knee" occurred in the plot at the edge of the internal layer. Figure 32 shows the mean velocity profiles for 12 m/s plotted in these coordinates with a shifted origin. Lines are drawn on the profiles to show quantitatively the location of the "kink" or "knee" point and, therefore, the internal layer thickness. Figure 33 shows a plot of the boundary layer thickness, δ, and the internal layer thickness, δ_i. The internal layer grows more rapidly than the boundary layer, since ultimately it will envelop the entire boundary layer. At x = 1.9 m the ratio of $\delta_i/\delta = 0.8$. The mean velocity profiles shown in Figure 24 are repeated in Figure 34 with the boundary layer thickness, δ, and the internal layer thickness, δ_i, shown on the plot. There is good agreement between the point where the rough-wall and rough-to-smooth wall profiles meet, and the location of the inner layer edge found using Antonia and Luxton's method for the first few profiles. For the latter profiles the agreement is not as good. This is due, partially, to difficulty in determining the location of the "kink" using Antonia and Luxton's method on these latter velocity profiles.

In addition to the mean velocity profiles, local skin friction coefficients were determined along the smooth-wall portion of the test surface using Preston tube measurements. Figure 35 shows the skin friction coefficient distribution for the rough-to-smooth surface at a freestream velocity of 12 m/s. Also shown on the plot are the all-rough data from Hosni (1989) and the all-smooth wall data from Brown (1988). Brown's data were taken with the same Preston tube. Hosni's rough-wall data have an uncertainty of ± 10 percent. The values of C_f determined from the Preston tube method have an uncertainty of ± 6 percent except for the value at the first smooth plate, as discussed in Chapter II. As with the Stanton number, the values of C_f fall below the smooth-wall values immediately after the rough-to-smooth interface and then rise back to the smooth-wall values. Antonia and Luxton (1972) and Andreopoulous and Wood (1982) reported a similar trend in their experiments. The skin friction coefficient data shown in Figure 35 are tabulated and shown in Appendix

B. Data at 58 m/s give similar results and are also tabulated in Appendix B.

The mean velocity profiles are plotted in the inner variable coordinates, u^+ versus y^+, for the freestream velocity of 12 m/s in Figure 36. Also shown is the reference "law of the wall" for smooth surfaces [Kays and Crawford (1980)].

$$u^+ = 2.44 \ln y^+ + 5.0 \tag{7}$$

In these coordinates, the mean velocity profiles show how quickly the flow assumes the smooth wall profiles. The profile at the x = 0.95 m location displays a slight nonlinearity in the log region. The later profiles, however, show an excellent agreement with the smooth wall log region. In contrast to the thermal boundary layer profiles shown in Figure 13, the near wall velocity profiles almost immediately fall on the smooth-wall line. Recall that the temperature profile 0.04 m downstream of the interface almost matched the rough-wall profile. Since the profiles downstream of the rough-to-smooth interface rapidly match the smooth wall log law, using the Preston tube method with Patel's calibration to determine the skin friction coefficient was assumed valid as discussed in Chapter II.

Alignment Comparison

Figure 37 compares the mean velocity profiles for the base-aligned and crest-aligned cases for a freestream velocity of 12 m/s. Both profiles were measured at a location 0.05 m downstream of the rough-to-smooth interface. As seen in this plot, there is virtually no difference between the two velocity profiles. There is a slight difference between the data for the two cases, but this difference is well within the data uncertainty. For the axial turbulence intensity profiles shown in Figure 38, the data are virtually indistinguishable between the two alignment cases. A similar comparison for skin friction coefficient, C_f, is shown in Figures 39 and 40 for freestream velocities of 12 and 58 m/s, respectively. The crest-aligned values of C_f appear to be slightly less than the corresponding base-aligned data. However, since the skin friction coefficient data have an uncertainty of ±6 percent, no real difference in the value of C_f for the two alignments can be concluded. For the above comparisons, any differences in the flow field due to alignment effects are not substantial.

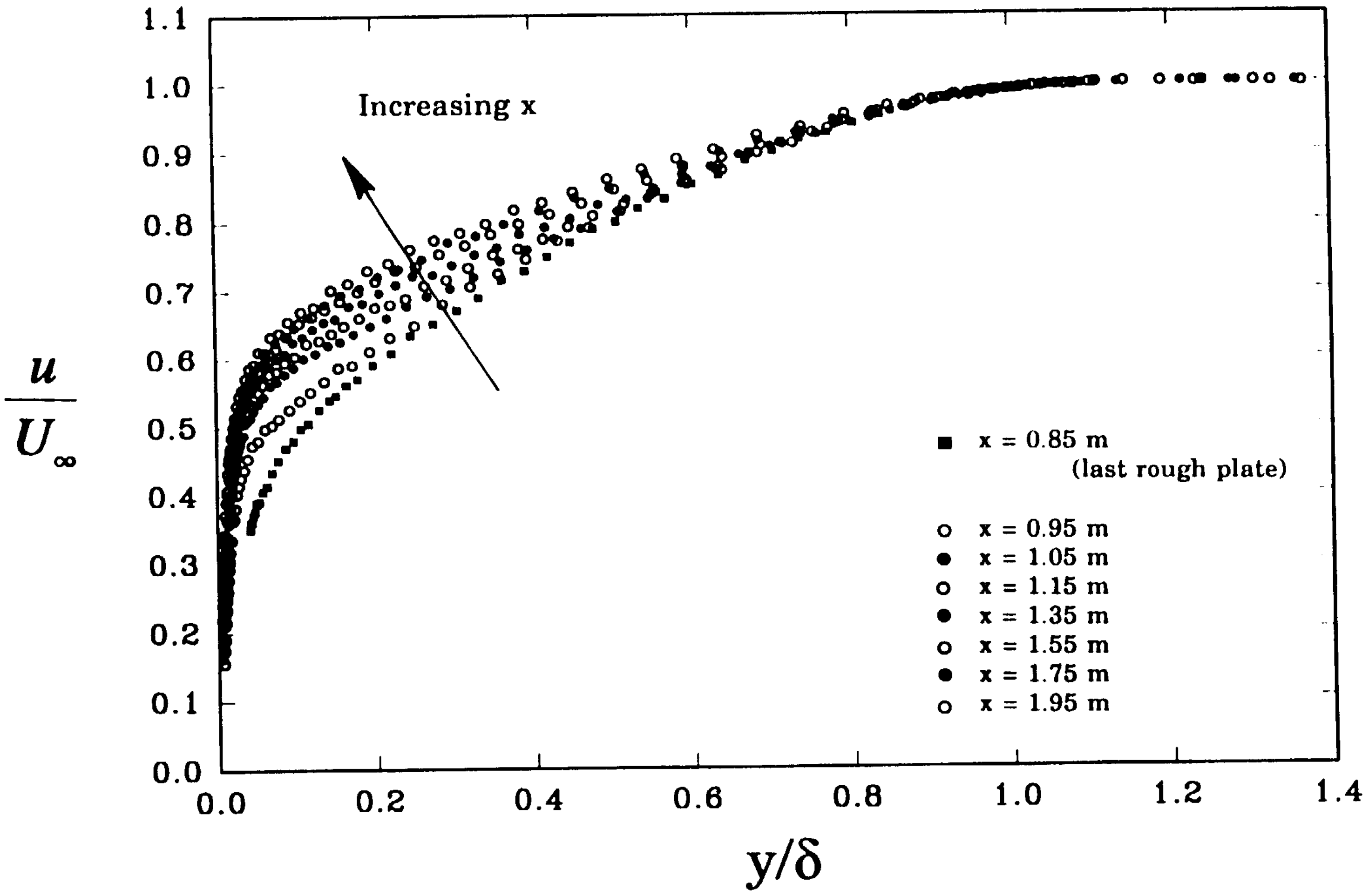

Figure 24. Velocity profiles for the rough-to-smooth surface at increasing x-locations for $U_\infty = 12$ m/s.

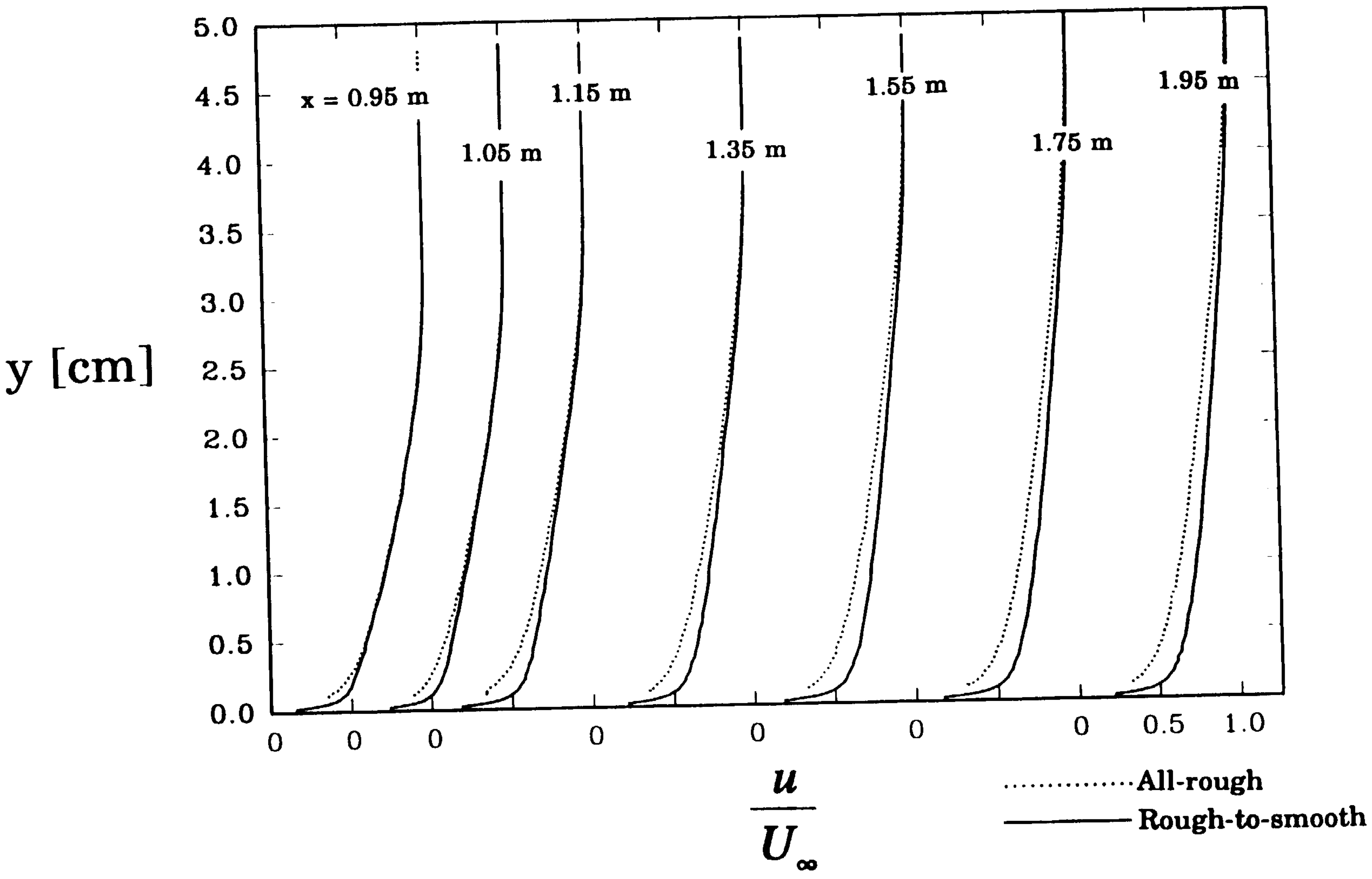

Figure 25. Velocity profiles for the rough-to-smooth and all-rough test surfaces at increasing locations plotted on a shifted axis for U_∞ = 12 m/s.

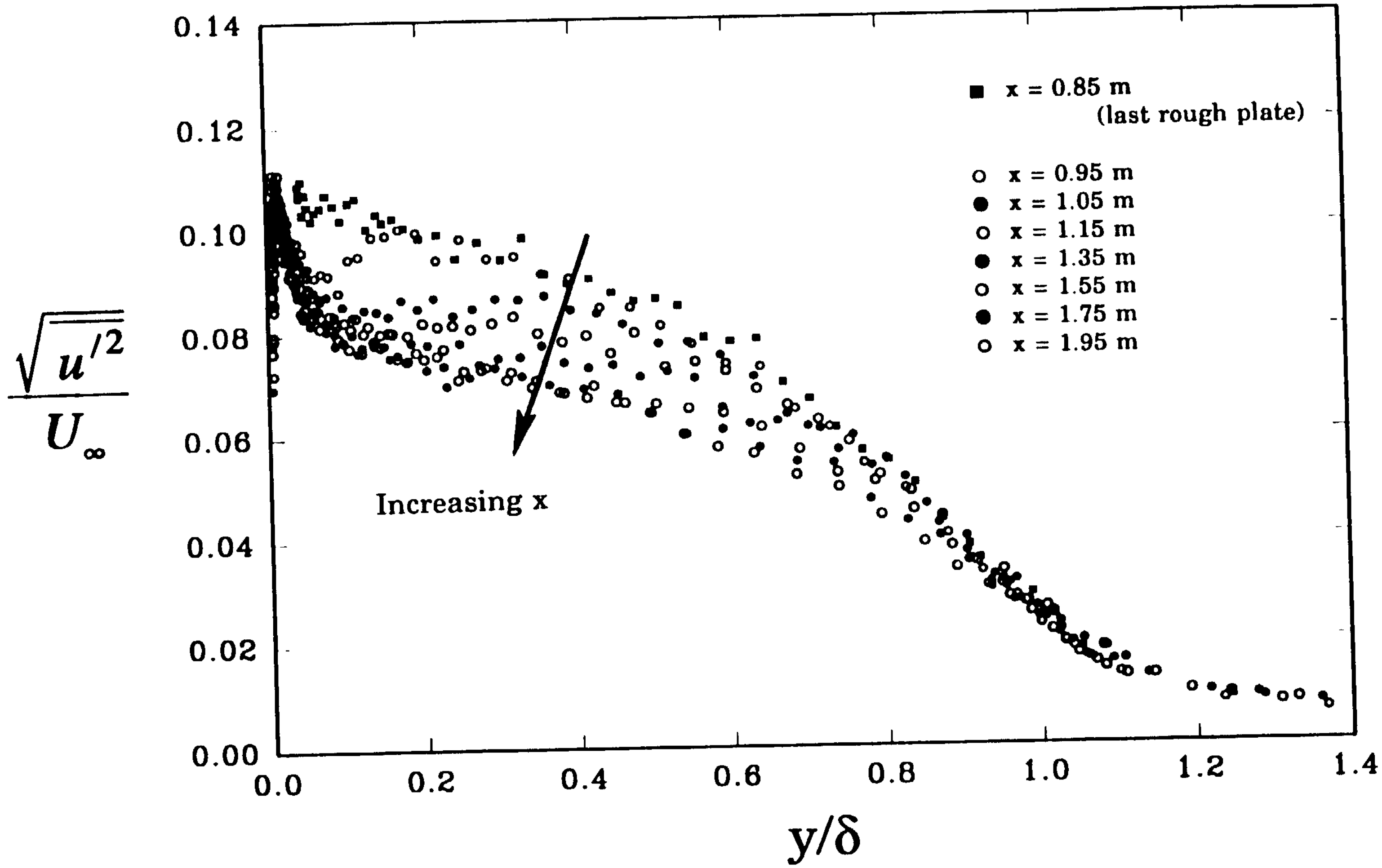

Figure 26. Axial turbulence intensity profiles for the rough-to-smooth test surface at increasing x-locations for U_∞ = 12 m/s.

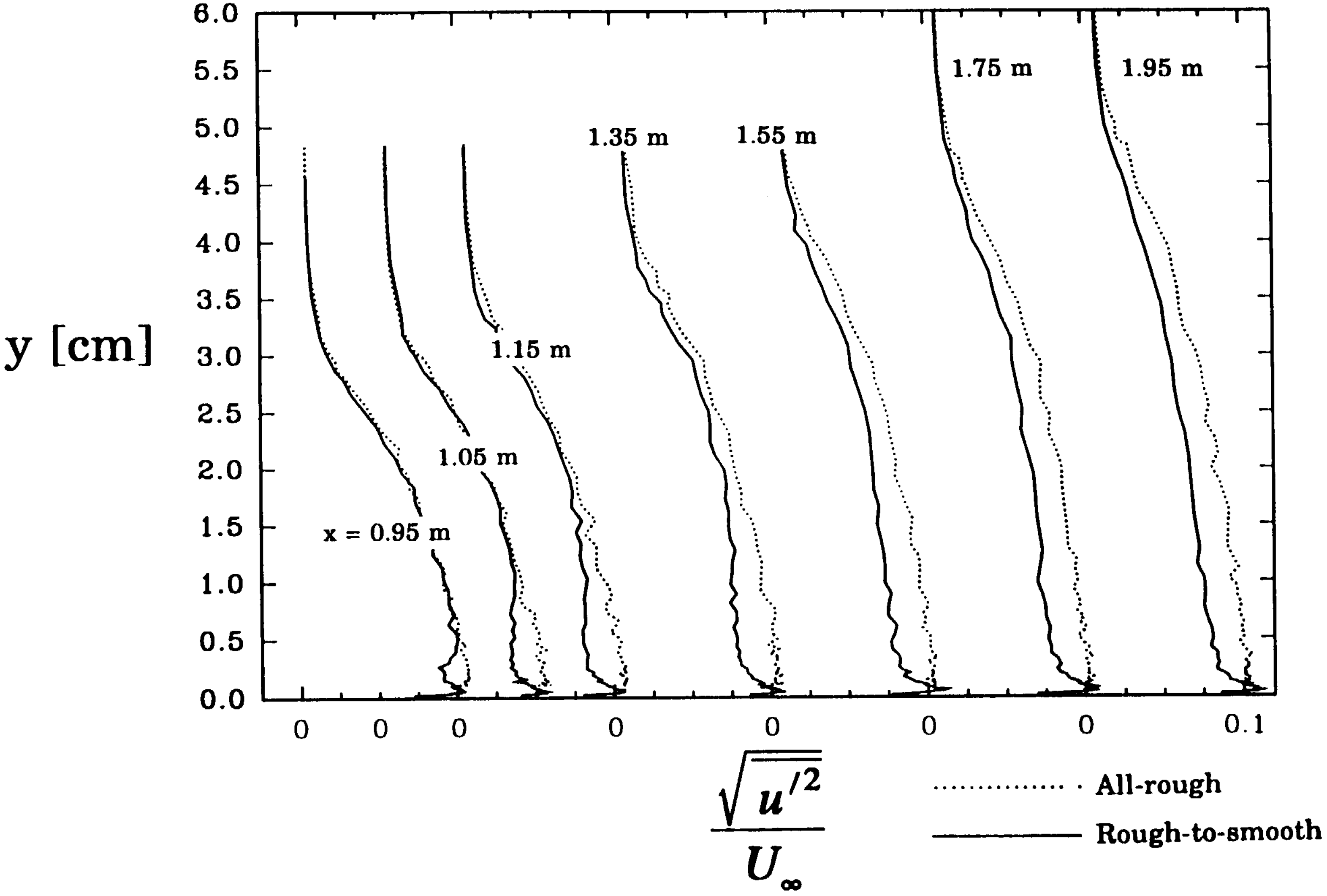

Figure 27. Axial turbulence intensity profiles for the rough-to-smooth and all-rough test surfaces at increasing x-locations plotted on a shifted axis for U_∞ = 12 m/s.

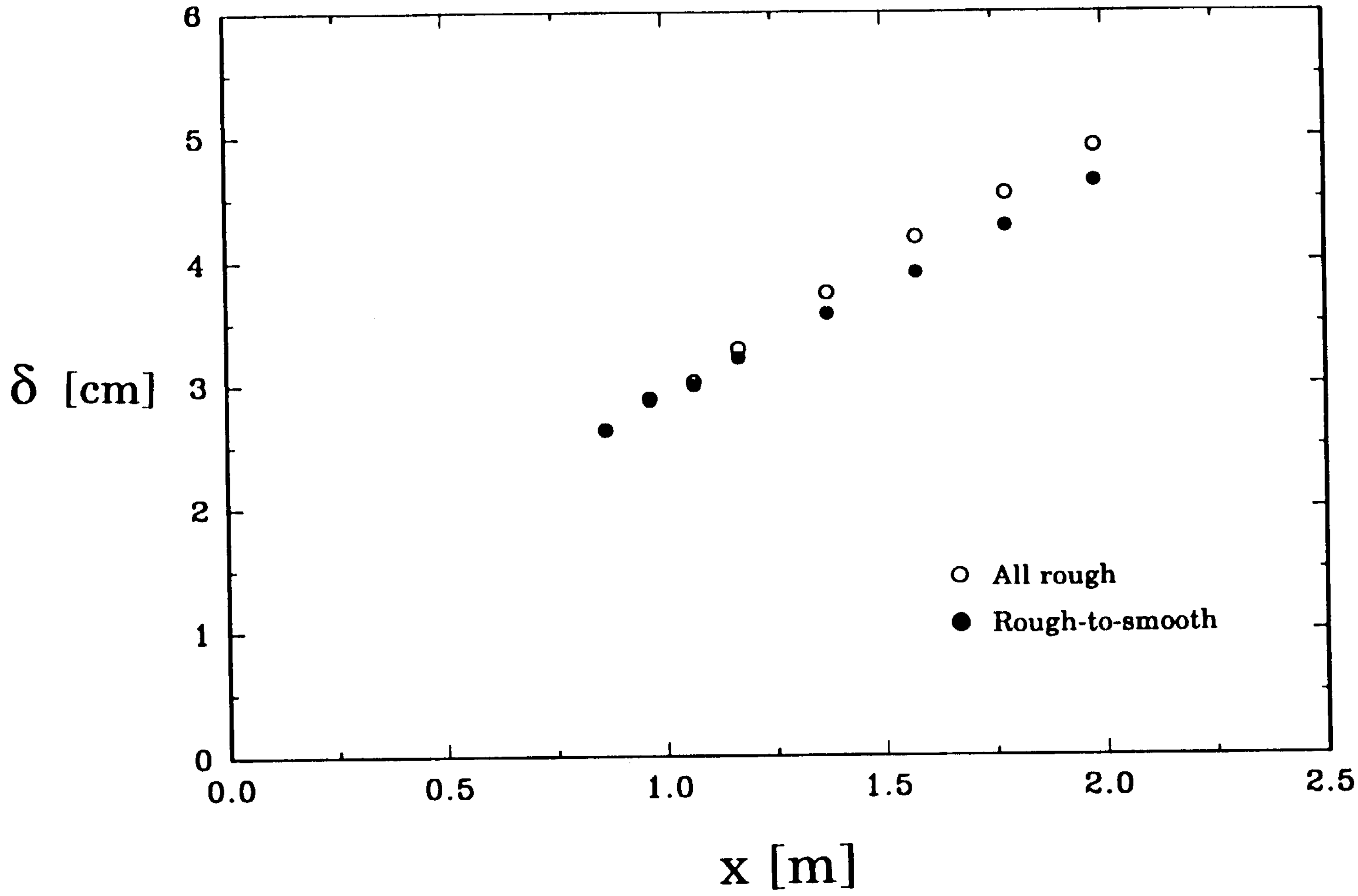

Figure 28. Comparison of boundary layer thickness versus x for the rough-to-smooth surface and all-rough surface for $U_\infty = 12$ m/s.

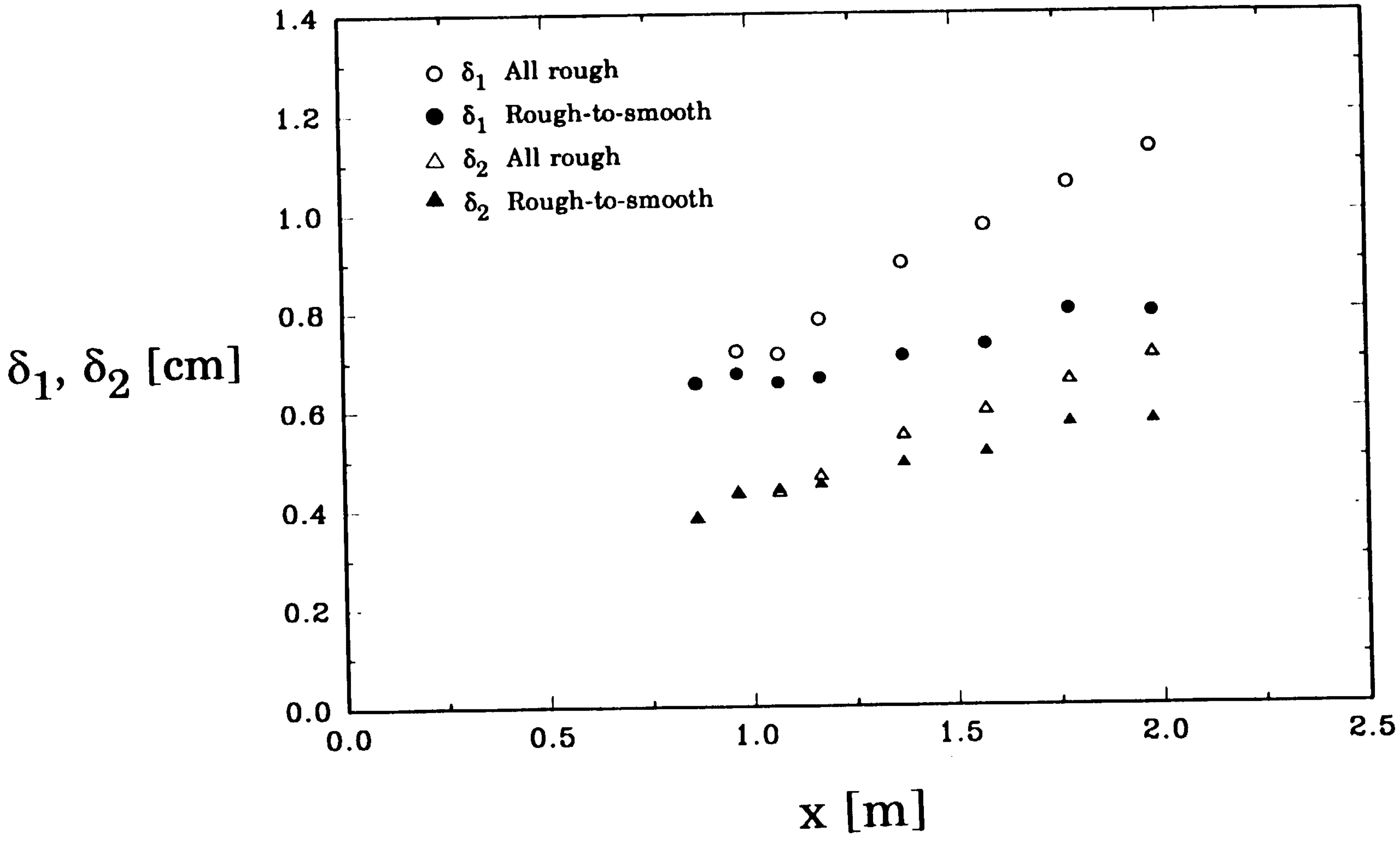

Figure 29. Comparison of displacement and momentum thickness versus **x** for the rough-to-smooth surface and all-rough surface for U_∞ = 12 m/s.

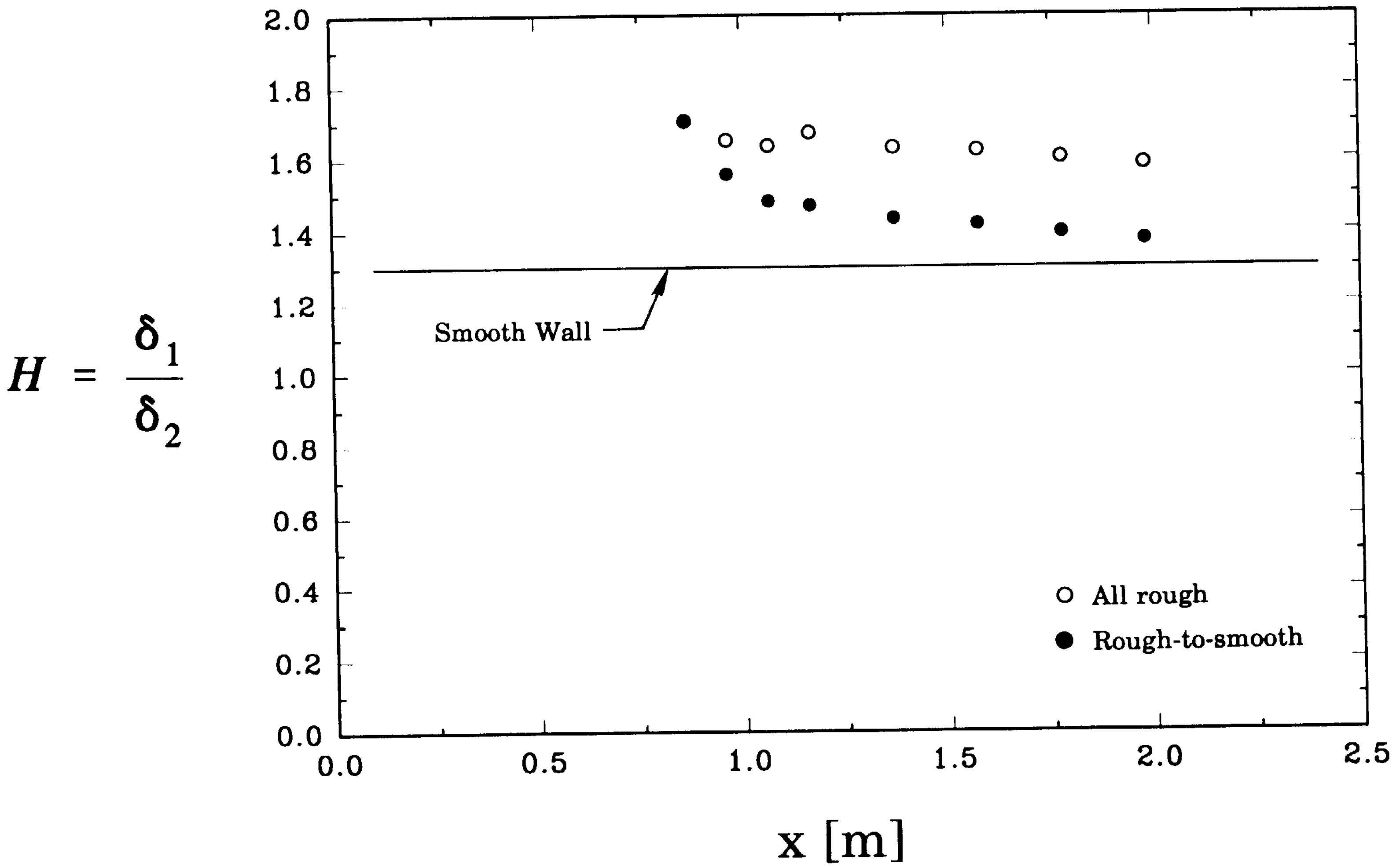

Figure 30. Comparison of shape factor versus x for the rough-to-smooth surface and the all-rough surface for U_∞ = 12 m/s.

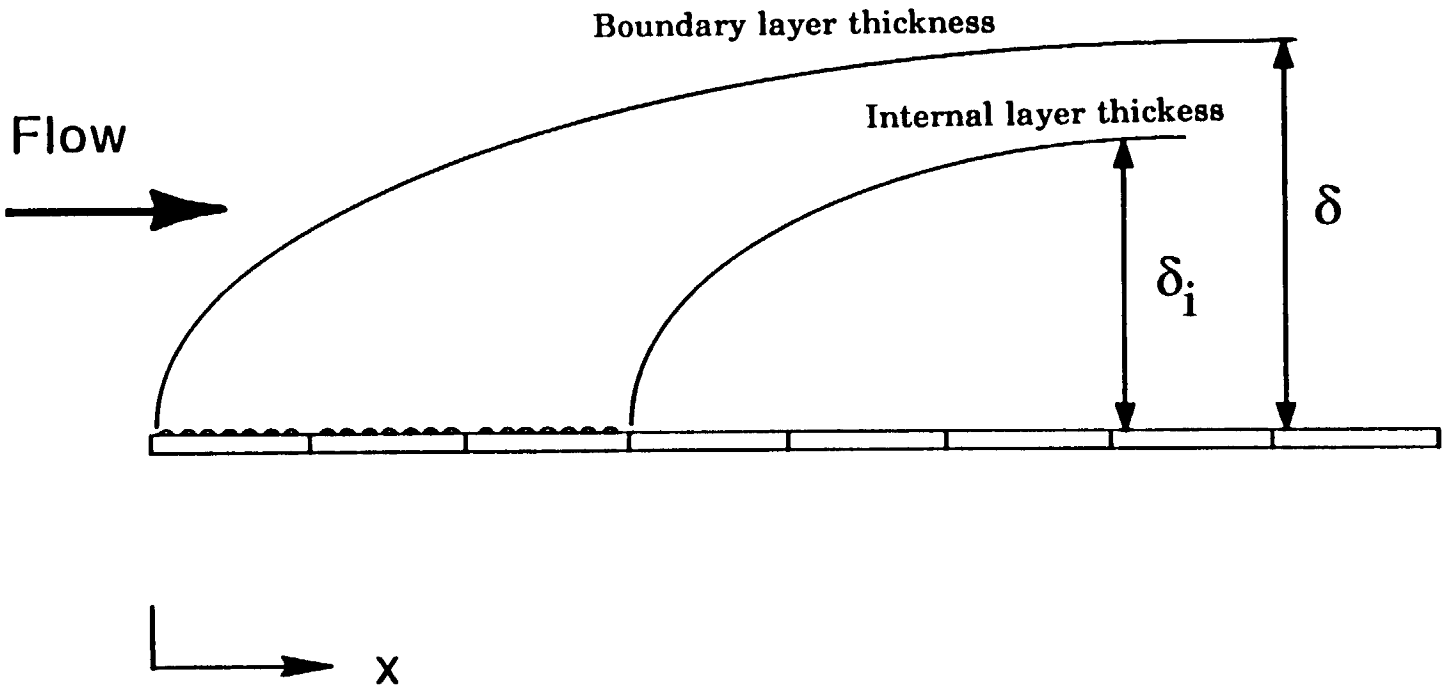

Figure 31. Internal layer and boundary layer regions of flow downstream of a step change in surface roughness.

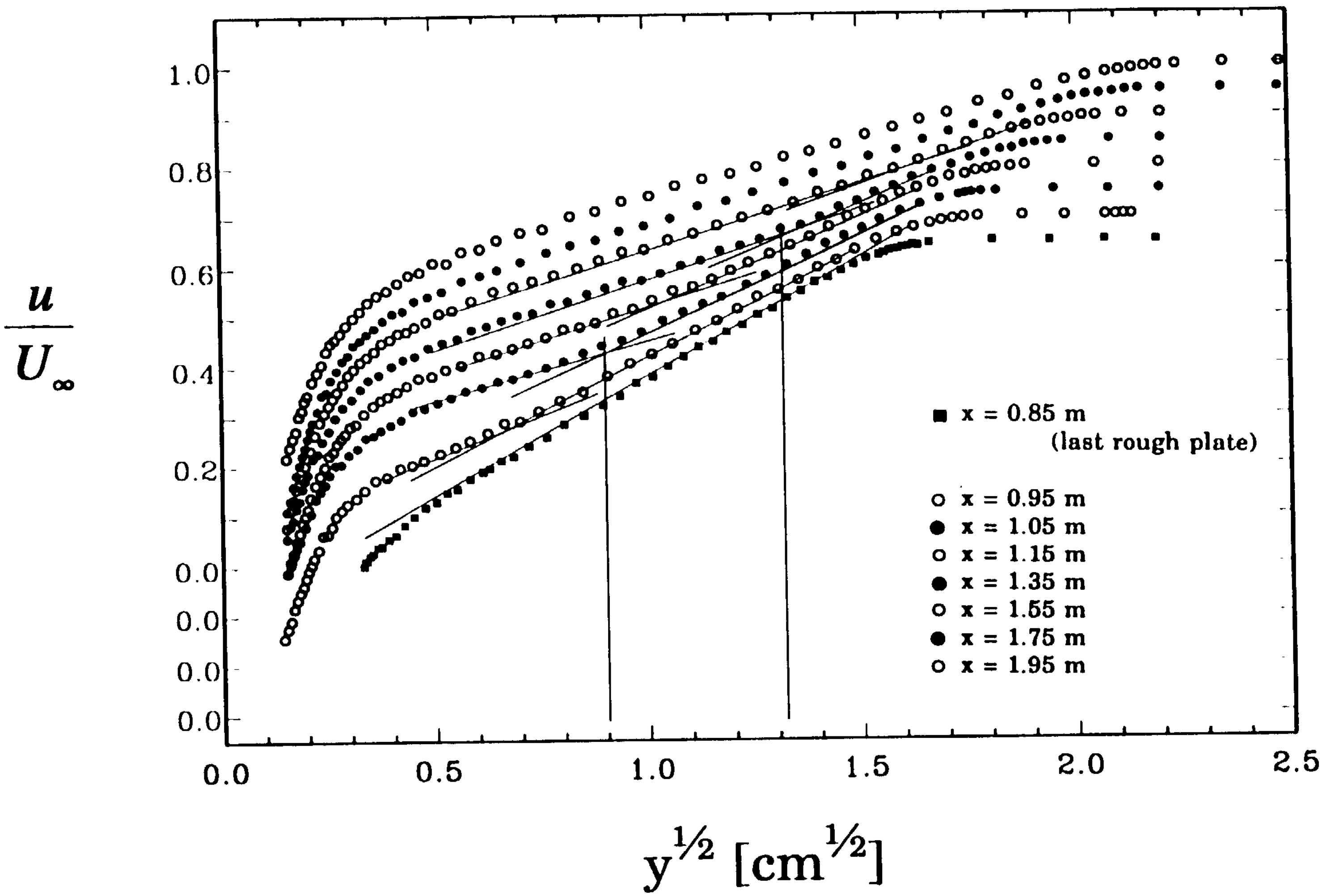

Figure 32. Mean velocity profiles plotted in u/U_∞ versus $y^{1/2}$ coordinates for U_∞ = 12 m/s.

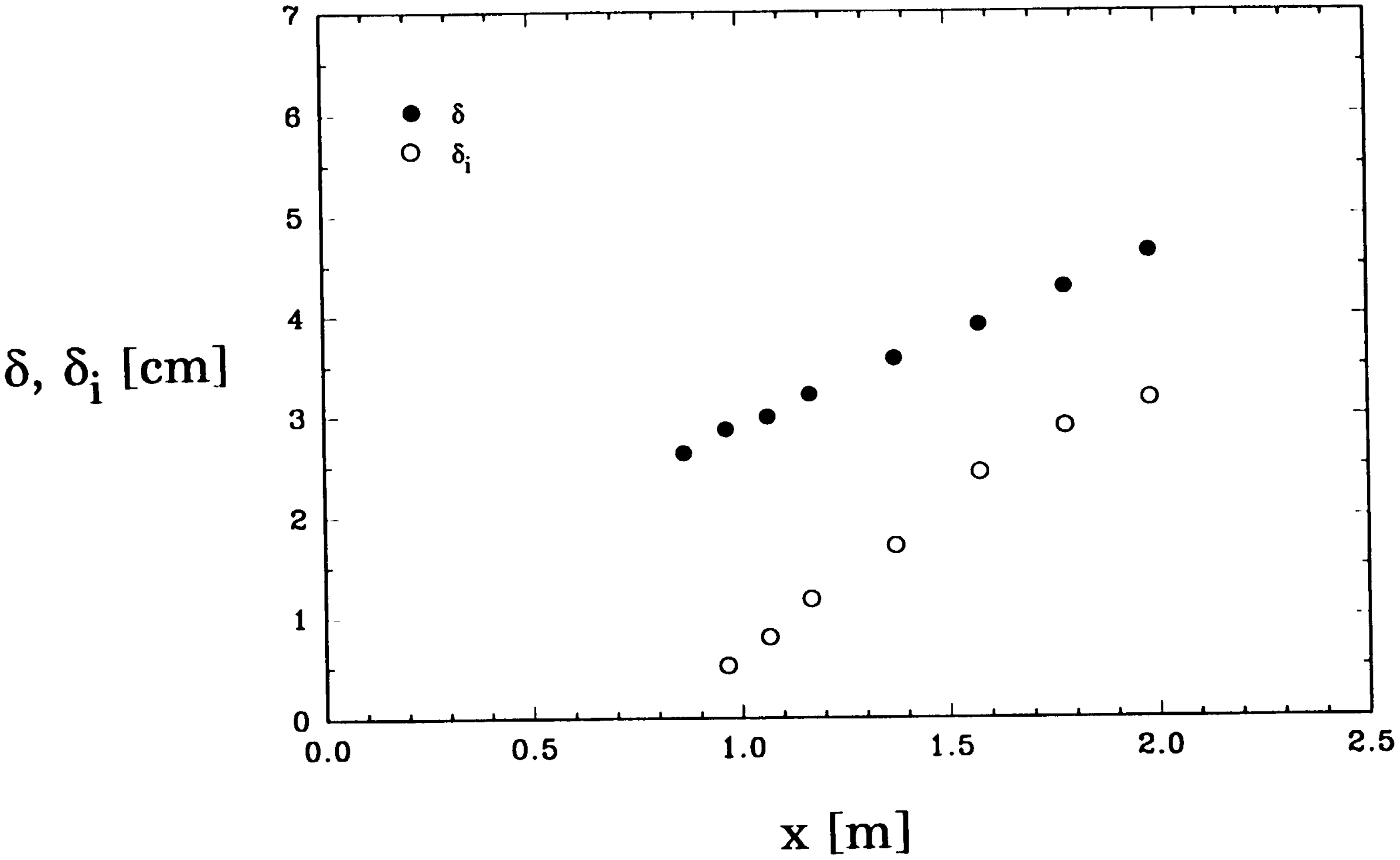

Figure 33. Boundary layer and internal layer thicknesses versus x for $U_\infty = 12$ m/s.

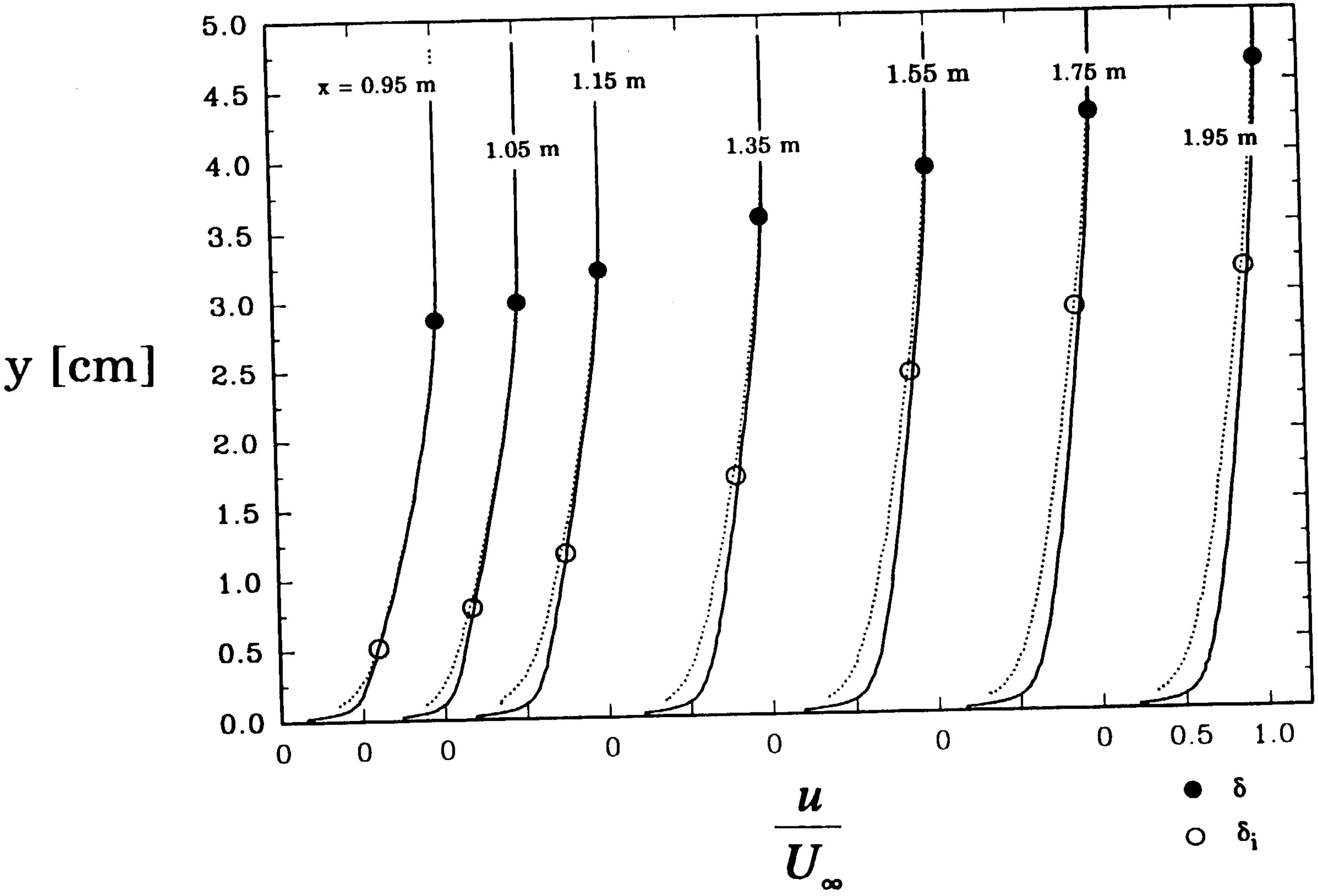

Figure 34. Boundary layer and internal layer thicknesses plotted on the composite plot of y versus u/U_∞ for the rough-to-smooth and all-rough surfaces for $U_\infty = 12$ m/s.

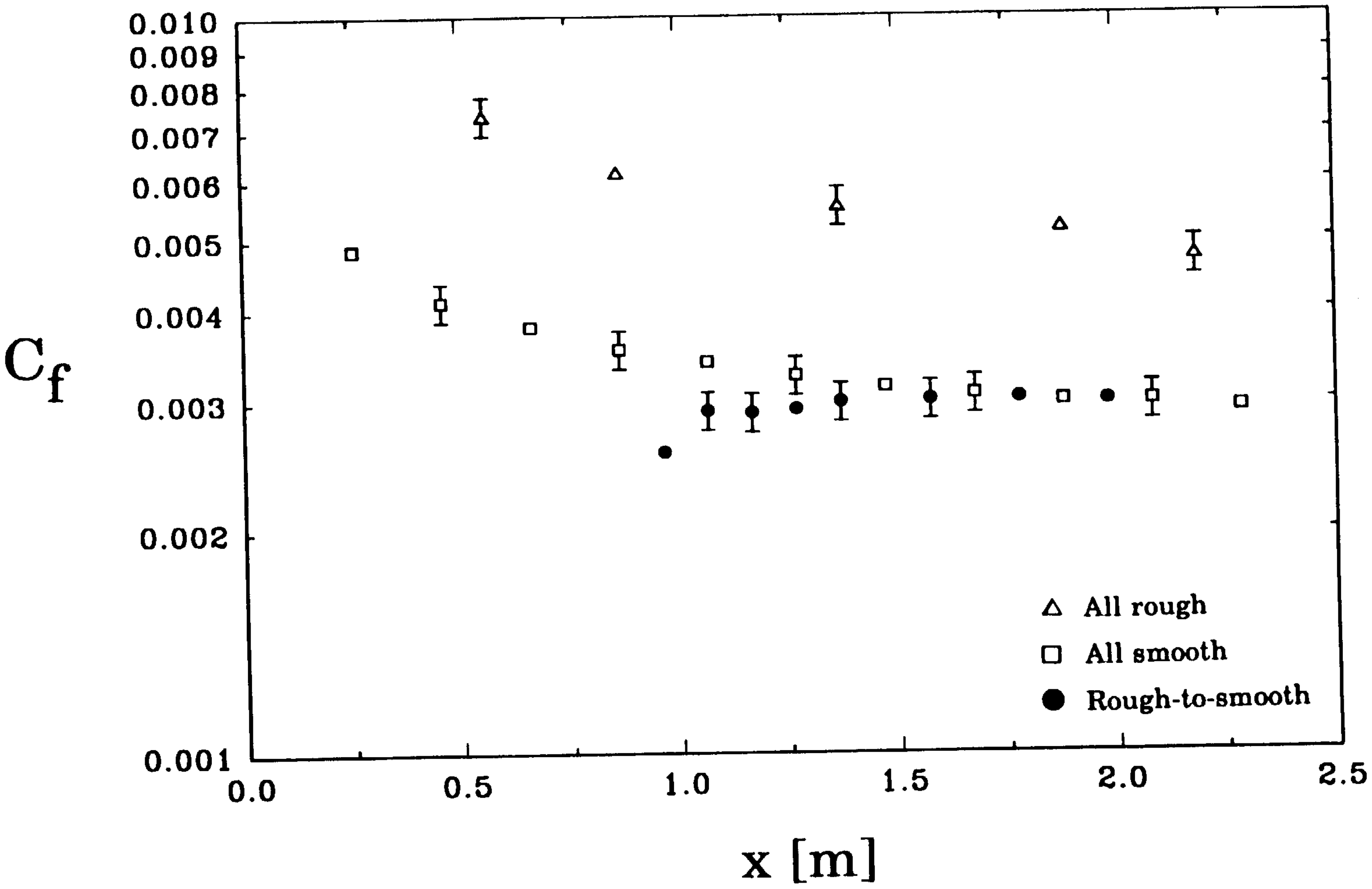

Figure 35. Comparison of skin friction coefficient versus x for the rough-to-smooth, all-rough, and all-smooth surfaces for $U_\infty = 12$ m/s.

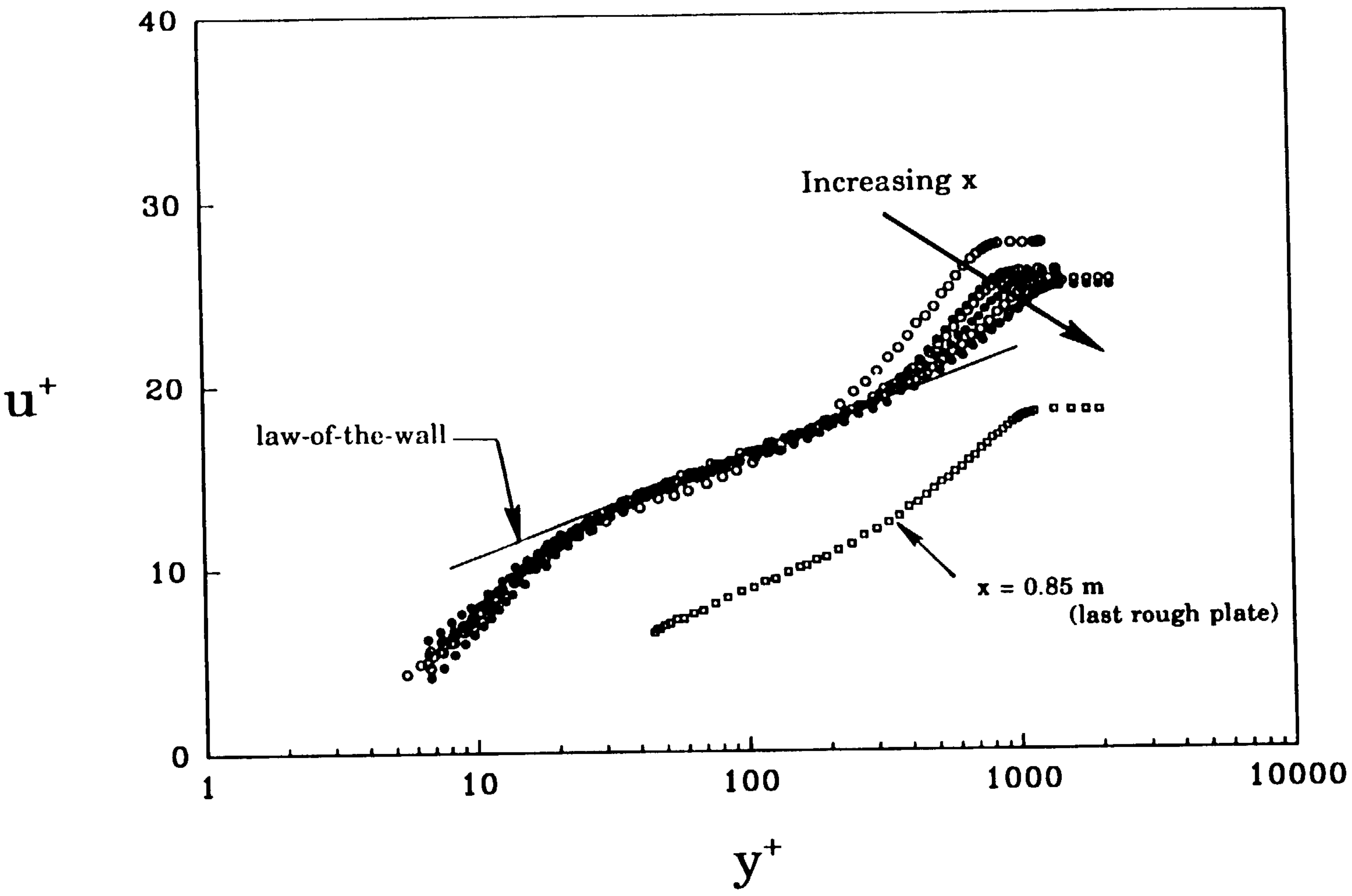

Figure 36. Mean velocity profiles for the rough-to-smooth surfaces compared with the smooth wall law of the wall for U_∞ = 12 m/s.

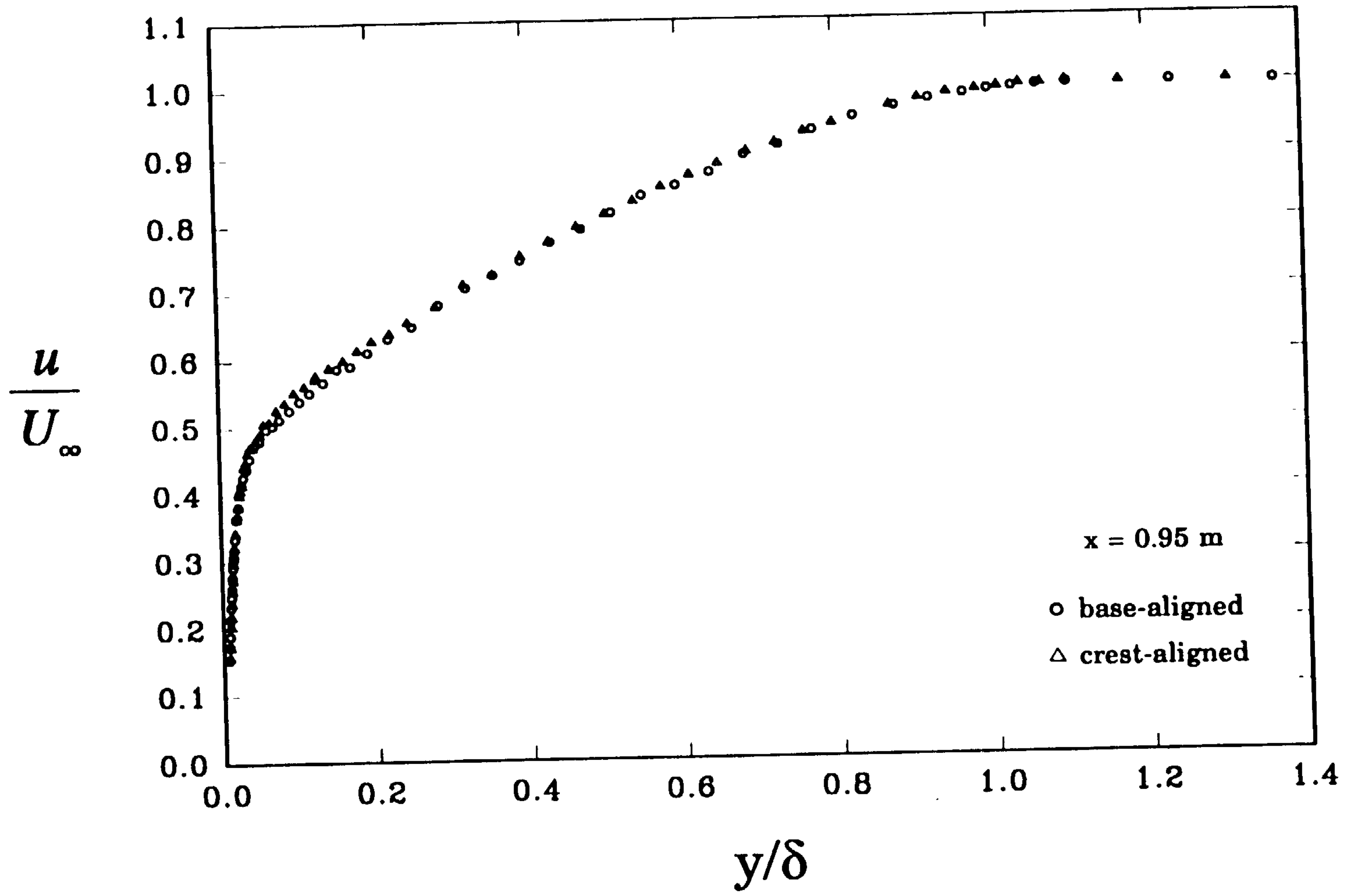

Figure 37. Comparison of mean velocity profiles for the base-aligned and crest-aligned cases for U_∞ = 12 m/s in u/U_∞ versus y/δ coordinates.

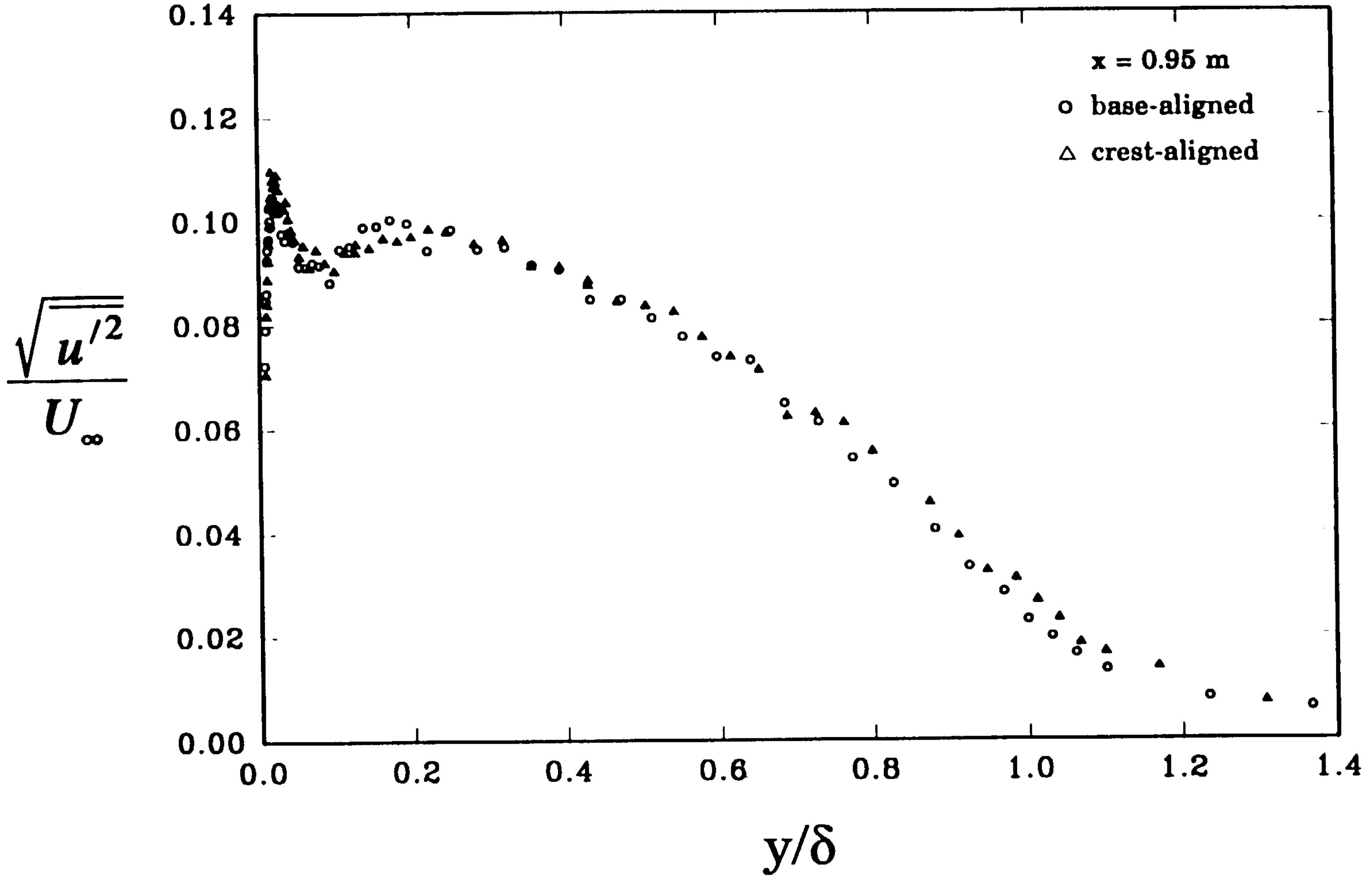

Figure 38. Comparison of the axial turbulence intensity profiles for the base-aligned and crest-aligned cases for U_∞ = 12 m/s.

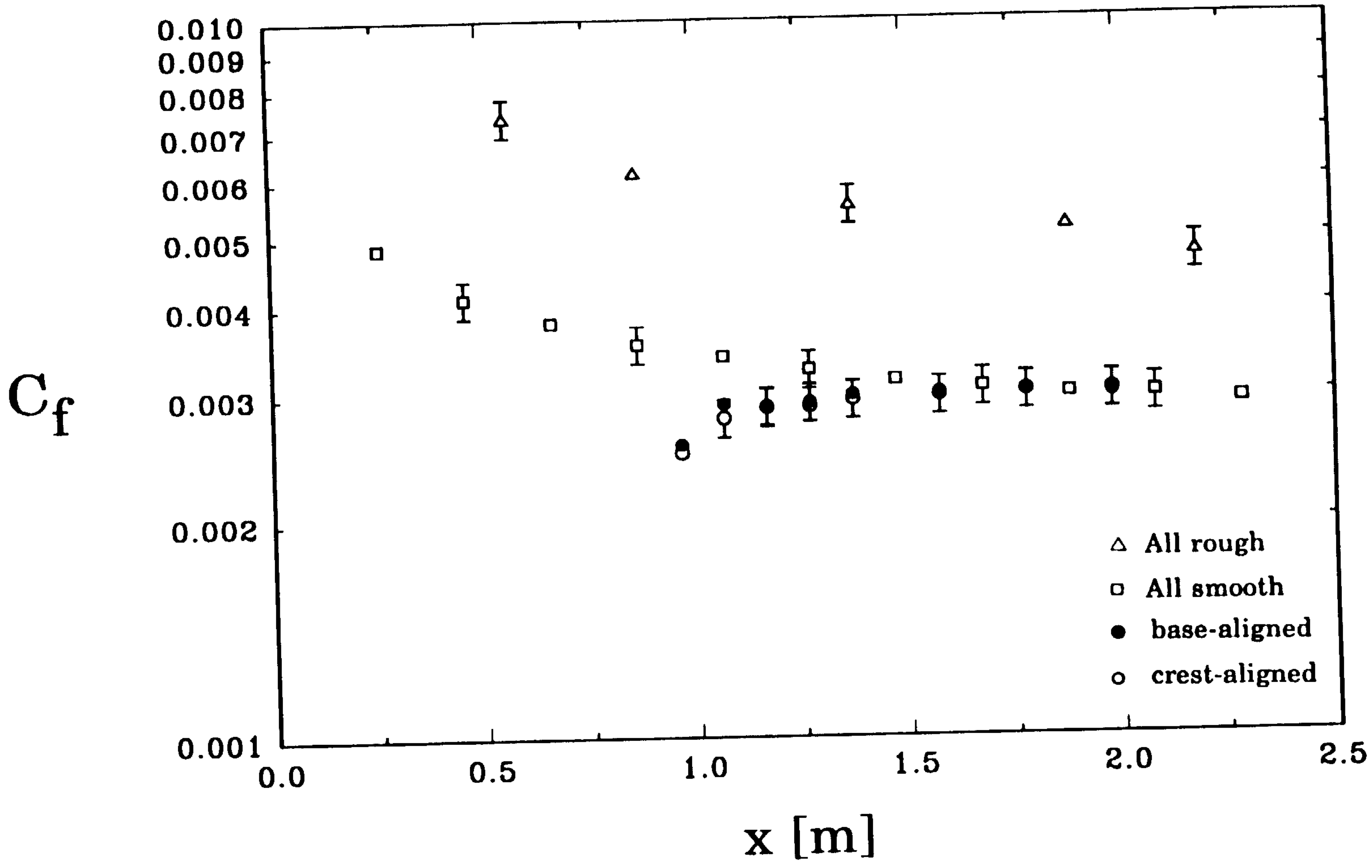

Figure 39. Comparison of skin friction coefficient versus x for the base-aligned and crest-aligned cases for $U_\infty = 12$ m/s.

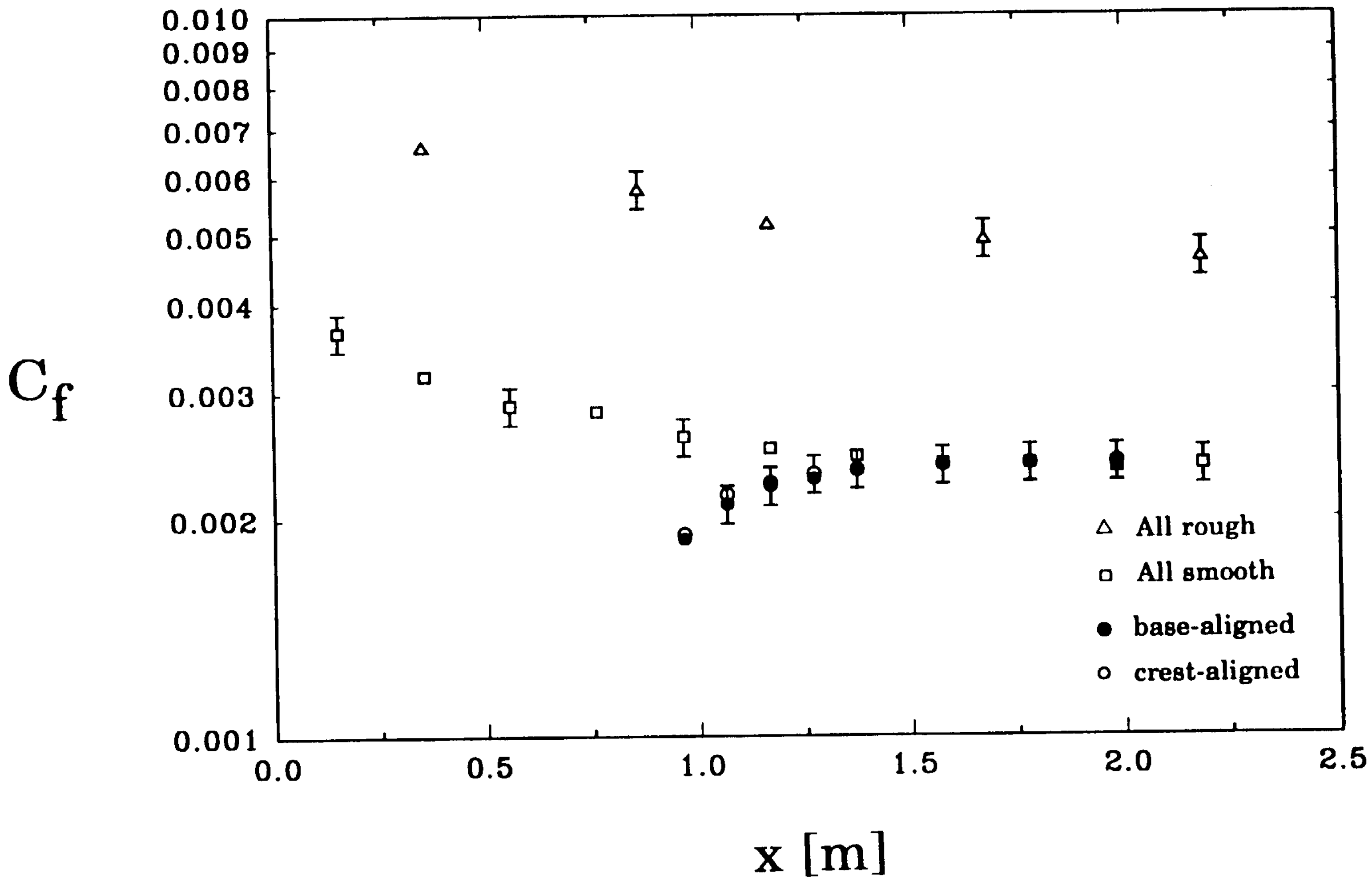

Figure 40. Comparison of skin friction coefficient versus x for the base-aligned and crest-aligned cases for $U_\infty = 58$ m/s.

CHAPTER V

COMPARISON OF DATA AND PREDICTIONS

The development of the turbulent boundary layer over a surface with a step change in surface roughness can be predicted with good accuracy using standard roughness and turbulence models. In this chapter, the discrete element method is described, and computations using this method are compared with selected data sets from the preceding chapters.

Discrete Element Method

The two basic categories in which calculation efforts have fallen are (1) the equivalent sandgrain approach and (2) the discrete element approach. While both methods require experimental input, the equivalent sandgrain approach may require experimental data on the particular surface under consideration. On the other hand, the discrete element approach incorporates more basic physics of the process and uses a more generalized empirical input. It is therefore applicable to a broader spectrum of rough surfaces without requiring surface-specific experimental data. Since the discrete element approach is used for computations reported in this report, an overview of this method is presented next.

The discrete element approach considers the mass, momentum and energy transport processes on the collection of individual roughness elements and the smooth surface between the elements. The basic idea is to formulate a system of partial differential equations that describes the mass, momentum and energy transport for the flow over, around and between the roughness elements. In this method, the roughness effects are taken as an integral part of the flow problem and not (as with the equivalent sandgrain approach) as some ill-defined boundary condition.

The discrete element method used in this work is formulated for roughness elements with three dimensional shapes (as opposed to transverse ribs) for which the element cross section can be approximated as circular at every height, y. Thus, the geometric description of the roughness element, d(y), is easily included in this prediction scheme.

The steady (Reynolds-averaged), two-dimensional turbulent boundary layer equations presented here are for flow over a rough surface with roughness elements of uniform shape and spacing as derived by Taylor et al. (1984, 1985). The equations are:

$$\frac{\partial}{\partial x}(\rho \beta_x u) + \frac{\partial}{\partial y}(\rho \beta_y v) = 0 \tag{8}$$

$$\beta_x \rho u \frac{\partial u}{\partial x} + \beta_y \rho v \frac{\partial u}{\partial y} = - \frac{\partial}{\partial x}(\beta_x P) + \frac{\partial}{\partial y}\left[\beta_y \left(\mu \frac{\partial u}{\partial y} - \rho \overline{u'v'}\right)\right] - \frac{1}{2}\rho C_D d(y) \frac{u^2}{L^2} \tag{9}$$

$$\begin{aligned} \beta_x \rho u \frac{\partial H}{\partial x} + \beta_y \rho v \frac{\partial H}{\partial y} = {} & \frac{\partial}{\partial y}\left[\beta_y \left(\frac{K}{C_p}\frac{\partial H}{\partial y} - \rho \overline{v'h'}\right)\right] \\ & + u \frac{\partial}{\partial x}(\beta_x P) + \beta_y \frac{\partial u}{\partial y}\left(\mu \frac{\partial u}{\partial y} - \rho \overline{u'v'}\right) \\ & + \frac{1}{2}\rho C_D \frac{d(y)}{L^2} u^3 + \pi \frac{K Nu_d}{L^2}(T_R - T) \end{aligned} \tag{10}$$

Empirical models for $-\rho\overline{u'v'}, -\rho\overline{v'h'}$, the roughness element drag coefficient $C_D(y)$, and the roughness element Nusselt number $Nu_d(y)$ are necessary for closure.

The blockage parameters β_x and β_y and the element shape descriptor d(y) require no empirical fluid mechanics input as they are determined solely from the geometry of the rough surface. Taylor et al. (1984) have shown for uniform three-dimensional roughness elements with circular cross-section that

$$\beta_x = \beta_y = 1 - \frac{\pi d^2(y)}{4L^2} \tag{11}$$

where for y > k, d(y) = 0 and both β_x and β_y become identically 1.0.

The boundary conditions for the discrete element approach for rough wall flows are identical to those for smooth wall flows. The wall location (y = 0) is the smooth surface on which the roughness elements occur. At y = 0, u = v = 0 and $H = H_w$. As $y \to \infty$, $u \to U_\infty$ and $H \to H_\infty$.

The numerical solution of the discrete element equations is obtained by finite difference solution of the transformed equations in the computational plane. The transformation, finite difference scheme, and program structure are described by Taylor et al. (1984). The steamwise derivative is approximated with a first-order backwards difference. The surface normal derivatives are replaced with second-order approximations which allow the spacing between grid points to vary with distance from the wall. This allows a concentration of nodes near the wall and below the crests of the elements. In this stretched grid the ratio of any two adjacent mesh lengths is a constant.

The solution is by an iterative marching, implicit method. The solution is known at station i and is sought at station i + 1. The implicit difference equations result in a tridiagonal coefficient matrix whose inverse is known and can be expressed algebraically (often referred to as the Thomas algorithm). Since the equations are non-linear, the system must be solved by iteration. A relaxation scheme is employed with a required residual < 0.01 percent.

The solutions were obtained on finer and finer grids until differences were less than 1 percent in computed values of C_f and St. In the transformed coordinates there were typically 120 grid points across the boundary layer with approximately 20-30 grid points below the crests of the elements. The streamwise grid spacing was typically 1 cm.

In addition, the codes were verified by comparisons with known solutions of smooth-wall laminar and turbulent flows.

The "wall shear stress" is defined as the sum of the shear and drag forces on the wall in the mean flow direction divided by the plan area of the wall. The corresponding skin friction coefficient is then

$$C_f = \frac{(\beta_y)_w \, \mu \left.\frac{\partial u}{\partial y}\right|_w + \frac{1}{2}\frac{1}{L^2}\int_0^k (\rho d C_D u^2) dy}{\frac{1}{2}\rho_\infty U_\infty^2} \tag{12}$$

and the Stanton Number is

$$St = \frac{-(\beta_y)_w \, \frac{K}{C_p}\left.\frac{\partial H}{\partial y}\right|_w + \frac{\pi}{L^2}\int_0^k [K Nu_d (T_R - T)] dy}{\rho_\infty U_\infty (H_w - H_{0,\infty})} \tag{13}$$

In order to solve Eqs. (8), (9) and (10), turbulence models for $-\overline{\rho u'v'}$ and $\overline{\rho v'h'}$ and roughness models for C_D and Nu_d are required. Because of its proven predictive capability for attached boundary layer flows over smooth surfaces, the Prandtl mixing length model with van Driest damping and a constant turbulent Prandtl number is used for turbulence closure. Thus

$$-\overline{\rho u'v'} = \rho l_m^2 \left(\frac{\partial u}{\partial y}\right)\left|\frac{\partial u}{\partial y}\right| = \mu_t \frac{\partial u}{\partial y} \tag{14}$$

where

$$\begin{aligned} l_m &= 0.40y[1 - \exp(-y^+/26)]\ ;\ l_m < 0.09\delta \\ l_m &= 0.09\delta;\ \textit{otherwise}, \end{aligned} \tag{15}$$

and

$$-\overline{\rho v'h'} = \frac{\mu_t}{Pr_t}\frac{\partial H}{\partial y} \tag{16}$$

where $Pr_t = 0.9$. Transition from laminar to turbulent flow is modeled using a streamwise intermittency factor

$$\frac{\mu_{eff}}{\mu_t} = 1 - e^{-3.61(x/x_c-1)^2} \tag{17}$$

where x_c is the specified point at which transition begins.

After the surface changes abruptly from rough to smooth, the turbulence will not immediately take on the new equilibrium values for the smooth surface. The turbulent flow "remembers" the upstream history. The mixing length model presented above does not account for this effect. Here, a fairly crude fix is adopted by using a lag model downstream of the step in roughness. This was done by taking a weighted average of the predicted local eddy viscosity, μ_{te}, with the eddy viscosity at some upstream location

$$\mu_t = \mu_{t0}(1-\eta) + \mu_{te}\eta \tag{18}$$

$$\eta = 1 - e^{-(x-x_0)/\lambda} \tag{19}$$

where $\lambda = 5\delta_o$ with δ_o being the boundary layer thickness at x_o which was located 0.02 m upstream of the interface between the surfaces. This idea was taken from a boundary layer shock wave interaction model of Shang, Hankey, and Law (1976).

The roughness element C_D and Nu_d models are formulated as functions of the local element Reynolds number $Re_d = u(y)d(y)/\nu$ which includes roughness element size and shape information through d(y). As discussed in Taylor et al. (1984), the C_D model which gave the best overall agreement with experimental data was

$$\log_{10}(C_D) = -\ 0.125\ \log_{10}(Re_d) + 0.375 \tag{20}$$

This model has been tested for values of Re_d up to

25,000 (Taylor et al. (1984), Scaggs et al. (1988)) using many data sets. In particular, Scaggs et al. used eleven different rough surfaces, nine of which had uniform roughness elements and two of which were roughened nonuniformly. It was demonstrated that the roughness element drag coefficient model in the discrete element prediction approach gave excellent agreement with all of these data sets.

Consequently, this model was used unchanged for the predictions presented in this work.

The roughness element energy transport model requires empirical input in the form of a Nusselt number, Nu_d. Hosni, et al. (1989) developed the model

$$Nu_d = 1.7\ Re_d^{0.49} Pr^{0.4} \tag{21}$$

which is used in this work. This model has been tested up to Re_d of about 2200. All of the experiments reported in this article have local element Reynolds numbers, Re_d, which fall within the ranges of calibration listed above.

Comparisons

In the following comparisons all predictions and data correspond to the base aligned cases.

Figures 41-46 show the comparisons between the data and the predictions for freestream velocities of 6, 12, 27, 43, 58, and 66 m/s. As stated before, the 6 m/s case in Figure 41 has a transitionally rough turbulent boundary layer over the rough portion of the surface. The other velocities have fully rough boundary layers over the rough portion. The discrete element method predictions are seen to be in good agreement for the 12 m/s and higher velocity cases (Figures 42-46). The rough portion Stanton number are somewhat underpredicted for the 6 m/s case, but the trends of this complicated case are reasonably predicted.

Figure 47 shows the results of the velocity profile predictions for the 12 m/s case. These are the same conditions as the data given in Figure 24. Comparison of the two figures shows that the predictions agree well with the data. Figures 48 and

49 show the comparison for skin friction coefficients with freestream velocities of 12 and 58 m/s respectively. The agreement is seen to be very good.

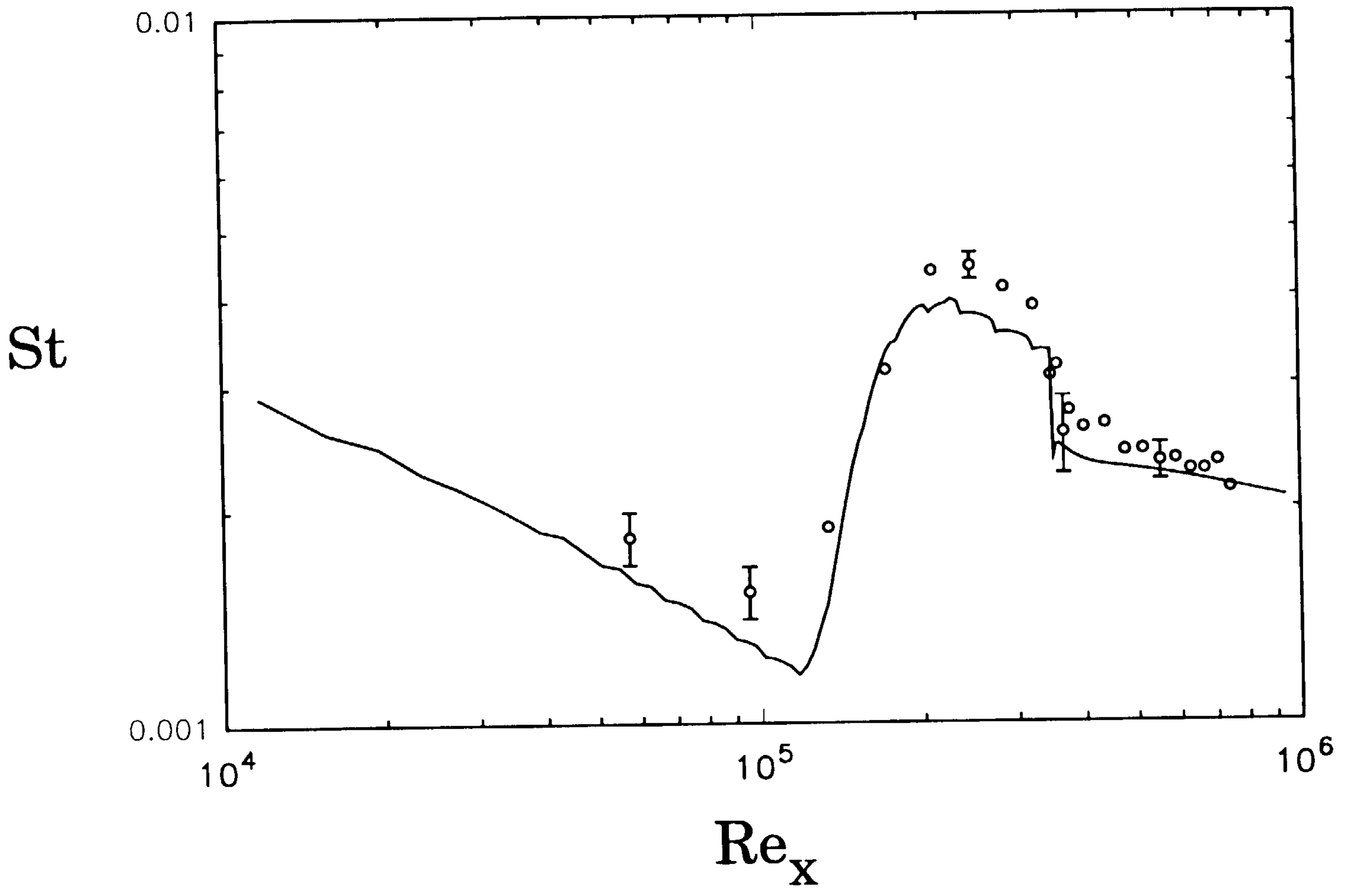

Figure 41. Comparison of base-aligned Stanton number predictions and data for U_∞ = 6 m/s.

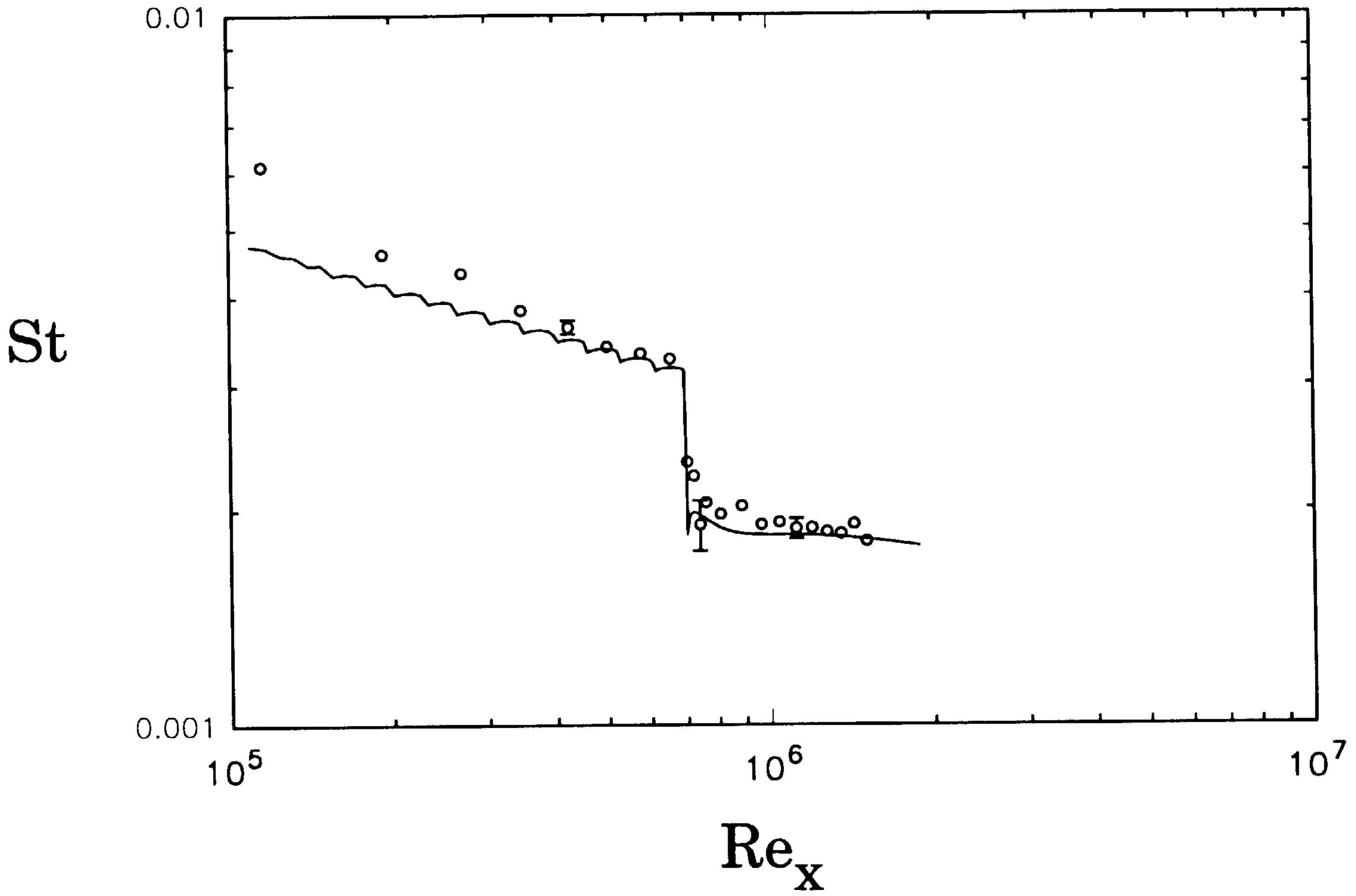

Figure 42. Comparison of base-aligned Stanton number predictions and data for U_∞ = 12 m/s.

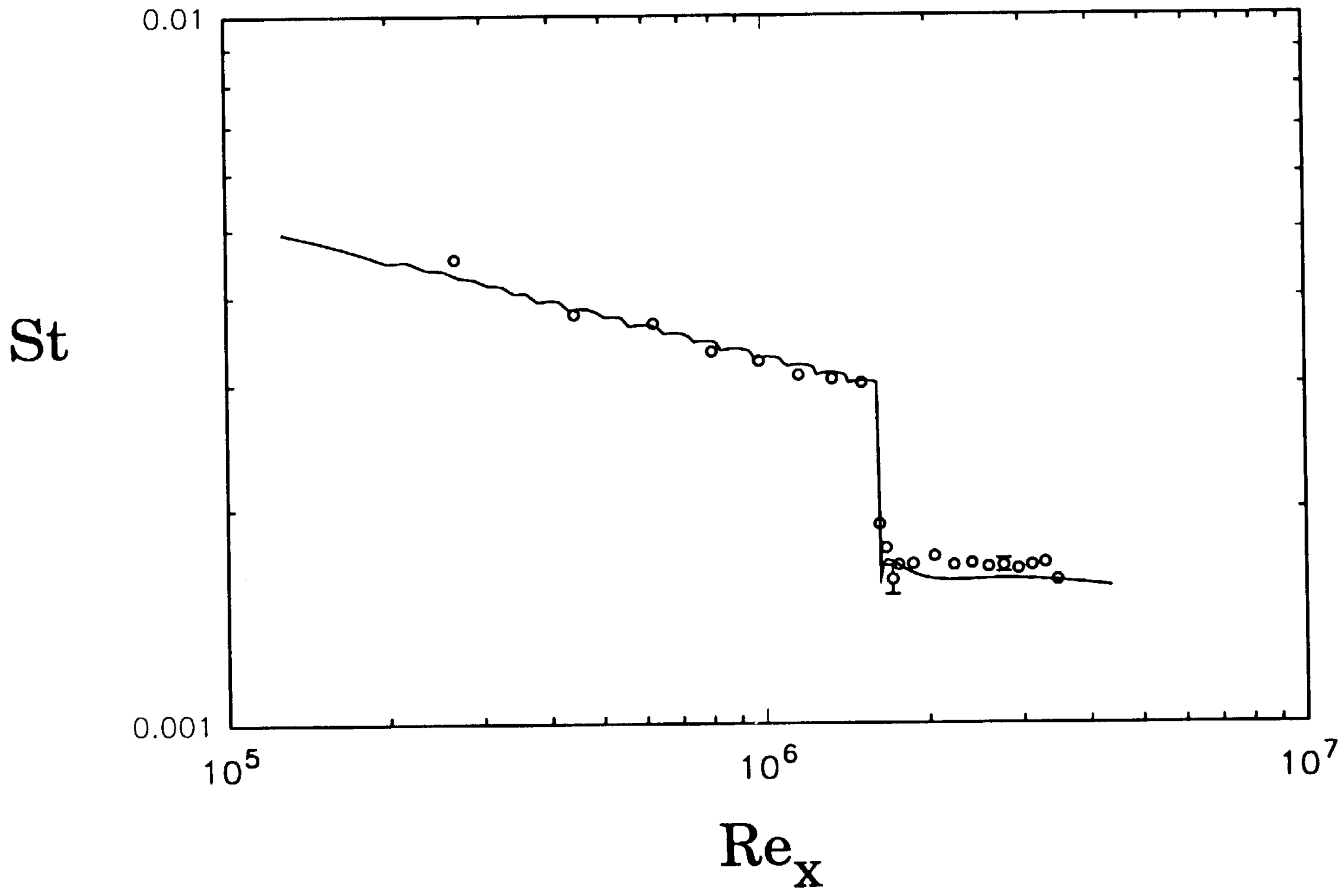

Figure 43. Comparison of base-aligned Stanton number predictions and data for $U_\infty = 27$ m/s.

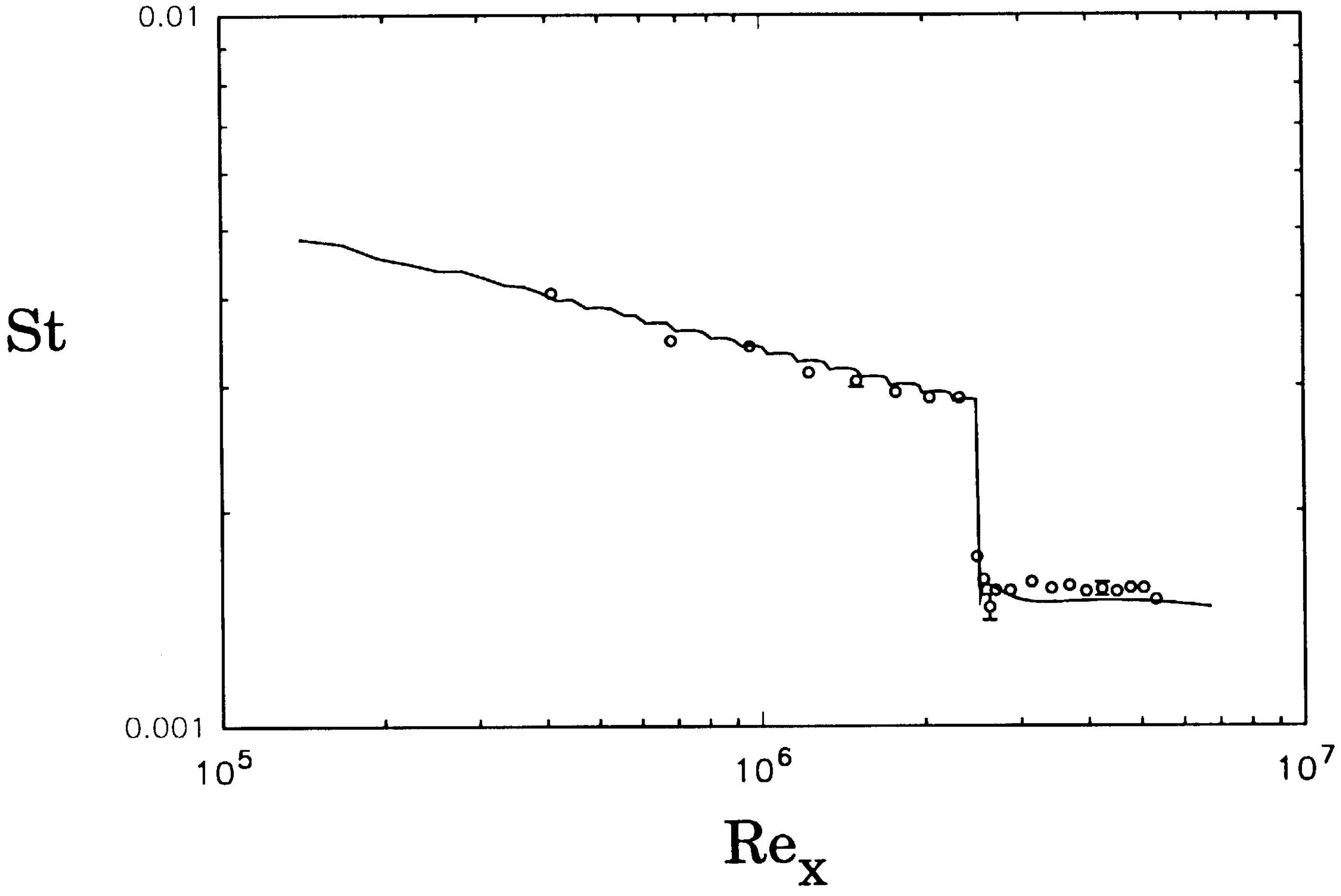

Figure 44. Comparison of base-aligned Stanton number predictions and data for $U_\infty = 43$ m/s.

C-2

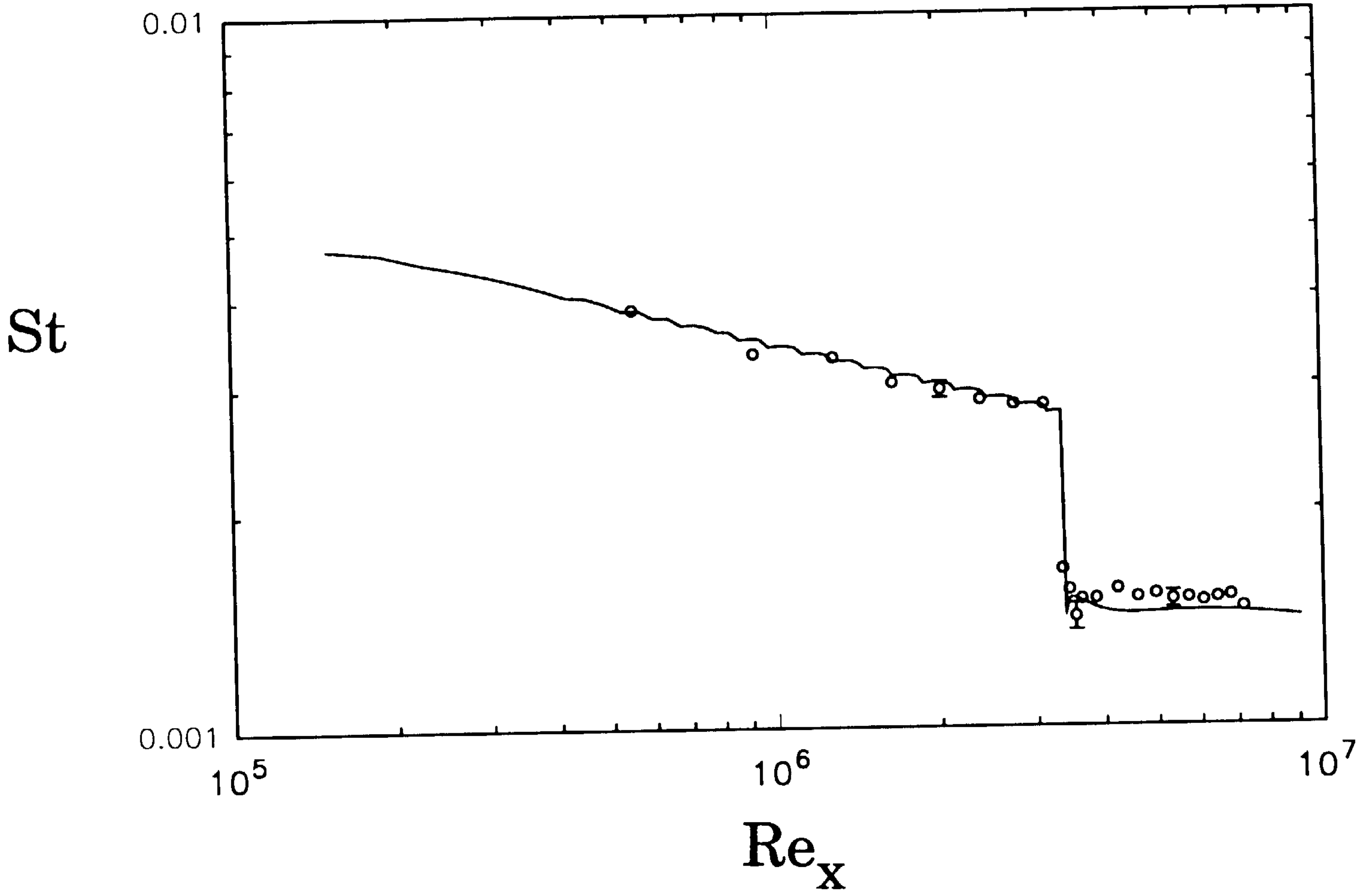

Figure 45. Comparison of base-aligned Stanton number predictions and data for $U_\infty = 58$ m/s.

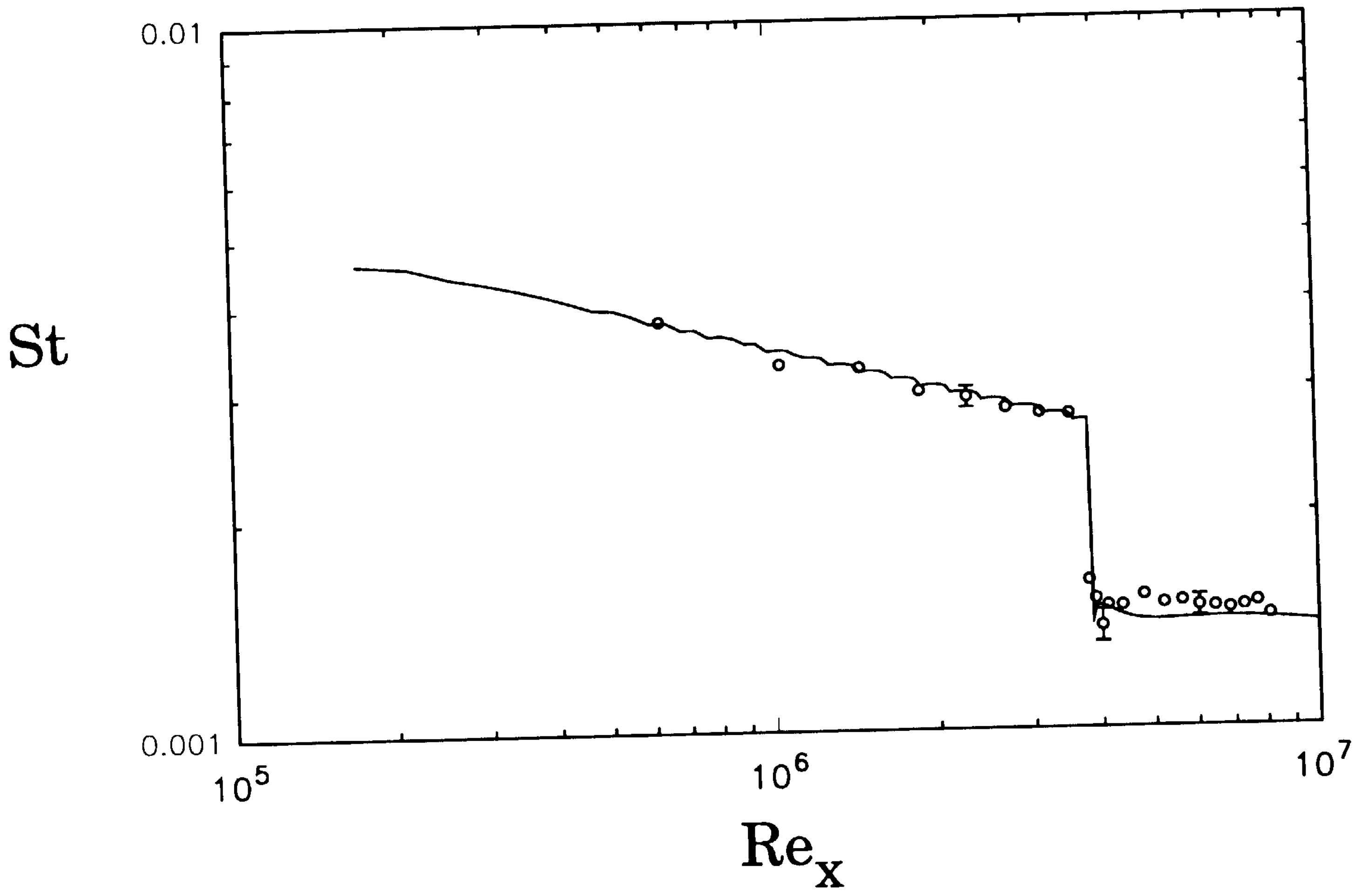

Figure 46. Comparison of base-aligned Stanton number predictions and data for U_∞ = 66 m/s.

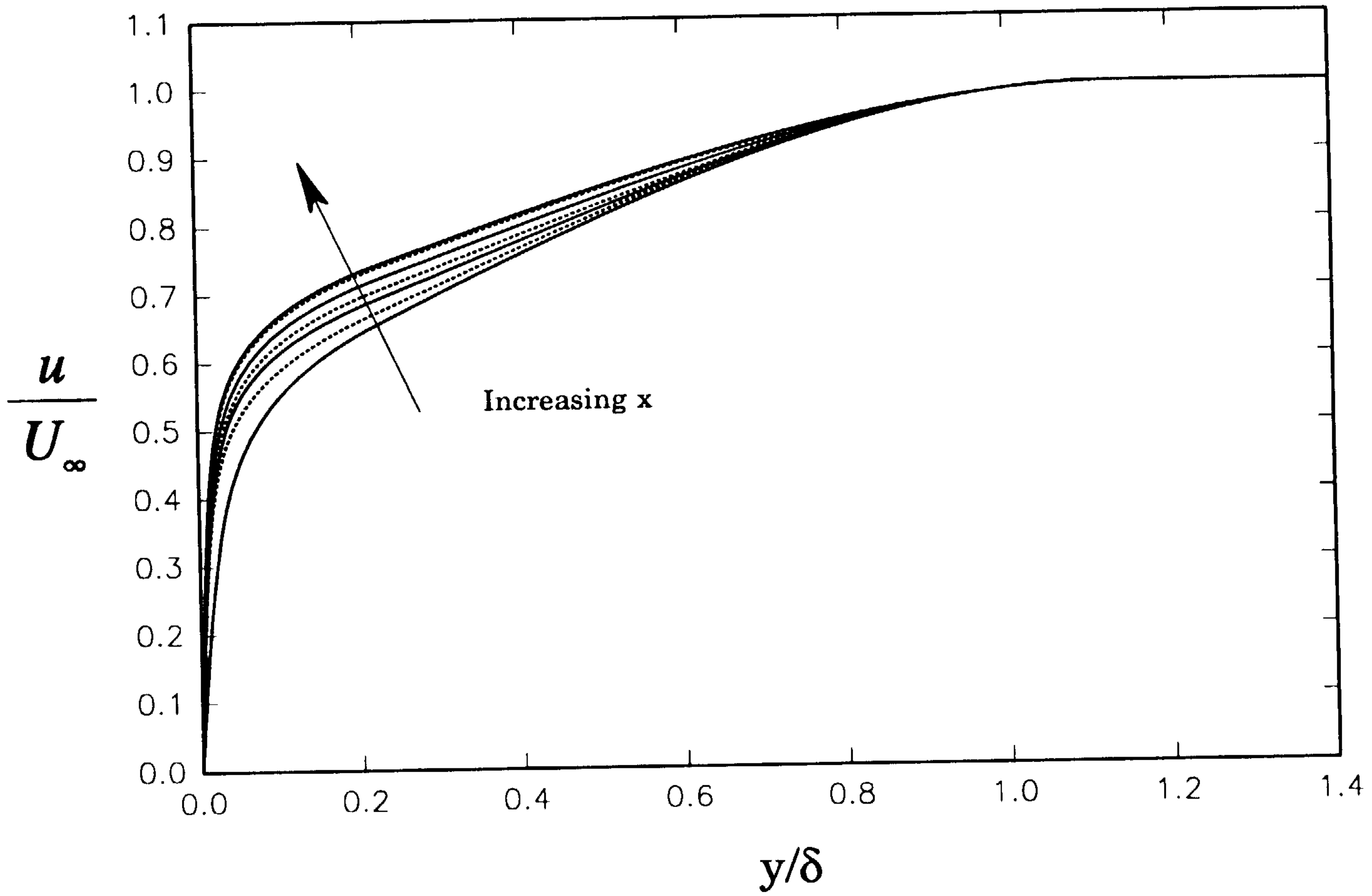

Figure 47. Velocity profile predictions for the rough-to-smooth surface at increasing x-locations (0.85 to 1.95 m) for U_∞ = 12 m/s.

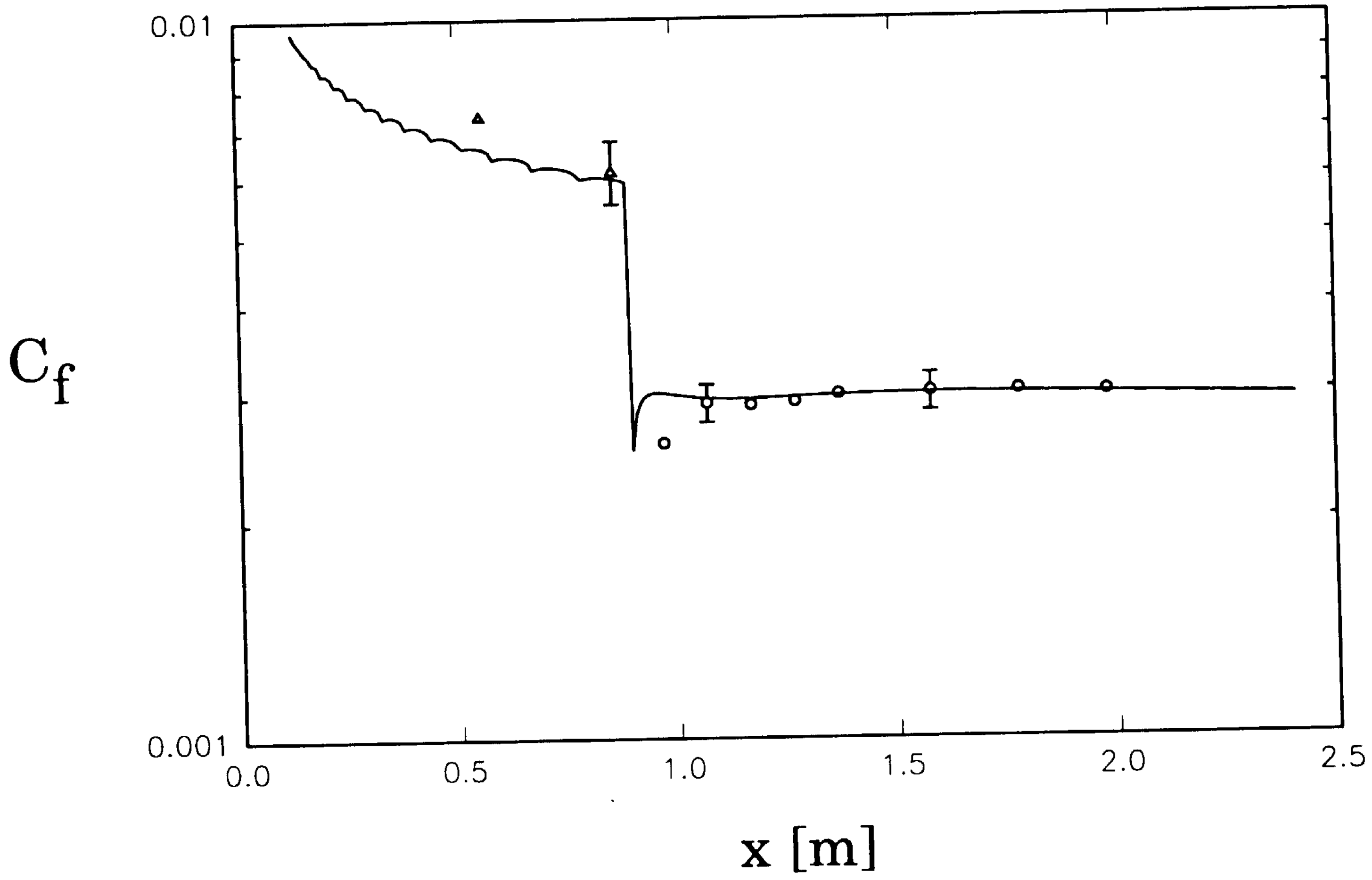

Figure 48. Comparison of base-aligned skin friction coefficient predictions and data for $U_\infty = 12$ m/s.

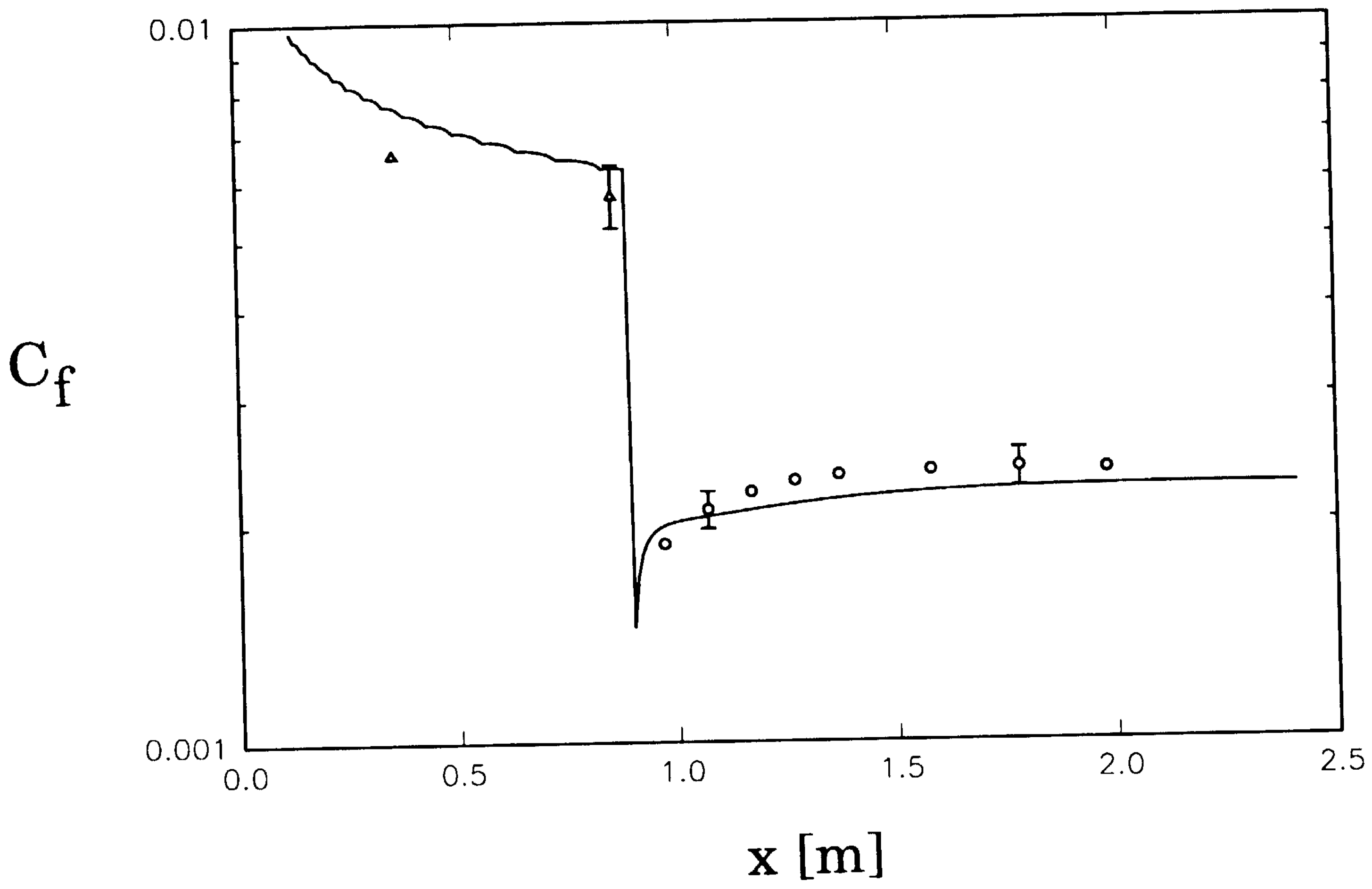

Figure 49. Comparison of base-aligned skin friction coefficient predictions and data for U_∞ = 58 m/s.

CHAPTER VI

SUMMARY AND CONCLUSIONS

The purpose of this research effort was to investigate the effects of a step change in surface roughness from rough to smooth on heat transfer and skin friction in the turbulent boundary layer. Heat transfer and fluid mechanics data were collected for zero pressure gradient, incompressible, constant wall temperature air flows over the rough-to-smooth surface. These data were collected for both alignments with the smooth surface aligned with the base of the hemispherical roughness elements and the smooth surface aligned with the crests of the roughness elements. The rough-to-smooth data were compared to previously reported THTTF all-rough surface data (Hosni 1989) and all-smooth surface data (Coleman et al., 1988).

For transitionally rough flow, the Stanton number after the rough-to-smooth interface quickly drops in a smooth, continuous fashion to the new smooth wall equilibrium value. For fully rough flows, on the other hand, the Stanton number undergoes an immediate drop to a value at or below the equivalent smooth-wall Stanton number at the same x-Reynolds number. The thermal boundary layer temperature profiles show the thermal boundary layer to slowly approach a smooth wall equilibrium profile. The alignment of the rough to smooth surfaces shows only a very small effect on the heat transfer between the base-aligned and crest aligned cases. Any effect that is observed between the two alignment cases is limited to the region just downstream of the rough-to-smooth interface.

The skin friction coefficient distributions behave very much like the Stanton number distributions. After the step change in surface roughness, the skin friction coefficient, C_f, falls below the equivalent smooth-wall values before approaching the smooth-wall values. Mean velocity and turbulence intensity profiles show the flow to rapidly assume smooth-wall behavior in the near wall region, while requiring more distance to assume a complete smooth-wall behavior. Also seen from the fluid mechanics data is the emergence of two layers in the flow field downstream of the rough-to-smooth interface. In addition to the external boundary layer, an internal layer develops which separates the rough-wall flow characteristics from the rapidly developing smooth-wall flow. There are no discernable differences between the two alignment cases for the fluid mechanics data.

Boundary layer computations using the standard discrete element method roughness model and mixing length turbulence model are shown to be in very good agreement with the data.

These tests indicate that data obtained with smooth heat flux gauges on otherwise rough SSME fuel pump turbine blades could have large errors. We recommend that heat flux data taken in this fashion be used with caution.

REFERENCES

______, 1986, Measurement Uncertainty, ANSI/ASME PTC 19.1-1985 Part 1.

Andreopoulous, J. and Wood, D.H., 1982, "The Response of a Turbulent Boundary Layer to a Short Length of Surface Roughness, Journal of Fluid Mechanics, Vol. 118, pp 143-164.

Antonia, R.A. and Luxton, R.E., 1971a, "The Response of a Turbulent Boundary Layer to a Step Change in Surface Roughness. Part 1. Smooth-to-Rough", Journal of Fluid Mechanics, Vol. 48, pp 721-726.

Antonia, R.A. and Luxton, R.E., 1971b, "The Response of a Turbulent Boundary Layer to an Upstanding Step Change in Surface Roughness", J. Basic Eng., Vol. 93, No. 1, pp 22-23.

Antonia, R.A. and Luxton, R.E., 1972, "The Response of a Turbulent Boundary Layer to a Step Change in Surface Roughness. Part 2. Rough-to-Smooth", Journal of Fluid Mechanics, Vol. 48, pp 721-726.

Brown, G.B., 1988, "Smooth Wall Qualification of a Turbulent Heat Transfer Test Facility", M.S. Thesis, Mech. and Nuc. Eng. Dept., Mississippi State University.

Coleman, H.W., Hosni, M.H., Taylor, R.P., and Brown, G.B., 1988, Smooth Wall Qualification of a Turbulent Heat Transfer Test Facility, Report TFD-88-2, Mech. and Nuc. Eng. Dept., Mississippi State University.

Coleman, H.W. and Steele, W.G., 1989, Experimentation and Uncertainty Analysis for Engineers, John Wiley and Sons, New York.

Eckert, R.G. and Goldstein, R.J., 1976, Measurements in Heat Transfer, 2nd edition, McGraw-Hill, New York.

Healzer, J.M. (1974), "The Turbulent Boundary Layer on a Rough, Porus Plate: Experimental Heat Transfer with Uniform Blowing," Ph.D. Dissertation, Mech. Eng. Dept., Stanford Univ. (Also Report HMT-18).

Hosni, M.H., 1989, "Measurement and Calculation of Surface Roughness Effects on Turbulent Flow and Heat Transfer," Ph.D. Dissertation, Mech. and Nuc. Eng. Dept., Mississippi State University.

Hosni, M.H., Coleman, H.W., and Taylor, R.P., 1989, "Measurement and Calculation of Surface Roughness Effects on Turbulent Flow and Heat Transfer", Report TFD-89-1, Mech. and Nuc. Eng. Dept., Mississippi State University.

Jacobs, W., 1939, Umformung eines turbulenten Geschwindigkeitsprofiles, Zeitschrift für Angewandte Mathematik and Mechanik, Vol 19, No. 2, pp 87-100. (Also NACA TM 951).

Kays, W.M. and Crawford, M.E., 1980, Convective Heat and Mass Transfer, 2nd edition, McGraw-Hill, New York, NY.

Norton, B.A., 1983, "Preliminary Analysis and Design of A Turbulent Heat Transfer Test Apparatus", M.S. Thesis, Mech. and Nuc. Eng. Dept., Mississippi State University.

Patel, V.C., 1965, "Calibration of the Preston Tube and Limitations on its Use in Pressure Gradients," Journal of Fluid Mechanics, Vol. 23, Part 1, pp. 185-208.

Preston, J.H., 1954, "The Determination of Turbulent Skin Friction by Means of Pitot Tubes," J. Roy. Aero. Soc., 58, 109.

Scaggs, W. F., Taylor, R. P., and Coleman, H. W., 1988, Measurement and prediction of rough wall effects on friction factor--uniform roughness results, J. Fluids Engr., Vol. 110, pp 385-391.

Schofield, W.H., 1975, "Measurements in Adverse-Pressure-Gradient Turbulent Boundary Layers with a Step Change in Surface Roughness", Journal of Fluid Mechanics, Vol. 70, pp 573-593.

Shang, J. S., Hankey, W. L., and Law, C. H., 1976, Numerical simulation of shock wave--turbulent boundary-layer interaction, AIAA J., Vol. 14, pp 1451-1457.

Suryanarayana, P.V.R., 1986, "Remote Data Acquisition and Control Techniques for Wind and Water Tunnel Experiments," M.S. Thesis, Mech. and Nuc. Eng. Dept., Mississippi State University.

Taylor, R. P., Coleman, H. W., and Hodge, B. K., 1984, A discrete element prediction approach for turbulent flow over rough surfaces, Report TFD-84-1, Mech. and Nuc. Eng. Dept., Mississippi State University.

Taylor, R. P., Coleman, H. W., and Hodge, B. K., 1985, Prediction of turbulent rough-wall skin friction using a discrete element approach, J. Fluids Engr., Vol. 107, pp 251-257.

APPENDIX A

EXPERIMENTAL STANTON NUMBER DETERMINATION AND ITS UNCERTAINTY ANALYSIS

Stanton Number Data Reduction Equation

The Stanton number is the nondimensional convective heat transfer coefficient and may be defined as

$$St = \frac{h}{\rho\, C_p\, U_\infty} \tag{22}$$

where

h is the convective heat transfer coefficient

ρ is the density of the freestream air

C_p is the specific heat of freestream air

U_∞ is the velocity of freestream air

The convective heat transfer coefficient for heat transfer from a test plate to the air in the tunnel is defined as

$$h = \frac{q}{A(T_p - T_o)} \tag{23}$$

where

q is the convective heat rate from the test plate

A is the plate area

T_p is the plate surface temperature

T_o is the freestream air total temperature

Solving equation (9) for the convective heat transfer coefficient and substituting into equation (8) gives the Stanton number at each test plate as

$$St = \frac{q}{\rho\, C_p\, U_\infty A\,(T_p - T_o)} \tag{24}$$

Since the convective heat transfer rate, q, will be determined, it is required that the corresponding radiation and conduction heat losses be known. Figure 41 shows the modes of heat exchange from each plate. Application of an energy balance to a plate gives

$$W = q + q_c + q_r \tag{25}$$

where

W is power supplied to the plate heater pad

q_r is the radiation heat loss rate

q_c is the conduction heat loss rate

Solving equation (11) for the convective heat transfer rate and substituting into equation (10) yields

$$St = \frac{W - q_c - q_r}{\rho\, C_p\, U_\infty A\,(T_p - T_o)} \tag{26}$$

The radiation heat loss is modeled using

$$q_r = \sigma \varepsilon\, A\,(T_p^{\,4} - T_r^{\,4}) \tag{27}$$

where

σ is the Stefan-Boltzmann constant

ε	is the test plate emissivity
T_r	is the freestream recovery temperature

The conduction heat loss rate is modeled using

$$q_c = (UA)_{pr}(T_p - T_{rail}) + (U)_{pp}(T_p - T_{p-1}) + (UA)_{pp}(T_p - T_{p+1}) \tag{28}$$

where

$(UA)_{pr}$	is the experimentally-determined effective conductance between a test plate and the side rails
$(UA)_{pp}$	is the experimentally-determined effective conductance between two adjoining test plates
T_{rail}	is the side rail temperature at the axial location of the plate
T_{p-1}	the temperature of the previous adjoining plate
T_{p+1}	the temperature of the next adjoining plate

Substitution of equations (13) and (14) into equation (12) gives the final form of the data reduction equation for the experimentally determined Stanton number

$$St = \frac{W - (UA)_{pr}(T_p - T_{rail}) - (UA)_{pp}((T_p - T_{p-1}) + (T_p - T_{p+1})) - \sigma \varepsilon A (T_p{}^4 - T_r{}^4)}{\rho\, C_p\, U_\infty A\, (T_p - T_o)} \tag{29}$$

Most of the variables involved in the experimentally determined Stanton number are shown explicitly in this expression. However, additional variable are used in the calculation of the static and total temperature of the freestream air and in the moist air property calculations for specific heat and density. The freestream air total and static temperatures are calculated using the measured recovery temperature and a recovery factor, R, (Eckert and Goldstein, 1976) for the probe:

$$T_o = T_r + (1 - R)\frac{U_\infty^2}{2C_p} \tag{30}$$

$$T_\infty = T_r - (R)\frac{U_\infty^2}{2C_p} \tag{31}$$

The functional relationships for the moist air specific heat and density calculations are

$$C_p = C_p(T_\infty, T_{wb}, P_{baro}, C_{p_{air}}, C_{p_{H_2O}}) \tag{32}$$

$$\rho = \rho(T_\infty, T_{wb}, P_{baro}) \tag{33}$$

where

T_∞ is the freestream air dry-bulb temperature

T_{wb} is the freestream air wet-bulb temperature

P_{baro} is the barometric pressure

$C_{p_{air}}$ is the specific heat of dry air

$C_{p_{H_2O}}$ is the specific heat of water vapor

In order to determine the Stanton number for each plate, the following sixteen variables must be measured or found from a reference source:

- Plate heater power (W)
- Recovery temperature (T_r)
- Plate temperature (T_p)
- Plate temperature (T_{p-1})
- Plate temperature (T_{p+1})
- Rail temperature (T_{rail})

- Wet-bulb temperature (T_{wb})
- Plate-to-rail effective conductance $(UA)_{pr}$
- Plate-to-plate effective conductance $(UA)_{pp}$
- Plate area (A)
- Barometric pressure (P_{baro})
- Specific heat of dry air $C_{p\,air}$
- Specific heat of water vapor C_{pH_2O}
- Freestream air velocity (U_∞)
- Recovery factor (R)
- Emissivity (ε)

Uncertainty Analysis Overview

The detailed uncertainty analysis is consistent with the 1986 ANSI/ASME Standard on Measurement Uncertainty and follows the procedure of Coleman and Steele (1989). The uncertainty, U_r, in an experimentally determined result, r, defines the interval r ± U_r within which the true result lies with a 95 percent confidence. Here U_r is the uncertainty in the result determined from a root-sum-square combination of the bias limit of the result, B_r, and the precision limit of the result, P_r.

$$U_r = (B_r^2 + P_r^2)^{1/2} \tag{34}$$

For the Stanton number which is a function of sixteen variables, X_j

$$r = r(X_1, X_2, \ldots, X_j) \tag{35}$$

The propagation of precision limits, P_{X_j}, of the measured variables and parameters into the result is given by

$$P_r = \left\{ \sum_{i=1}^{J} [\frac{\partial r}{\partial X_1} P_{X_i}]^2 \right\}^{1/2} \tag{36}$$

The propagation of bias limits, B_{X_j}, of the measured variables and parameters into the result is given by

$$B_r = \left\{ \left[\sum_{i=1}^{J} (\frac{\partial r}{\partial X_i} B_{X_i})^2 \right] + 2 (\frac{\partial r}{\partial X_1}) (\frac{\partial r}{\partial X_2}) B_{X_1}{}' B_{X_2}{}' + \ldots \right\}^{1/2} \tag{37}$$

The primed terms on the right hand side of equation (23) represent the portions of bias limits of two variables which are perfectly correlated. For this case, the bulb thermistors used to measure various temperatures in the THTTF were all calibrated against the same standard. Therefore, a portion of the bias limit for each thermistor is perfectly correlated with a portion of the bias limits of the other thermistors.

Previous work in the THTTF [Coleman et al. (1988)] has shown that most of the experiments in this facility are bias limit dominated. All of the P_{X_j}'s are negligible when compared to the bias limits. Therefore,

$$P_{St} = 0 \,. \tag{38}$$

An exception to this occurs at low freestream velocities ($U_\infty \leq 12$ m/s), for which the heat transfer coefficients are low. At these conditions, the time constant of the THTTF is large enough that a tight steady state is hard to maintain. This is due mainly because of fluctuations in the line voltage to the test plate heater circuits and fluctuations in the temperature of the incoming cooling water. After observations of the St results for eight U_∞ = 12 m/s replications with the smooth wall and three U_∞ = 6 m/s replications with the rough wall, the 95% confidence estimate of P_{St} = 3%

was determined. This is present because of system unsteadiness and not because of measurement uncertainty [Coleman et al. (1988)].

Applying equation (23) to equation (15) gives

$$\begin{aligned}
B_{St}^2 = {} & \left(\frac{\partial St}{\partial T_p}\right)^2 B_{T_p}^2 + \left(\frac{\partial St}{\partial T_{p_{i-1}}}\right)^2 B_{T_{p_{i-1}}}^2 + \left(\frac{\partial St}{\partial T_{p_{i+1}}}\right)^2 B_{T_{p_{i+1}}}^2 + \left(\frac{\partial St}{\partial T_r}\right)^2 B_{T_r}^2 \\
& + \left(\frac{\partial St}{\partial T_{rail}}\right)^2 B_{T_{rail}}^2 + \left(\frac{\partial St}{\partial T_{wb}}\right)^2 B_{T_{wb}}^2 + \left(\frac{\partial St}{\partial W}\right)^2 B_W^2 + \left(\frac{\partial St}{\partial U_\infty}\right)^2 B_{U_\infty}^2 \\
& + \left(\frac{\partial St}{\partial P_{baro}}\right)^2 B_{P_{baro}}^2 + \left(\frac{\partial St}{\partial R}\right)^2 B_R^2 + \left(\frac{\partial St}{\partial A}\right)^2 B_A^2 + \left(\frac{\partial St}{\partial C_{p_{air}}}\right)^2 B_{C_{p_{air}}}^2 \\
& + \left(\frac{\partial St}{\partial C_{p_{H_2O}}}\right)^2 B_{C_{p_{H_2O}}}^2 + \left(\frac{\partial St}{\partial (UA)_{pr}}\right)^2 B_{(UA)_{pr}}^2 + \left(\frac{\partial St}{\partial (UA)_{pp}}\right)^2 B_{(UA)_{pp}}^2 + \left(\frac{\partial St}{\partial \varepsilon}\right)^2 B_\varepsilon^2 \\
& + 2\left(\frac{\partial St}{\partial T_p}\right)\left(\frac{\partial St}{\partial T_{p_{i-1}}}\right) B_{T_p}{}' B_{T_{p_{i-1}}}{}' + 2\left(\frac{\partial St}{\partial T_p}\right)\left(\frac{\partial St}{\partial T_{p_{i+1}}}\right) B_{T_p}{}' B_{T_{p_{i+1}}}{}' + 2\left(\frac{\partial St}{\partial T_p}\right)\left(\frac{\partial St}{\partial T_r}\right) B_{T_p}{}' B_{T_r}{}' \\
& + 2\left(\frac{\partial St}{\partial T_p}\right)\left(\frac{\partial St}{\partial T_{rail}}\right) B_{T_p}{}' B_{T_{rail}}{}' + 2\left(\frac{\partial St}{\partial T_r}\right)\left(\frac{\partial St}{\partial T_{rail}}\right) B_{T_r}{}' B_{T_{rail}}{}' + 2\left(\frac{\partial St}{\partial T_r}\right)\left(\frac{\partial St}{\partial T_{p_{i-1}}}\right) B_{T_r}{}' B_{T_{p_{i-1}}}{}' \\
& + 2\left(\frac{\partial St}{\partial T_r}\right)\left(\frac{\partial St}{\partial T_{p_{i+1}}}\right) B_{T_r}{}' B_{T_{p_{i+1}}}{}' + 2\left(\frac{\partial St}{\partial T_{rail}}\right)\left(\frac{\partial St}{\partial T_{p_{i-1}}}\right) B_{T_{rail}}{}' B_{T_{p_{i-1}}}{}' \\
& + 2\left(\frac{\partial St}{\partial T_{rail}}\right)\left(\frac{\partial St}{\partial T_{p_{i+1}}}\right) B_{T_{rail}}{}' B_{T_{p_{i+1}}}{}' + 2\left(\frac{\partial St}{\partial T_{p_{i-1}}}\right)\left(\frac{\partial St}{\partial T_{p_{i+1}}}\right) B_{T_{p_{i-1}}}{}' B_{T_{p_{i+1}}}{}'
\end{aligned} \tag{39}$$

Previous work in the THTTF has determined the following bias limits and nominal values for each of the sixteen variables involved in the calculation of the Stanton number. A detailed description of these estimates is given by Coleman et al. (1988) and Hosni et al. (1989). The values listed in parenthesis are the nominal values for the 2.54 cm wide plates immediately downstream of the rough-to-smooth interface.

Variable	Bias Limit	Nominal Values
Plate Temperature	0.14 C	45 C
Rail Temperature	0.4 C	45 C
Recovery Temperature	0.10 C	30 C
Wet-Bulb Temperature	1.0 C	27 C
Barometric Pressure	1.0 mm Hg	760 mm Hg
Recovery Factor	0.09	0.86
Power	0.9%	20-150 W (3-18 W)
Area	0.03%	464.5 cm^2 (116.1 cm^2)
Freestream Velocity	0.04%	6-70 m/s
$C_{p_{air}}$	0.5%	1.006 kJ/kg K
$C_{p_{H_2O}}$	0.5%	1.86 kJ/kg K
$(UA)_{pr}$	45%	0.42 W/C (0.105 W/C)
$(UA)_{pp}$	45%	1.25 W/C
Emissivity	45%	0.11

Since the same calibration standard was used in the temperature calibration, the following bias limits are correlated

$$B_{T_p}{}' = B_{T_{p+1}}{}' = B_{T_{p-1}}{}' = B_{T_r}{}' = B_{T_{rail}}{}' = 0.04\ C$$

A jitter program, as discussed by Coleman and Steele (1989), was used to determine the uncertainty estimate for each experimentally determined Stanton number. The jitter program uses the Stanton number data reduction equation as a subroutine and approximates the partial derivatives in equation (25) using a finite difference scheme. Using this method, the Stanton number is first calculated using the original values of the sixteen variables for all twenty-four plates. Next, using a loop in the data reduction program, the partial derivative of Stanton number with respect to a particular variable is approximated by perturbing the variable a specified amount and recalculating the Stanton number for all of the plates. The partial derivative of Stanton with respect to the variable is the difference between the new Stanton number and the original Stanton number divided by the perturbation. The variables are then reset to their original values and the next variable is perturbed.

After all of the partial derivatives have been calculated, the bias estimate for the uncertainty in the Stanton number is calculated directly from equation (25) using the partial derivatives and the previously stated bias limits.

The overall uncertainty for the Stanton numbers reported in Chapter III ranged from 2 to 5 percent for the 10.2 cm wide plates, depending upon the flow conditions. For the 2.54 cm wide plate downstream of the rough-to-smooth interface, the uncertainty in the Stanton number was found to be from 3 to 11 percent, dependent upon the flow conditions.

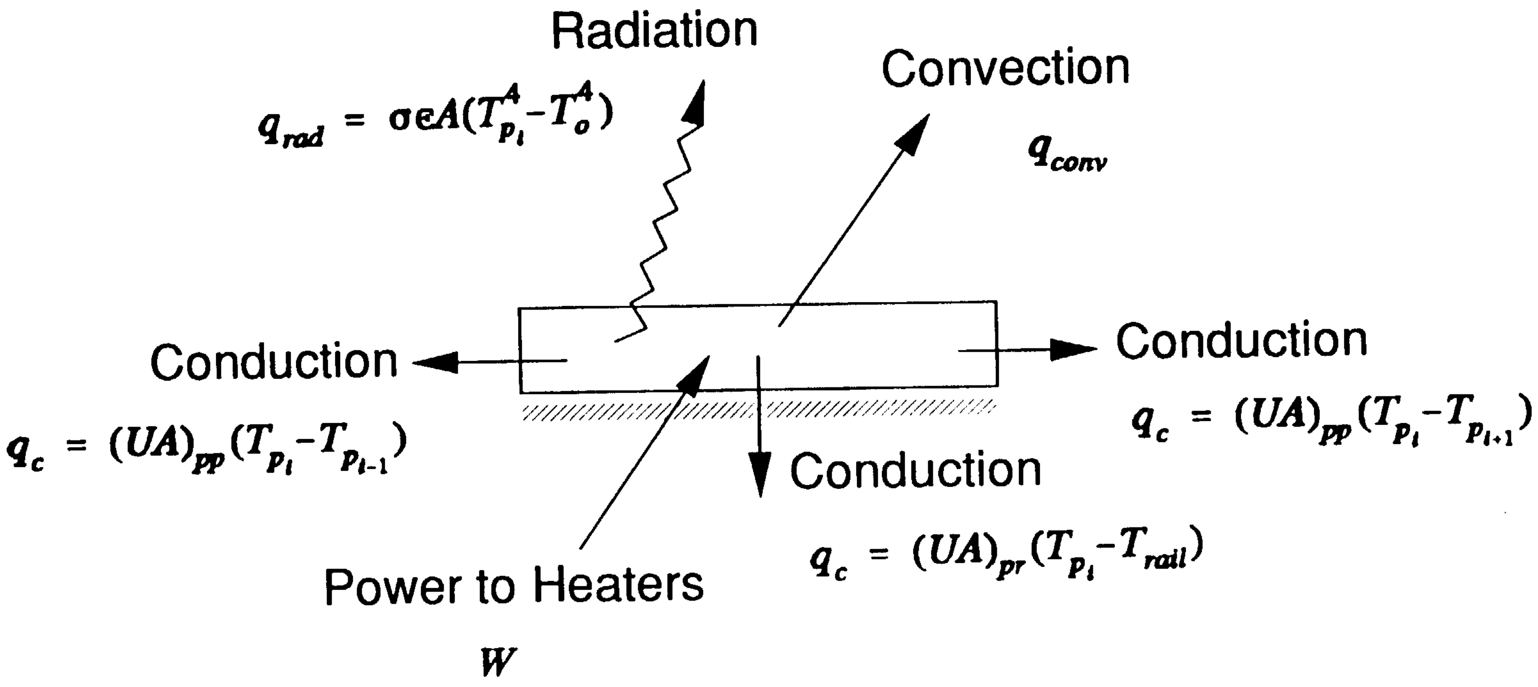

Figure 50. Energy balance of a test plate.

APPENDIX B

TABULATION OF EXPERIMENTAL DATA

Tabular listings of the experimental Stanton number and the skin friction coefficient data are presented in this Appendix. These data correspond to measurements of boundary layer flows over the rough-to-smooth test surface for both the base-aligned and crest-aligned cases. Stanton number data for both alignments are presented for freestream velocities of 6, 12, 27, 43, 58, and 66 m/s. Skin friction coefficient data for both alignments for freesteam velocities of 12 and 58 m/s are presented.

As described in Appendix A, the Stanton number data were determined from an energy balance applied to each test plate. Plate 1 and plate 24 were considered as guard heaters and are not shown on the plots of heat transfer data. Their uncertainties are not reported in the listings. These data are marked with an * in the following tabular listings.

The first six digits of the "RUN" designation indicate the date in month, day, and year. The number after the dash is the run number for that particular day.

Stanton Number Data (Base-Aligned Case)

Table 1. Stanton number data for the base-aligned case for U_∞ = 6 m/s.

RUN : 081790-1
U = 6.0 m/s   Pbar = 76.0 cm Hg   Tub = 18.9 C
Rho = 1.17 kg/m^3   Cp = 1.01 kJ/kg C   Mu = 1.86E-05 kg/m s
Tr = 27.6 C   T = 27.6 C   To = 27.6 C

PL	x(m)	Tw(C)	W(W)	Qc(W)	Qr(W)	Rex	St	U (%)
1	0.05	44.8	19.1	1.82	0.59	1.90E+04	0.00295	0.0 *
2	0.15	44.8	12.1	1.20	0.59	5.71E+04	0.00182	8.5
3	0.25	44.7	9.7	0.54	0.59	9.52E+04	0.00153	8.4
4	0.36	44.8	11.6	0.44	0.59	1.33E+05	0.00188	6.7
5	0.46	44.8	18.8	0.40	0.59	1.71E+05	0.00315	4.9
6	0.56	44.7	24.8	-0.10	0.59	2.09E+05	0.00435	4.3
7	0.66	44.6	25.2	-0.11	0.58	2.48E+05	0.00441	4.3
8	0.76	44.7	23.7	-0.01	0.59	2.86E+05	0.00412	4.4
9	0.86	44.7	22.2	-0.12	0.59	3.24E+05	0.00387	4.5
10	0.93	44.7	4.5	0.07	0.15	3.48E+05	0.00308	10.7
11	0.95	44.7	4.6	-0.01	0.15	3.57E+05	0.00319	10.4
12	0.98	44.7	3.8	0.01	0.15	3.67E+05	0.00256	12.6
13	1.00	44.7	4.1	0.10	0.15	3.76E+05	0.00275	11.9
14	1.07	44.6	15.3	0.18	0.58	4.00E+05	0.00260	5.4
15	1.17	44.6	15.5	0.29	0.58	4.38E+05	0.00263	5.6
16	1.27	44.6	14.4	0.37	0.58	4.76E+05	0.00241	5.8
17	1.37	44.8	14.8	0.61	0.59	5.14E+05	0.00242	5.8
18	1.47	44.7	14.0	0.35	0.59	5.52E+05	0.00233	5.9
19	1.57	44.7	14.0	0.28	0.59	5.90E+05	0.00234	5.8
20	1.68	44.7	13.7	0.37	0.59	6.28E+05	0.00227	6.1
21	1.78	44.8	14.2	0.84	0.59	6.67E+05	0.00226	6.3
22	1.88	44.8	14.6	0.84	0.59	7.05E+05	0.00233	6.5
23	1.98	44.8	13.7	1.04	0.59	7.43E+05	0.00213	7.3
24	2.08	44.8	25.5	1.74	0.59	7.81E+05	0.00410	0.0 *

Table 2. Stanton number data for the base-aligned case for U_∞ = 12 m/s.

RUN : 081590-1
U = 12.0 m/s
Rho = 1.17 kg/m^3
Tr = 26.5 C

Pbar = 76.1 cm Hg
Cp = 1.01 kJ/kg C
T = 26.4 C

Twb = 18.3 C
Mu = 1.86E-05 kg/m s
To = 26.5 C

PL	x(m)	Tw(C)	W(W)	Qc(W)	Qr(W)	Rex	St	U (%)
1	0.05	44.1	44.4	0.00	0.00	0.00E+00	0.00000	0.0 *
2	0.15	44.0	72.9	0.66	0.60	1.15E+05	0.00614	1.9
3	0.25	44.1	55.2	0.56	0.60	1.92E+05	0.00461	2.1
4	0.36	44.1	51.4	0.13	0.60	2.69E+05	0.00433	2.1
5	0.46	44.0	45.3	-0.09	0.60	3.46E+05	0.00383	2.2
6	0.56	44.0	42.6	-0.25	0.60	4.23E+05	0.00363	2.3
7	0.66	44.0	40.1	-0.20	0.60	5.00E+05	0.00340	2.3
8	0.76	44.0	38.8	-0.48	0.60	5.77E+05	0.00333	2.4
9	0.86	44.0	38.6	-0.17	0.60	6.54E+05	0.00327	2.4
10	0.93	44.0	6.9	-0.08	0.15	7.02E+05	0.00234	7.4
11	0.95	44.0	6.5	-0.13	0.15	7.21E+05	0.00224	7.7
12	0.98	44.1	5.7	-0.04	0.15	7.40E+05	0.00191	8.7
13	1.00	44.1	6.1	-0.05	0.15	7.60E+05	0.00205	8.2
14	1.07	44.1	23.8	0.07	0.60	8.08E+05	0.00197	4.4
15	1.17	44.1	24.5	0.20	0.60	8.85E+05	0.00203	4.4
16	1.27	44.1	23.2	0.28	0.60	9.61E+05	0.00191	4.5
17	1.37	44.1	23.4	0.28	0.60	1.04E+06	0.00192	4.4
18	1.47	44.1	22.7	0.11	0.60	1.12E+06	0.00188	4.5
19	1.57	44.1	22.8	0.11	0.60	1.19E+06	0.00189	4.4
20	1.68	44.1	22.6	0.23	0.60	1.27E+06	0.00186	4.5
21	1.78	44.1	22.7	0.42	0.60	1.35E+06	0.00185	4.6
22	1.88	44.1	23.6	0.62	0.60	1.42E+06	0.00191	4.6
23	1.98	44.1	22.9	1.04	0.60	1.50E+06	0.00181	4.9
24	2.08	44.1	36.1	0.00	0.00	0.00E+00	0.00000	0.0 *

Table 3. Stanton number data for the base-aligned case for $U_\infty = 27$ m/s.

RUN : 081690-1
U = 27.9 m/s
Rho = 1.17 kg/m^3
Tr = 26.9 C

Pbar = 76.1 cm Hg
Cp = 1.01 kJ/kg C
T = 26.6 C

Twb = 18.3 C
Mu = 1.86E-05 kg/m s
To = 27.0 C

PL	x(m)	Tw(C)	W(W)	Qc(W)	Qr(W)	Rex	St	U (%)
1	0.05	44.5	166.6	1.74	0.60	8.90E+04	0.00610	0.0 *
2	0.15	44.4	123.6	1.18	0.60	2.67E+05	0.00454	1.7
3	0.25	44.4	102.4	0.60	0.60	4.45E+05	0.00378	1.7
4	0.36	44.4	99.2	0.42	0.60	6.23E+05	0.00367	1.7
5	0.46	44.4	90.1	0.13	0.60	8.01E+05	0.00334	1.8
6	0.56	44.5	88.2	0.41	0.60	9.79E+05	0.00324	1.8
7	0.66	44.4	83.8	0.19	0.60	1.16E+06	0.00309	1.8
8	0.76	44.4	82.1	-0.11	0.60	1.34E+06	0.00305	1.8
9	0.86	44.5	81.9	0.30	0.60	1.51E+06	0.00301	1.8
10	0.93	44.4	12.7	-0.18	0.15	1.62E+06	0.00190	4.1
11	0.95	44.4	12.0	0.03	0.15	1.67E+06	0.00176	4.3
12	0.98	44.5	10.9	0.07	0.15	1.71E+06	0.00159	4.7
13	1.00	44.5	11.4	0.01	0.15	1.76E+06	0.00166	4.5
14	1.07	44.5	46.1	0.48	0.60	1.87E+06	0.00167	2.2
15	1.17	44.5	47.2	0.53	0.60	2.05E+06	0.00171	2.2
16	1.27	44.5	46.1	0.70	0.60	2.23E+06	0.00166	2.2
17	1.37	44.5	45.9	0.38	0.60	2.40E+06	0.00167	2.2
18	1.47	44.5	45.7	0.52	0.60	2.58E+06	0.00165	2.2
19	1.57	44.5	45.7	0.37	0.60	2.76E+06	0.00166	2.2
20	1.68	44.4	45.1	0.35	0.60	2.94E+06	0.00164	2.2
21	1.78	44.5	46.0	0.65	0.60	3.12E+06	0.00166	2.2
22	1.88	44.5	46.6	0.83	0.60	3.29E+06	0.00168	2.3
23	1.98	44.5	44.4	1.03	0.60	3.47E+06	0.00159	2.4
24	2.08	44.5	62.3	1.47	0.60	3.65E+06	0.00224	0.0 *

Table 4. Stanton number data for the base-aligned case for U_∞ = 43 m/s.

RUN : 081690-2
U = 43.0 m/s
Rho = 1.16 kg/m^3
Tr = 28.9 C

Pbar = 76.0 cm Hg
Cp = 1.01 kJ/kg C
T = 28.1 C

Twb = 19.4 C
Mu = 1.86E-05 kg/m s
To = 29.0 C

PL	x(m)	Tw(C)	W(W)	Qc(W)	Qr(W)	Rex	St	U (%)
1	0.05	44.4	216.7	1.79	0.54	1.36E+05	0.00591	0.0 *
2	0.15	44.2	147.0	0.66	0.53	4.09E+05	0.00406	1.8
3	0.25	44.4	127.0	0.52	0.53	6.82E+05	0.00348	1.8
4	0.36	44.4	125.1	0.27	0.54	9.55E+05	0.00341	1.9
5	0.46	44.4	114.6	0.10	0.54	1.23E+06	0.00313	1.9
6	0.56	44.3	110.4	-0.43	0.53	1.50E+06	0.00305	1.9
7	0.66	44.4	107.3	-0.11	0.54	1.77E+06	0.00294	1.9
8	0.76	44.4	105.0	-0.34	0.54	2.05E+06	0.00289	1.9
9	0.86	44.4	105.0	-0.22	0.54	2.32E+06	0.00288	1.9
10	0.93	44.3	15.6	-0.11	0.13	2.49E+06	0.00172	3.7
11	0.95	44.3	14.4	-0.18	0.13	2.56E+06	0.00160	3.9
12	0.98	44.4	13.5	0.10	0.13	2.63E+06	0.00146	4.1
13	1.00	44.3	13.8	-0.26	0.13	2.69E+06	0.00154	4.0
14	1.07	44.3	56.6	0.16	0.53	2.86E+06	0.00154	2.1
15	1.17	44.3	58.1	0.25	0.53	3.14E+06	0.00159	2.1
16	1.27	44.4	57.2	0.36	0.53	3.41E+06	0.00155	2.1
17	1.37	44.4	58.1	0.51	0.54	3.68E+06	0.00157	2.1
18	1.47	44.4	56.5	0.18	0.53	3.96E+06	0.00154	2.2
19	1.57	44.3	56.7	0.06	0.53	4.23E+06	0.00155	2.2
20	1.68	44.4	57.1	0.49	0.54	4.50E+06	0.00154	2.1
21	1.78	44.4	57.8	0.56	0.54	4.77E+06	0.00156	2.1
22	1.88	44.4	57.6	0.68	0.53	5.05E+06	0.00156	2.2
23	1.98	44.3	55.7	0.90	0.53	5.32E+06	0.00150	2.2
24	2.08	44.4	72.7	1.63	0.53	5.59E+06	0.00195	0.0 *

Table 5. Stanton number data for the base-aligned case for U_∞ = 58 m/s.

RUN : 081390-2
U = 58.1 m/s Pbar = 76.2 cm Hg Twb = 20.0 C
Rho = 1.16 kg/m^3 Cp = 1.01 kJ/kg C Mu = 1.86E-05 kg/m s
Tr = 31.2 C T = 29.8 C To = 31.5 C

PL	x(m)	Tw(C)	W(W)	Qc(W)	Qr(W)	Rex	St	U (%)
1	0.05	44.3	224.5	1.81	0.46	1.84E+05	0.00546	0.0 *
2	0.15	44.3	158.2	1.18	0.45	5.51E+05	0.00386	2.4
3	0.25	44.2	135.3	0.41	0.45	9.18E+05	0.00333	2.4
4	0.36	44.2	133.2	0.17	0.45	1.28E+06	0.00329	2.5
5	0.46	44.2	122.3	-0.03	0.45	1.65E+06	0.00303	2.5
6	0.56	44.1	118.9	-0.37	0.45	2.02E+06	0.00296	2.6
7	0.66	44.1	115.1	-0.30	0.45	2.39E+06	0.00286	2.5
8	0.76	44.1	113.0	-0.48	0.45	2.75E+06	0.00282	2.6
9	0.86	44.2	113.3	-0.37	0.45	3.12E+06	0.00281	2.6
10	0.93	44.2	16.7	-0.04	0.11	3.35E+06	0.00165	3.9
11	0.95	44.2	15.6	-0.12	0.11	3.44E+06	0.00155	4.1
12	0.98	44.2	14.3	-0.06	0.11	3.53E+06	0.00142	4.3
13	1.00	44.2	15.1	-0.08	0.11	3.63E+06	0.00150	4.1
14	1.07	44.2	60.9	-0.04	0.45	3.85E+06	0.00150	2.7
15	1.17	44.2	63.5	0.54	0.45	4.22E+06	0.00155	2.6
16	1.27	44.1	61.1	0.22	0.45	4.59E+06	0.00151	2.7
17	1.37	44.2	62.4	0.52	0.45	4.96E+06	0.00152	2.6
18	1.47	44.2	60.9	0.18	0.45	5.32E+06	0.00150	2.6
19	1.57	44.3	61.8	0.43	0.45	5.69E+06	0.00150	2.6
20	1.68	44.2	60.8	0.34	0.45	6.06E+06	0.00149	2.6
21	1.78	44.1	61.1	0.34	0.45	6.42E+06	0.00150	2.6
22	1.88	44.2	61.9	0.65	0.45	6.79E+06	0.00151	2.6
23	1.98	44.2	60.2	0.97	0.45	7.16E+06	0.00146	2.6
24	2.08	44.2	74.7	1.48	0.45	7.53E+06	0.00181	0.0 *

Table 6. Stanton number data for the base-aligned case for U_∞ = 66 m/s.

RUN : 081490-1
U = 66.3 m/s   Pbar = 76.1 cm Hg   Twb = 21.1 C
Rho = 1.15 kg/m^3   Cp = 1.01 kJ/kg C   Mu = 1.86E-05 kg/m s
Tr = 33.5 C   T = 31.6 C   To = 33.8 C

PL	x(m)	Tw(C)	W(W)	Qc(W)	Qr(W)	Rex	St	U (%)
1	0.05	44.3	205.7	1.98	0.38	2.08E+05	0.00538	0.0 *
2	0.15	44.2	145.5	1.32	0.38	6.24E+05	0.00382	3.3
3	0.25	44.2	125.1	0.58	0.38	1.04E+06	0.00330	3.4
4	0.36	44.2	123.1	0.22	0.38	1.46E+06	0.00326	3.4
5	0.46	44.2	113.7	0.12	0.38	1.87E+06	0.00300	3.4
6	0.56	44.2	110.5	-0.30	0.38	2.29E+06	0.00294	3.5
7	0.66	44.2	106.6	-0.22	0.38	2.71E+06	0.00283	3.5
8	0.76	44.2	104.5	-0.41	0.38	3.12E+06	0.00278	3.5
9	0.86	44.3	105.3	-0.18	0.38	3.54E+06	0.00278	3.5
10	0.93	44.2	15.2	-0.11	0.09	3.80E+06	0.00162	4.8
11	0.95	44.2	14.3	-0.07	0.09	3.90E+06	0.00152	4.9
12	0.98	44.2	13.0	-0.14	0.09	4.01E+06	0.00139	5.2
13	1.00	44.2	14.0	-0.10	0.09	4.11E+06	0.00149	5.0
14	1.07	44.2	56.6	0.16	0.38	4.37E+06	0.00149	3.5
15	1.17	44.3	58.6	0.54	0.38	4.79E+06	0.00153	3.4
16	1.27	44.3	57.5	0.75	0.38	5.20E+06	0.00149	3.4
17	1.37	44.2	57.0	0.36	0.38	5.62E+06	0.00150	3.5
18	1.47	44.3	56.8	0.57	0.38	6.03E+06	0.00147	3.4
19	1.57	44.3	56.4	0.34	0.38	6.45E+06	0.00147	3.5
20	1.68	44.2	55.6	0.26	0.38	6.87E+06	0.00146	3.5
21	1.78	44.2	56.6	0.53	0.38	7.28E+06	0.00148	3.4
22	1.88	44.2	56.7	0.50	0.38	7.70E+06	0.00149	3.5
23	1.98	44.2	55.0	0.90	0.38	8.12E+06	0.00143	3.4
24	2.08	44.2	66.8	1.38	0.38	8.53E+06	0.00174	0.0 *

Stanton Number Data (Crest-Aligned Case)

Table 7. Stanton number data for the crest-aligned case for $U_\infty = 6$ m/s.

```
RUN :  102390-1
U   =   6.0 m/s          Pbar = 75.9 cm Hg       Tub = 16.7 C
Rho =  1.18 kg/m^3       Cp   = 1.01 kJ/kg C     Mu  = 1.86E-05 kg/m s
Tr  =  25.2 C            T    = 25.2 C           To  = 25.2 C
```

PL	x(m)	Tw(C)	W(W)	Qc(W)	Qr(W)	Rex	St	U (%)
1	0.05	44.1	19.4	1.31	0.64	1.92E+04	0.00279	0.0 *
2	0.15	44.1	12.3	0.73	0.64	5.75E+04	0.00175	7.2
3	0.25	44.1	10.2	0.29	0.64	9.58E+04	0.00149	7.4
4	0.36	44.2	12.6	0.19	0.64	1.34E+05	0.00187	6.2
5	0.46	44.1	20.4	-0.27	0.64	1.72E+05	0.00321	4.6
6	0.56	44.2	28.1	0.02	0.65	2.11E+05	0.00436	4.1
7	0.66	44.2	27.3	-0.22	0.64	2.49E+05	0.00429	4.2
8	0.76	44.1	25.3	-0.38	0.64	2.87E+05	0.00400	4.3
9	0.86	44.2	23.7	-0.15	0.64	3.26E+05	0.00371	4.4
10	0.93	44.1	5.1	-0.27	0.16	3.50E+05	0.00333	9.4
11	0.95	44.2	4.9	0.21	0.16	3.59E+05	0.00292	10.5
12	0.98	44.1	4.1	-0.28	0.16	3.69E+05	0.00271	11.2
13	1.00	44.2	4.4	0.06	0.16	3.78E+05	0.00268	11.1
14	1.07	44.1	16.7	-0.09	0.64	4.02E+05	0.00258	5.1
15	1.17	44.2	16.8	0.37	0.64	4.41E+05	0.00253	5.2
16	1.27	44.1	15.7	0.16	0.64	4.79E+05	0.00238	5.4
17	1.37	44.1	15.6	0.04	0.64	5.17E+05	0.00239	5.4
18	1.47	44.1	15.3	0.27	0.64	5.55E+05	0.00231	5.5
19	1.57	44.0	15.0	-0.10	0.64	5.94E+05	0.00232	5.4
20	1.68	44.0	14.7	0.06	0.64	6.32E+05	0.00225	5.5
21	1.78	44.1	15.0	0.36	0.64	6.70E+05	0.00225	5.6
22	1.88	44.1	15.6	0.45	0.64	7.09E+05	0.00233	5.6
23	1.98	44.1	15.0	0.80	0.64	7.47E+05	0.00217	6.2
24	2.08	44.1	21.8	1.18	0.64	7.85E+05	0.00321	0.0 *

Table 8. Stanton number data for the crest-aligned case for U_∞ = 12 m/s.

RUN : 101290-1
U = 12.2 m/s
Rho = 1.17 kg/m^3
Tr = 25.7 C

Pbar = 75.7 cm Hg
Cp = 1.01 kJ/kg C
T = 25.6 C

Twb = 16.1 C
Mu = 1.86E-05 kg/m s
To = 25.7 C

PL	x(m)	Tw(C)	W(W)	Qc(W)	Qr(W)	Rex	St	U (%)
1	0.05	44.1	48.5	0.00	0.00	0.00E+00	0.00000	0.0 *
2	0.15	43.9	75.2	0.79	0.62	1.17E+05	0.00602	1.9
3	0.25	43.9	56.2	0.37	0.62	1.95E+05	0.00451	2.0
4	0.36	43.9	52.9	0.42	0.62	2.73E+05	0.00422	2.1
5	0.46	43.9	47.3	0.12	0.62	3.51E+05	0.00379	2.1
6	0.56	43.9	44.3	-0.18	0.62	4.29E+05	0.00358	2.2
7	0.66	44.0	42.1	0.11	0.62	5.07E+05	0.00336	2.3
8	0.76	43.9	40.6	-0.08	0.62	5.85E+05	0.00327	2.3
9	0.86	43.9	39.3	-0.26	0.62	6.63E+05	0.00318	2.3
10	0.93	43.9	7.5	-0.02	0.15	7.12E+05	0.00240	7.0
11	0.95	43.9	6.8	0.10	0.16	7.32E+05	0.00212	7.7
12	0.98	43.9	6.0	-0.20	0.15	7.51E+05	0.00197	8.2
13	1.00	43.9	6.3	0.09	0.15	7.71E+05	0.00198	8.1
14	1.07	43.9	24.9	0.06	0.62	8.19E+05	0.00197	4.3
15	1.17	43.9	25.5	0.21	0.62	8.97E+05	0.00201	4.3
16	1.27	44.0	24.4	0.44	0.62	9.75E+05	0.00189	4.4
17	1.37	44.0	24.3	0.10	0.62	1.05E+06	0.00192	4.3
18	1.47	44.0	23.9	0.21	0.62	1.13E+06	0.00187	4.4
19	1.57	44.0	24.2	-0.01	0.62	1.21E+06	0.00191	4.3
20	1.68	44.0	23.6	0.12	0.62	1.29E+06	0.00185	4.4
21	1.78	44.0	24.1	0.36	0.62	1.37E+06	0.00188	4.4
22	1.88	44.0	24.7	0.48	0.62	1.44E+06	0.00192	4.4
23	1.98	43.9	23.3	0.49	0.62	1.52E+06	0.00182	4.6
24	2.08	43.9	31.0	0.00	0.00	0.00E+00	0.00000	0.0 *

Table 9. Stanton number data for the crest-aligned case for U_∞ = 27 m/s.

```
RUN :  101790-1
U   =  27.8 m/s        Pbar = 75.9 cm Hg       Twb = 18.9 C
Rho =  1.17 kg/m^3     Cp   = 1.01 kJ/kg C     Mu  = 1.86E-05 kg/m s
Tr  =  26.4 C          T    = 26.1 C           To  = 26.5 C
```

PL	x(m)	Tw(C)	W(W)	Qc(W)	Qr(W)	Rex	St	U (%)
1	0.05	44.1	164.1	1.58	0.60	8.86E+04	0.00600	0.0 *
2	0.15	44.0	122.5	0.86	0.60	2.66E+05	0.00451	1.7
3	0.25	44.0	101.8	0.42	0.60	4.43E+05	0.00376	1.7
4	0.36	44.0	96.3	0.25	0.60	6.20E+05	0.00355	1.7
5	0.46	44.0	90.3	0.15	0.60	7.98E+05	0.00333	1.8
6	0.56	44.0	86.4	-0.16	0.60	9.75E+05	0.00320	1.8
7	0.66	44.0	82.8	0.02	0.60	1.15E+06	0.00306	1.8
8	0.76	44.0	80.1	-0.38	0.60	1.33E+06	0.00299	1.8
9	0.86	44.0	79.9	-0.04	0.60	1.51E+06	0.00295	1.8
10	0.93	44.0	13.3	-0.14	0.15	1.62E+06	0.00198	4.0
11	0.95	44.1	11.8	0.08	0.15	1.66E+06	0.00172	4.4
12	0.98	44.1	10.9	-0.07	0.15	1.71E+06	0.00161	4.6
13	1.00	44.1	11.2	0.12	0.15	1.75E+06	0.00163	4.6
14	1.07	43.9	44.9	-0.22	0.59	1.86E+06	0.00167	2.2
15	1.17	44.0	46.4	0.39	0.60	2.04E+06	0.00169	2.2
16	1.27	44.0	45.0	0.33	0.60	2.22E+06	0.00164	2.2
17	1.37	43.9	44.9	-0.08	0.59	2.39E+06	0.00166	2.2
18	1.47	44.0	44.5	0.16	0.60	2.57E+06	0.00163	2.2
19	1.57	43.9	44.8	-0.06	0.60	2.75E+06	0.00165	2.2
20	1.68	43.9	44.3	0.09	0.60	2.92E+06	0.00163	2.2
21	1.78	44.0	44.7	0.24	0.60	3.10E+06	0.00164	2.2
22	1.88	43.9	45.3	0.43	0.60	3.28E+06	0.00166	2.2
23	1.98	43.9	43.9	0.56	0.60	3.46E+06	0.00160	2.3
24	2.08	44.0	53.0	1.39	0.60	3.63E+06	0.00190	0.0 *

Table 10. Stanton number data for the crest-aligned case for U_∞ = 43 m/s.

RUN : 101890-1
U = 42.9 m/s
Rho = 1.17 kg/m^3
Tr = 28.6 C

Pbar = 76.3 cm Hg
Cp = 1.01 kJ/kg C
T = 27.8 C

Twb = 16.7 C
Mu = 1.86E-05 kg/m s
To = 28.7 C

PL	x(m)	Tw(C)	W(W)	Qc(W)	Qr(W)	Rex	St	U (%)
1	0.05	44.2	219.3	1.30	0.54	1.37E+05	0.00596	0.0 *
2	0.15	44.4	151.6	1.28	0.54	4.10E+05	0.00407	1.8
3	0.25	44.4	129.0	0.62	0.54	6.84E+05	0.00347	1.8
4	0.36	44.3	120.8	0.14	0.54	9.58E+05	0.00328	1.8
5	0.46	44.3	115.8	0.03	0.54	1.23E+06	0.00314	1.8
6	0.56	44.4	113.3	0.15	0.54	1.50E+06	0.00305	1.8
7	0.66	44.4	108.4	-0.14	0.54	1.78E+06	0.00293	1.9
8	0.76	44.4	106.4	-0.03	0.54	2.05E+06	0.00287	1.9
9	0.86	44.4	104.5	-0.13	0.54	2.33E+06	0.00283	1.9
10	0.93	44.3	16.9	-0.13	0.14	2.50E+06	0.00183	3.5
11	0.95	44.4	14.9	0.10	0.14	2.57E+06	0.00159	3.8
12	0.98	44.4	13.8	-0.07	0.14	2.63E+06	0.00149	3.9
13	1.00	44.4	14.3	0.13	0.14	2.70E+06	0.00152	3.9
14	1.07	44.3	57.8	-0.18	0.54	2.87E+06	0.00157	2.1
15	1.17	44.4	60.6	0.68	0.55	3.15E+06	0.00160	2.1
16	1.27	44.4	58.2	0.33	0.54	3.42E+06	0.00155	2.1
17	1.37	44.3	58.2	-0.05	0.54	3.69E+06	0.00157	2.1
18	1.47	44.4	58.1	0.34	0.54	3.97E+06	0.00155	2.1
19	1.57	44.4	58.3	0.12	0.54	4.24E+06	0.00156	2.1
20	1.68	44.3	56.9	-0.05	0.54	4.51E+06	0.00153	2.1
21	1.78	44.4	58.5	0.47	0.54	4.79E+06	0.00156	2.1
22	1.88	44.4	58.7	0.36	0.54	5.06E+06	0.00157	2.1
23	1.98	44.4	57.9	0.93	0.54	5.34E+06	0.00153	2.1
24	2.08	44.4	65.6	1.17	0.54	5.61E+06	0.00174	0.0 *

Table 11. Stanton number data for the crest-aligned case for U_∞ = 58 m/s.

```
RUN :  101690-1
U   =  58.0 m/s            Pbar = 76.0 cm Hg        Tub = 18.9 C
Rho =  1.16 kg/m^3         Cp   = 1.01 kJ/kg C      Mu  = 1.86E-05 kg/m s
Tr  =  31.1 C              T    = 29.7 C            To  = 31.3 C
```

PL	x(m)	Tw(C)	W(W)	Qc(W)	Qr(W)	Rex	St	U (%)
1	0.05	44.4	230.0	2.26	0.47	1.83E+05	0.00548	0.0 *
2	0.15	44.5	162.9	1.76	0.47	5.50E+05	0.00386	2.3
3	0.25	44.4	139.2	1.01	0.47	9.16E+05	0.00332	2.3
4	0.36	44.5	134.0	0.93	0.47	1.28E+06	0.00318	2.3
5	0.46	44.4	126.2	0.48	0.47	1.65E+06	0.00302	2.3
6	0.56	44.4	123.2	0.31	0.46	2.01E+06	0.00296	2.4
7	0.66	44.4	118.8	0.24	0.46	2.38E+06	0.00286	2.4
8	0.76	44.4	116.0	0.14	0.46	2.75E+06	0.00279	2.4
9	0.86	44.4	115.1	0.40	0.47	3.11E+06	0.00275	2.3
10	0.93	44.3	18.0	-0.18	0.12	3.34E+06	0.00175	3.8
11	0.95	44.4	16.0	0.19	0.12	3.43E+06	0.00151	3.9
12	0.98	44.4	14.9	-0.07	0.12	3.53E+06	0.00144	4.1
13	1.00	44.4	15.5	0.23	0.12	3.62E+06	0.00147	3.9
14	1.07	44.3	63.0	0.15	0.46	3.85E+06	0.00152	2.6
15	1.17	44.4	65.5	0.69	0.46	4.21E+06	0.00156	2.5
16	1.27	44.4	63.7	0.63	0.46	4.58E+06	0.00151	2.5
17	1.37	44.4	64.2	0.61	0.46	4.95E+06	0.00152	2.5
18	1.47	44.4	62.3	0.38	0.46	5.31E+06	0.00149	2.5
19	1.57	44.4	63.6	0.40	0.46	5.68E+06	0.00151	2.5
20	1.68	44.4	62.4	0.30	0.46	6.04E+06	0.00149	2.5
21	1.78	44.4	63.1	0.54	0.46	6.41E+06	0.00150	2.5
22	1.88	44.4	64.2	0.78	0.46	6.78E+06	0.00152	2.5
23	1.98	44.3	61.7	0.72	0.46	7.14E+06	0.00147	2.5
24	2.08	44.4	70.6	1.62	0.47	7.51E+06	0.00165	0.0 *

Table 12. Stanton number data for the crest-aligned case for U_∞ = 66 m/s.

RUN : 102290-1
U = 66.2 m/s Pbar = 75.8 cm Hg Twb = 20.0 C
Rho = 1.15 kg/m^3 Cp = 1.01 kJ/kg C Mu = 1.86E-05 kg/m s
Tr = 32.7 C T = 30.8 C To = 33.0 C

PL	x(m)	Tw(C)	W(W)	Qc(W)	Qr(W)	Rex	St	U (%)
1	0.05	44.1	214.9	1.65	0.40	2.08E+05	0.00532	0.0 *
2	0.15	44.1	154.4	0.93	0.40	6.23E+05	0.00383	3.0
3	0.25	44.2	133.6	0.65	0.41	1.04E+06	0.00328	3.0
4	0.36	44.2	125.5	0.31	0.41	1.45E+06	0.00309	3.1
5	0.46	44.1	120.2	-0.07	0.40	1.87E+06	0.00299	3.2
6	0.56	44.1	117.5	-0.06	0.40	2.28E+06	0.00292	3.1
7	0.66	44.1	113.1	-0.11	0.40	2.70E+06	0.00282	3.2
8	0.76	44.1	111.1	-0.11	0.40	3.11E+06	0.00276	3.2
9	0.86	44.2	109.8	0.08	0.40	3.53E+06	0.00272	3.1
10	0.93	44.1	17.3	-0.18	0.10	3.79E+06	0.00174	4.4
11	0.95	44.2	15.2	0.12	0.10	3.89E+06	0.00149	4.5
12	0.98	44.1	14.2	-0.13	0.10	4.00E+06	0.00142	4.8
13	1.00	44.2	14.9	0.19	0.10	4.10E+06	0.00145	4.5
14	1.07	44.1	60.7	0.09	0.40	4.36E+06	0.00150	3.3
15	1.17	44.2	62.8	0.68	0.41	4.78E+06	0.00153	3.1
16	1.27	44.2	61.2	0.58	0.41	5.19E+06	0.00149	3.1
17	1.37	44.1	60.8	0.24	0.40	5.61E+06	0.00150	3.2
18	1.47	44.2	59.9	0.40	0.40	6.02E+06	0.00147	3.2
19	1.57	44.1	60.1	0.13	0.40	6.44E+06	0.00149	3.2
20	1.68	44.1	59.2	0.18	0.40	6.85E+06	0.00147	3.2
21	1.78	44.1	59.8	0.32	0.40	7.27E+06	0.00147	3.2
22	1.88	44.1	61.0	0.41	0.40	7.68E+06	0.00150	3.2
23	1.98	44.1	59.2	0.58	0.40	8.10E+06	0.00145	3.2
24	2.08	44.2	66.0	1.10	0.40	8.51E+06	0.00160	0.0 *

Skin Friction Coefficient Data (Base-Aligned Case)

Table 13. Skin friction coefficient data for the base-aligned case for $U_\infty = 12$ m/s. The C_f value at x = 0.86 m was obtained using the hot-wire technique (Hosni, 1989), all other values were measured using the Preston tube technique.

x (m)	C_f
0.86	0.00616
0.97	0.00257
1.07	0.00292
1.17	0.00290
1.27	0.00293
1.37	0.00300
1.58	0.00302
1.78	0.00303
1.98	0.00301

Table 14. Skin friction coefficient data for the base-aligned case for $U_\infty = 58$ m/s. The C_f value at $x = 0.86$ m was obtained using the hot-wire technique (Hosni, 1989), all other values were measured using the Preston tube technique.

x (m)	C_f
0.86	0.00577
0.97	0.00188
1.07	0.00210
1.17	0.00222
1.27	0.00230
1.37	0.00234
1.58	0.00237
1.78	0.00239
1.98	0.00237

Skin Friction Coefficient Data (Crest-Aligned Case)

Table 15. Skin friction coefficient data for the crest-aligned case for $U_\infty = 12$ m/s. The C_f value at x = 0.86 m was obtained using the hot-wire technique (Hosni, 1989), all other values were measured using the Preston tube technique.

x (m)	C_f
0.86	0.00616
0.97	0.00250
1.07	0.00279
1.17	0.00289
1.27	0.00295
1.37	0.00296
1.58	0.00299
1.78	0.00303
1.98	0.00303

Table 16. Skin friction coefficient data for the crest-aligned case for $U_\infty = 58$ m/s. The C_f value at $x = 0.86$ m was obtained using the hot-wire technique (Hosni, 1989), all other values were measured using the Preston tube technique.

x (m)	C_f
0.86	0.00577
0.97	0.00191
1.07	0.00216
1.17	0.00224
1.27	0.00231
1.37	0.00234
1.58	0.00237
1.78	0.00239
1.98	0.00240